Vanfossen, Jr., Joseph A. Ph.D., NUCLEAR PHYSICS

CHARM MESON PRODUCTION IN AU-AU COLLISIONS AT
$\sqrt{s_{NN}} = 200$ GEV AT RHIC (118 pp.)

Director of Dissertation: Spyridon Margetis

This research work is in the field of experimental nuclear physics, more specifically, the analysis of data taken with the Solenoidal Tracker at RHIC (STAR) apparatus at the Relativistic Heavy Ion Collider (RHIC) located at Brookhaven National Laboratory (BNL). There, we accelerate and collide beams of heavy ions (e.g. gold nuclei) at relativistic velocities. The collisions of heavy nuclei in the STAR Experiment compress nuclear matter to high densities, and heat it to extreme temperatures, over one trillion degrees Celsius. Under such conditions, Lattice QCD and other phenomenological models predict a phase transition in nuclear matter, a transition, where quarks and gluons become deconfined, i.e. they freely move throughout the interaction volume and are no longer confined to individual nucleons, forming Quark Gluon Plasma (QGP), a new state of nuclear matter. The study of QGP, its properties and dynamics, will provide a better understanding of QCD, the strong force, and of the history of the early universe.

Mesons containing heavy flavor (charm and bottom) quarks can be used in QGP searches. Heavy quarks are produced mainly in the early stages of a collisions via energetic parton-parton interactions; heavy flavor production in QGP or during hadronization is suppressed due to the high masses of the quarks. Heavy quarks can therefore be used to probe the whole evolution of the system and as a calibrated tool to better

understand the nature of the early, hot matter formed in the collisions.

A key finding by the experiments at RHIC is the anomalously low production of heavy flavor at high transverse momentum values. This was found by measuring the yields of the decay electrons from mesons containing either charm or bottom quarks. These measurements suffer from very large combinatorial backgrounds and conceal the parent's kinematic properties. A suppression of particle production at high transverse momenta is likely caused by their interaction with the hot and dense surrounding medium, as the quarks traverse it. Such suppression is an indicator that the medium generated in relativistic heavy-ion collisions is strongly interacting. Theoretical models were successful in describing the suppression of light quarks but under-predicted the observed heavy-flavor suppression. The data triggered a new effort in modeling where theorists started taking into account the energy loss due to elastic collisions between the traversing parton and the surrounding medium. To fully understand the interplay between elastic and inelastic collision mechanisms of light and heavy partons and the hot medium, we needed precise data on heavy flavor production. Also, in order to be able to access the parent's kinematic information, one needs to perform a full topological reconstruction of the parent's decay. This will also allow for the separation of charm and bottom mesons. The study of D^0 mesons, the lightest mesons with a charm quark, can be used to study the properties of the medium created in collisions, such as the density, flow, and thermalization of the medium.

This dissertation presents an attempt to measure $D^0/\bar{D}^0$ ratios and D^0 meson production in Au+ Au collisions at $\sqrt{s_{NN}} = 200\,\mathrm{GeV}$ from fully reconstructed decays. For this purpose, we used a silicon tracker in STAR consisting of the Silicon Vertex

Tracker (SVT) and the Silicon Strip Detector (SSD), along with the Time Projection Chamber (TPC) in a special run in the year 2007. We have developed new calibration and microvertexing techniques in the data analysis. We performed full secondary vertex reconstruction, to topologically reconstruct the secondary vertex of the D^0 meson in the decay channel $D^0 \rightarrow K^- + \pi^+$ ($B.R. = 3.89\%$ and $c\tau = 123\mu m$) and then performed a standard invariant mass analysis. At the same time we used a new tool (TMVA) in high energy physics for optimizing the signal to background ratio.

However, precise measurements of open heavy flavor are difficult to obtain with the SVT due to a) the low yields and short lifespan of heavy hadrons, b) the huge combinatorial background, c) the poor statistics in the final data sample and d) the poor resolution of the SVT. STAR proposed and built a new generation vertex tracker, the Heavy Flavor Tracker (HFT). The HFT made its debut during the 2014 year's run and has vastly improved the experiment's heavy flavor capabilities making STAR an ideal detector to study the hot and dense matter created in heavy ion collisions. Taking advantage of the greatly improved pointing resolution from a dedicated microvertex detector, it is possible to directly track and reconstruct weak decay products from hadrons comprised of heavy 'charm' and 'bottom' quarks with low background. The HFT consists of three sub-detectors: PIXEL (PXL), the Intermediate Silicon Tracker (IST), and the Silicon Strip Detector (SSD) with 4 separate layers of silicon to guide tracks reconstructed in the Time Projection Chamber down to a pointing resolution of around $30\,\mu$m for $1\,$GeV/c pions, a requirement to distinguish between an event's primary vertex and the position of a hadron's decay.

In this Dissertation we present the details of our SVT work, data analysis and results, and briefly show and discuss the recent results obtained with the HFT.

CHARM MESON PRODUCTION IN AU-AU COLLISIONS AT $\sqrt{s_{NN}} = 200$ GEV AT RHIC

A dissertation submitted to
Kent State University in partial
fulfillment of the requirements for the
degree of Doctor of Philosophy

by

Joseph A. Vanfossen, Jr.

May, 2017

Dissertation written by

Joseph A. Vanfossen, Jr.

B.S., Baldwin-Wallace College, 2004

M.A., Kent State University, 2012

Ph.D., Kent State University, 2017

Approved by

______________________________ , Chair, Doctoral Dissertation Committee
Dr. Spyridon Margetis

______________________________ , Members, Doctoral Dissertation Committee
Dr. Declan Keane

______________________________ ,
Dr. Maxim Dzero

______________________________ ,
Dr. Edgar Kooijman

______________________________ ,
Dr. Robin Selinger

Accepted by

______________________________ , Chair, Department of Physics
Dr. James T. Gleeson

______________________________ , Dean, College of Arts and Sciences
Dr. James L. Blank

Table of Contents

List of Figures

List of Tables

Acknowledgments

For Peyton and Ryder, may you always have the drive and perseverance to reach your goals. There is nothing you cannot achieve!

I would like to express my sincere gratitude to Spiros Margetis for the continuous support of my Ph.D work. Thank you for your patience, motivation, and immense knowledge. Your guidance was monumental though the course of our research and the writing of this dissertation.

I would like to thank members of my dissertation defense committee: Spiros Margetis, Declan Keane, Maxim Dzero (who better to serve on a committee for D^0 research), Edgar Kooijman, and Robin Selinger for their insightful comments and encouragement, but also for the insightful questions which allowed me to think about my research from various perspectives.

My sincere thanks also goes to Spiros and Declan, who provided me an opportunity to join their experimental nuclear group as a research assistant. Thank you to all of the members of the STAR Collaboration at Brookhaven National Laboratory, all who played a role in allowing me to access to the laboratory and research facilities. We worked though many days and nights taking shifts together and ensuring that the STAR detectors were functioning well. Without they precious support it would not be possible to conduct this research.

I thank my Jonathan Bouchet and Jaiby Joseph Ajish for many hours of stimulating discussions, for the sleepless nights we were working together before deadlines, and for all the fun we have had over the years.

Last but not the least, I would like to thank my family: my wife Julie, our children Peyton and Ryder, my parents, my sister, my in-laws, and the rest of our family. Without your unwavering support, I may have never been able to achieve my goals and complete my Ph.D.

Chapter 1

Introduction

It is widely accepted in Cosmology today that the Universe began about 13.8 billion years ago in an event known as the Big Bang. The conditions of the early Universe were extremely hot and dense. Under such conditions, nuclear matter might undergo a phase transition to a new phase called Quark Gluon Plasma (QGP). In order to understand the behavior of matter shortly after the Big Bang, it is required to create and study in the laboratory nuclear matter at high density and temperature. At the Relativistic Heavy Ion Collider (RHIC), located at Brookhaven National Laboratory (BNL), heavy ions (atomic nuclei) are accelerated and collide with each other at nearly the speed of light. The interactions of the constituent particles, quarks and gluons, are governed by Quantum Chromodynamics (QCD). The medium created is then probed in order to understand its nature, i.e. whether the QGP phase of matter has been created or not. In this dissertation we analyze the data obtained in the STAR experiment at RHIC looking for some specific aspects of the collision that will help us understand the nature of the matter created in these collisions.

1.1 The Standard Model and Color Interactions

The Standard Model of Particle Physics, developed in the 1970's, describes the interactions of fundamental particles. The theory was developed to produce a single theory that describes all four fundamental forces of nature, electromagnetic, weak nuclear, strong nuclear, and gravitation, as a manifestation of a single fundamental force. As of the writing of this dissertation, the Standard Model is currently successful in describing the unification of all fundamental forces with the exception of the gravitational force. In the Standard Model, all fundamental particles may be placed into two categories, half-integer spin fermions and integer spin bosons. The force carriers in the Standard Model are bosons, responsible for the interactions between particles, and the fermions are the fundamental building blocks of matter.

The fermions of the Standard Model can be separated further into two more categories, quarks and leptons, and each comes in three generations. There are six quarks, up, down, strange, charm, bottom and top, and six leptons, electron, electron neutrino, muon, muon neutrino, tau and tau neutrino. Leptons carry integer electric charge and quarks carry fractional electric charges. Every fermion also has a corresponding antiparticle with the opposite electric charge. The gauge bosons of the Standard Model are the photon (γ), force carrier for the electromagnetic force, the W and Z bosons, force carriers for the weak nuclear force, and the gluons (g), force carriers for the strong nuclear force. Table 1.1 shows the fundamental particles of the Standard Model and some of their properties, including their electric charge, mass, spin and how they are split into generations.

Part of the Standard Model is the Quark Model that defines how quarks are combined to form composite particles that we call hadrons. According to this model, a hadron is a composite of either two quarks (mesons) or three quarks (baryons), some of which may have identical quantum numbers when the strong nuclear force is neglected. In order to describe how quarks could coexist in a hadron with identical quantum states without being in violation of the Pauli Exclusion Principle, the

Generation	Quark	Electric Charge($\|q_e\|$)	Mass(MeV/c^2)	Spin
First	Up (u)	+2/3	1.7-3.1	1/2
	Down (d)	-1/3	4.1-5.7	1/2
Second	Charm (c)	+2/3	1180-1340	1/2
	Strange (s)	-1/3	80-130	1/2
Third	Top (t)	+2/3	172900±1500	1/2
	Bottom (b)	-1/3	4130-4370	1/2
Generation	**Lepton**	**Electric Charge($\|q_e\|$)**	**Mass(MeV/c^2)**	**Spin**
First	Electron (e)	-1	0.511	1/2
	Electron Neutrino (ν_e)	0	0	1/2
Second	Muon (μ)	-1	105.66	1/2
	Muon Neutrino (ν_μ)	0	0	1/2
Third	Tau (τ)	-1	1776.84	1/2
	Tau Neutrino (ν_τ)	0	0	1/2
Force	**Gauge Boson**	**Electric Charge($\|q_e\|$)**	**Mass(GeV/c^2)**	**Spin**
Electromagnetic	γ (Photon)	0	0	1
Weak Nuclear	$W^{\pm}$	±1	80.3980±0.025	1
	Z^0	0	91.1876±0.0021	1
Strong Nuclear	g (8 Gluons)	0	0	1

Table 1.1: Quarks, Leptons and Gauge Bosons of the Standard Model

concept of color charge was introduced. The color charge, analogous to the electric charge, is responsible for the color interaction. Color charge, unlike the electric charge, comes in six varieties, red, green, blue for quarks and antired, antigreen and antiblue for antiquarks. Also unlike the electric charge where the photon carries no electric charge, the eight gluons carry color charge as well. Each gluon represents a mixed state of color and anticolor. So, in addition to being the mediator of the color interaction, the gluons themselves also interact via the color charge. In the Quark Model all hadrons, including the everyday nucleons, must be either ‘white’ or colorless. One can always create such objects with two or three quark combinations. There is recent evidence that other combinations of quarks might exist (four or five quark particles) but this is research beyond the current Quark Model.

1.1.1 Strong Force and Quark Confinement

The strong nuclear force has the weird and counter-intuitive feature that it grows weaker, asymptotically approaching zero, as either the separation between particles decreases or the interaction energy increases. This is called asymptotic freedom. As either the distance between quarks grows, or the interaction energy decreases, the interaction between particles grows stronger eventually making it energetically more favorable to create a quark-antiquark pair rather than to separate the quarks completely. The inability to separate quarks is called confinement, and is the reason that free quarks are not observed. Figure 1.1 shows the strong coupling as it varies with momentum transfer[1]. In the realm where $\alpha_s^2 << 1$, also high Q or high temperature, high density, perturbation theory may be used for calculations. As α_s increases, perturbative techniques may no longer be used making low temperature, low density calculations very complicated.

Asymptotic Freedom, as a feature of QCD, arises from the self-interaction of gluons and the specific number of gluons (8). Because the gluons carry a color charge, there is an antiscreening effect of the color charge. In Quantum Electrodynamics (QED), a particle's charge is screened by electron/positron pairs surrounding the particle in the vacuum, allowing one to see less of the charge as you move away from the particle. In QCD, the opposite effect occurs. In the case of a single particle with color charge surrounded by gluons, as one moves away from the particle, the color charges of the gluons contribute to the overall color charge observed allowing the strong force to increase with distance rather than decrease.

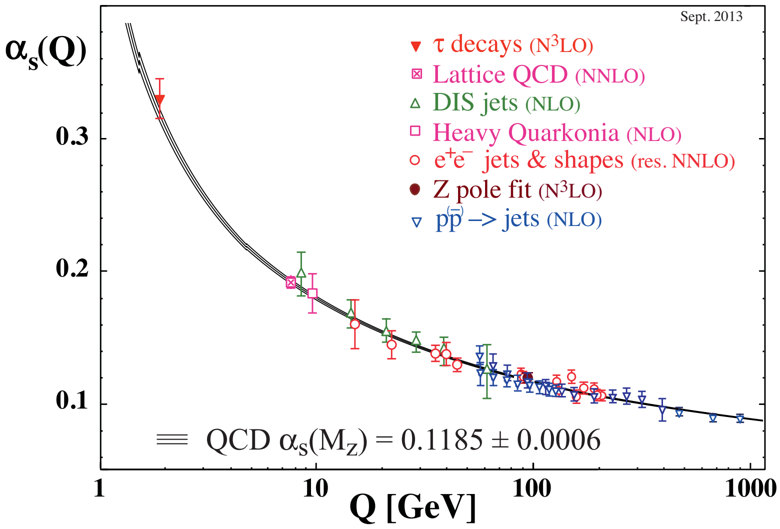

Figure 1.1: QCD Coupling Constant vs. Energy Transfer

1.1.2 Deconfinement, Chiral Symmetry and Quark-Gluon Plasma

As discussed above, quarks are always observed in color singlet states, consisting of color/anticolor pairs called mesons, or a mixture of all three (red, blue and green) color charges called baryons. When nuclear matter is compressed to very high density and temperatures, lattice QCD calculations as well as phenomenological models predict that it undergoes a phase transition to QGP[2][3][4]. Conditions sufficient for the formation of QGP have not existed naturally since shortly after the Big Bang. QGP is formed when energy densities are in excess of 1 GeV/fm^3 and this can be achieved either by temperatures of about 1-2 Trillion degrees of the Kelvin scale (‘heat’), or nuclear densities of about ten times the ground state nuclear density (‘squeeze’). This can be seen in Fig. 1.2 which shows two sketches of QCD inspired phase diagrams of nuclear matter. Both phase diagrams show that there are two primary phases of nuclear matter, the hadronic phase at low temperature and baryon density (hadron gas), and the parton/QGP phase at high temperature and/or baryon densities. The arrow in the upper left corner of the first phase diagram shows the path taken by the early Universe as it crossed over from QGP to hadron gas and is estimated to have occurred about 10 μs after the start of the Big Bang.

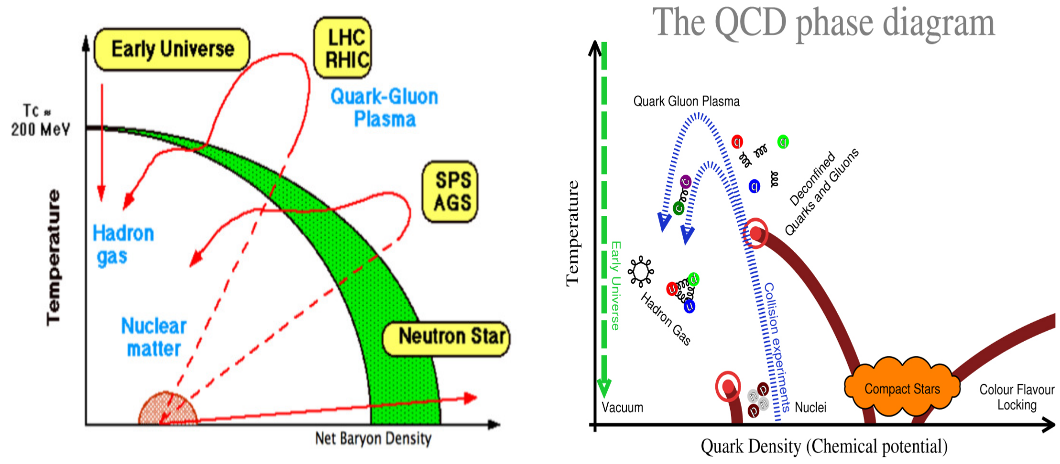

Figure 1.2: QCD Phase Diagram

The arrow in the lower right of the first phase diagram shows the path taken by neutron stars in their formation, where cold nuclear matter gets compressed by gravitational forces. It is still under theoretical research whether the matter at the core of a neutron star is QGP or another state. In high energy nuclear collisions, such as those at RHIC and the Large Hadron Collider (LHC), we both heat and compress nuclear matter. Therefore, the path taken by the nuclear matter in these experiments is between the above two extremes. The QCD phase diagram is an area of intense study, because the transition lines, critical points and all phases of nuclear matter have yet to be mapped out. Two important areas of study related to the QCD phase diagram are the Beam Energy Scan (BES) being conducted at RHIC, where the collision energies between nuclei are reduced in an effort to search for the QCD critical point (Fig. 1.2 [right panel]), and the search for Color Glass Condensates (coherent, high density gluon states), color superconductors and other exotic phases of nuclear mater.

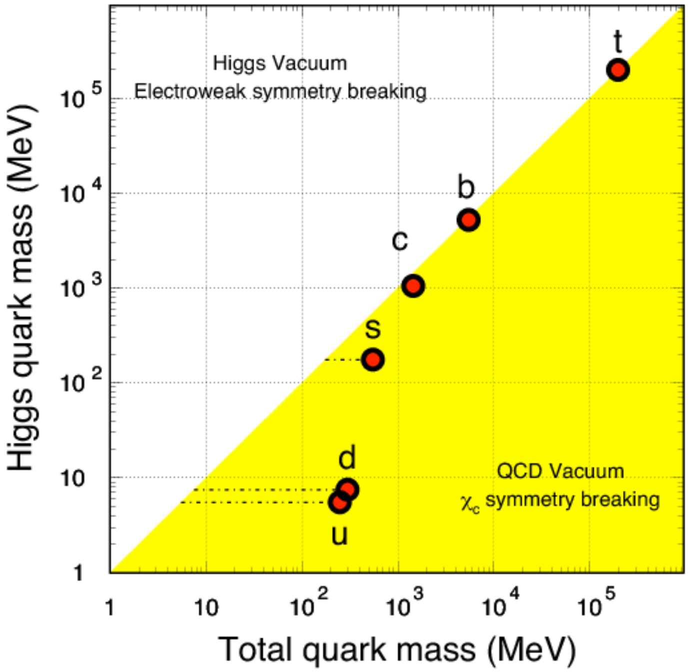

Figure 1.3: The current quark mass lies along the diagonal of the figure, and the greater the effects of the QCD vacuum on the quark's mass, the more it will deviate from the diagonal. Note that the heavy quarks, c, b, t are largely unaffected by the QCD vacuum.

In the QCD Lagrangian the current quark masses are responsible for chiral symmetry breaking. At low temperature (T) and baryon density (ρ), chiral symmetry is broken. When discussing the mass of quarks, one must distinguish between the mechanisms that generate the mass of the quark. When electroweak symmetry is broken, the current mass (Higgs mass) is generated, however when chiral symmetry is spontaneously broken, the QCD mass is generated. The masses of the heavy quarks (c, b, t) are largely dominated by the Higgs mechanism, while the QCD interaction has a significant effect on the masses of the lighter quarks (u, d, s). The figure shows the Higgs quark Mass (current quark mass) vs. the Total Quark Mass (QCD quark mass), where the current quark masses lie along the diagonal, and effects of the QCD vacuum result in a shift below the diagonal. Because the masses of the heavy quarks are unaffected by interactions in the QCD vacuum, they can be used as a calibrated probe for the properties of QGP.

1.2 Nuclear Collisions

In order to study QGP, it must first be created in a laboratory environment. Ultrarelativistic heavy ion collisions offer an environment capable of studying matter at extreme temperature and density. RHIC and the Large Hadron Collider (LHC) offer opportunities to collide heavy nuclei across a few orders of magnitude in energy to study the formation of QGP, and search for the QCD critical point. Careful study and analysis of the kinematics and statistical properties of the particles produced allow one to gain insight into the thermal properties of the medium produced. Because the masses of heavy quarks do not change in and out of the medium, they offer a well calibrated probe to study the properties of the medium produced in nuclear collisions. This section contains a discussion of nuclear collisions, the signatures for QGP and a discussion of heavy flavor physics.

In a Au-Au collision at RHIC energies ($\sqrt{s_{NN}} = 200$ GeV), it is theorized that gluon interactions dominate during the early stages of the collision. Fig. 1.4 shows a Minkowski diagram of the evolution of the medium produced in the collision with the z-axis (horizontal) representing the beam line direction and the t-axis (vertical) is time. A gluon-rich QGP may form in the hot, dense interaction region. The QGP

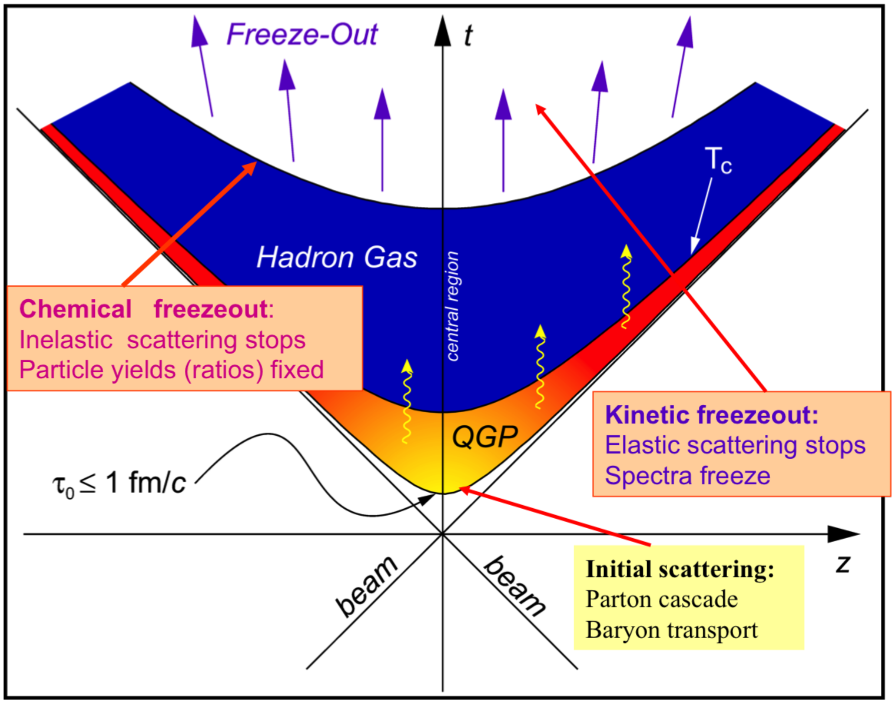

Figure 1.4: Evoluation of Nuclear Collisions

may reach chemical equilibrium of the quark flavors, but is not required to reach chemical equilibrium. After some time, a phase transition back to hadronic matter occurs. As the hadron gas expands and cools, the chemical balance of the particles is effectively fixed because inelastic collisions stop. This is referred to as chemical freezeout, and is thought to occur at temperatures of $\approx 150 - 170\,\text{MeV}$. As the gas continues to expand, the particles separate to the point where they no longer interact even elastically, and the system is said to undergo kinetic (thermal) freezeout. This is expected to occur at temperatures of around 120 MeV. Once kinetic freezeout occurs, the particle spectra are frozen and the particles travel toward the detector systems for data collection.

1.2.1 Signatures of QGP Formation

Experimental results from Alternating Gradient Synchrotron (AGS), Super Proton Synchrotron (SPS), and RHIC have stimulated impressive theoretical advances in the past decade on the thermodynamic and hydrodynamic properties of the hot and strongly interacting matter and the propagation of partons through the medium. However, the complexities of heavy ion collisions and hadron formation bring in ambiguities to such models. The following are some of the robust predictions of the formation of QGP, which survive the quantitative ambiguities.

At low temperature (T) and low baryon density (ρ), QCD exhibits dynamical breaking of chiral symmetry (exhibit actual quark current mass) and confinement. On the other hand, at sufficiently high temperatures and densities (T and ρ much larger than the QCD scale parameter $\Lambda_{\text{QCD}} \sim 200\,\text{MeV}$.) the QCD running coupling constant becomes small (Fig. 1.1). Furthermore, the long-range color electric force is subject to plasma screening and becomes short-ranged. These considerations suggest that the QCD vacuum undergoes a phase change at some values of T (T_C) and ρ (Fig. 1.2). This phase transition restores the broken chiral symmetry, i.e., makes the quarks behave as though they are massless. Various models and numerical simulations of QCD strongly indicate the existence of a transition from the hadronic phase to the quark-gluon phase. The new color degrees of freedom are then manifested as a rapid increase in entropy density, hence in pressure, and by a consequent change in the equation of state (EOS). The transition can be understood in terms of the number of degrees of freedom. Above the transition temperature, the gluon and quark degrees of freedom are activated. For gluons, 8(color) × 2(spin) gives a total of 16 degrees of freedom and for quarks, 2-3 (light flavors) × 2 (quark-antiquark) × 3 × 3 (colors) × 2 (spin) gives a total of 24-36 degrees of freedom. Thus, in the Quark-Gluon Plasma there are about 40-50 internal degrees of freedom in the temperature range (1-3)T$_C$. As the number of degrees of freedom increases, energy density increases. In the limit, where the deconfined quarks and gluons are non-interacting and the quarks are massless, the Stefan-Boltzmann pressure P_{SB} of this partonic state as a function of temperature T, at zero chemical potential (i.e., zero net quark density), would be simply determined by the number of degrees of freedom: $P_{SB} = T^4[2(N_c^2 - 1) + \frac{7}{2}N_cN_f]\frac{\pi^2}{90}$, (Stefan-Boltzmann law for massless bosons with degeneracy P $\propto$ T4), where N_c is the number of colors and N_f is the number of quark flavors. Here we took $\hbar = c = 1$. The two terms on the right represent the gluon and quark contributions respectively. Refinements to this equation to incorporate effects of color interactions among the constituents, non-vanishing quark masses and chemical potential, in order to predict the transition point from hadronic to partonic degrees of freedom are done with lattice QCD. To get physically relevant predictions, we extrapolate the lattice spacing to the continuum (lattice spacing $\rightarrow 0$), chiral mass to actual current quark mass and thermodynamic (large volume) limits. Within the constraints of computing cost and technical complications lattice QCD calculations have put forth the predictions described below.

Elliptic Flow (v_2)

In collisions of high energy nuclei, a large number of secondary particles is produced. Thus, the occurrence of multi-particle correlations, a collective phenomenon, is expected and is observed. During non-central collisions, the nuclear overlap is approximately an ellipsoid in the early stages of a collision. This causes a pressure gradient that is largest along the shortest axis of the ellipsoid, as shown in Fig. 1.5. This initial spatial anisotropy develops into a momentum space anisotropy. Fig. 1.5 shows a schematic of this process. We use only anisotropic transverse flow from the particle azimuthal distributions at fixed rapidity or pseudorapidity. The azimuthal distributions can be conveniently described by means of Fourier expansion. Anisotropic flow corresponding to the first two harmonics plays a very important role and we use special terms for them, directed and elliptic flow, respectively. The 'elliptic' comes from the fact that the azimuthal distribution of produced particles with non-zero second harmonic represents an ellipse.

Elliptic flow (v_2) is the second Fourier coefficient in the expansion of the azimuthal distribution of the particle with respect to the azimuthal angle ψ_{RP} of the reaction plane: $\frac{dN}{d\phi} \propto 1 + \Sigma_{n=1}^{\infty} 2v_n(p_T, y) \cos n(\phi - \psi_{RP})$.

Because of the symmetry $\phi \leftrightarrow -\phi$ in the collision geometry, no sine terms appear in the above equation. The anisotropic flows v_n generally depend on the particle transverse momentum and rapidity. The coefficients v_n are calculated to be

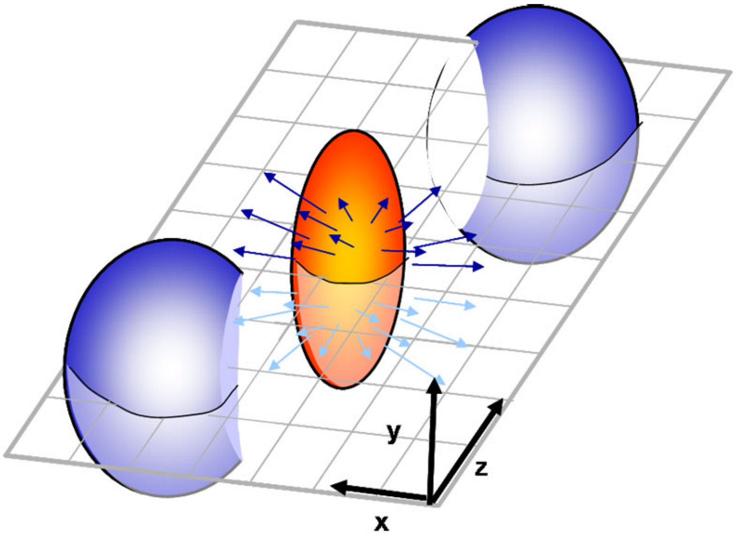

Figure 1.5: Diagram showing the ellipsoidal shape of the medium created in the collision nuclei

$v_n(p_T, y) = \langle \cos n(\phi - \psi_{RP}) \rangle$ where $\langle \ldots \rangle$ denotes an average over the azimuthal distribution of all particles in all events studied. It has been shown that the elliptic flow is sensitive to the early dynamics of produced matter in relativistic heavy ion collisions and it is a robust observable for studying the interactions in the partonic matter.

The transition of ordinary matter into a soup of quarks and gluons happens under extreme conditions. An estimate of the formation time relevant for the hydrodynamic calculations was predicted to be in the vicinity of $\tau_0 = 0.6\,\mathrm{fm/c}$, or approximately $10^{-24}\,\mathrm{s}$. This is shorter than the time taken by a massless particle to traverse the radius of a hadron ($\tau \sim 1\,\mathrm{fm/c}$). The temperature of this transition to QGP is about 150-200 MeV or 100,000 times the temperature of the center of the sun. The energy density is around $\epsilon = 30\,\mathrm{GeV/fm^3}$, and this should be compared with the energy density of a nucleon in its rest frame $\epsilon_N \sim 500\,\mathrm{MeV/fm^3}$, when the system is in local thermal equilibrium. The hydrodynamic models suggest that collisions at RHIC make something that is hotter, denser, smaller and faster than anything observed before. No viscosity was needed to reproduce the RHIC data within experimental and theoretical uncertainties. Thus, the matter created at RHIC is a ‘nearly’ perfect liquid. These extreme conditions permit us only to see the particles that escape from the fireball and reach the detector. These particles can retain the signatures of their past. We can use these signatures to work backwards in time to learn about the phase transition and the new matter created.

Hard Partons (high p_T probes)

Quarks and gluons with very high energies are most likely to be formed during the early stages of a collision. These high transverse momentum partons result from the initial hard scattering (large momentum transfer) of nucleon constituents. After a hard scattering, the parton either undergoes fragmentation to create a high-energy cluster (jet) of particles (in a vacuum), or it interacts with the surrounding medium (if such a medium exists). Parton fragmentation in a vacuum happens in elementary collisions (e^+–e^- or p–p) and has been studied in detail. It can also happen in nucleus–nucleus collisions if the parton is created on the outer surface of the overlapping interaction zone and its momentum vector points away from the bulk medium. In all other cases the parton will interact with the hot, dense medium produced in the collision. A high momentum parton traversing the medium is subjected to energy loss. There are two ways that energy loss occurs. (see also Fig. 1.6 [right panel]) One way to lose energy is via elastic collisions where the initial parton loses (redistributes) its momentum through elastic collisions with other partons in the medium and eventually ‘thermalizes’ and the other way is via inelastic collisions, e.g. induced gluon radiation.

Initially the contribution of the elastic collisions to the total energy loss was thought to be negligible. The energy loss per unit length ($\hat{q}$) is a very important parameter that characterizes the properties of the created medium. For example, in the extreme case of a weakly interacting QGP the energy loss is expected to be relatively low. The energy loss inside cold nuclear matter is expected to be low; something that can be studied in p–A interactions. In the case of strongly interacting matter the energy loss is expected to be relatively high.

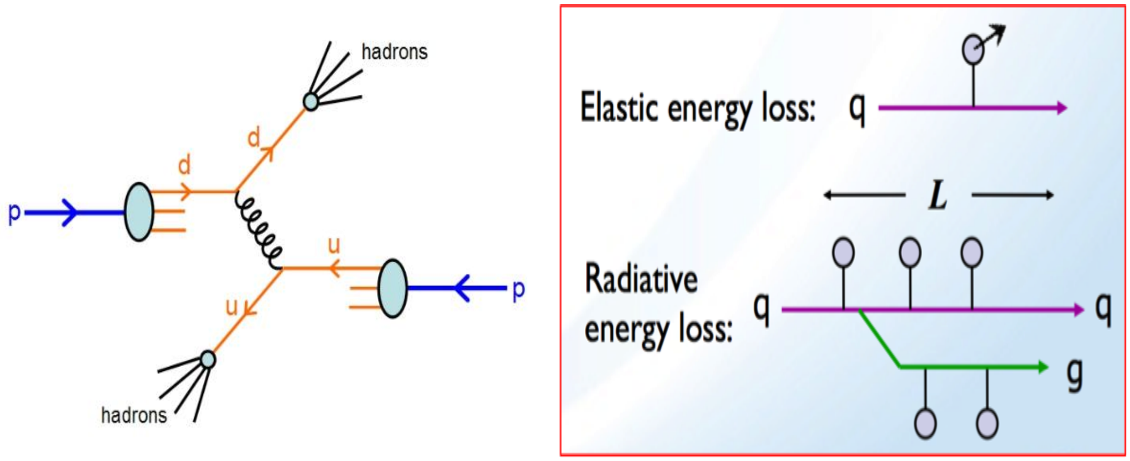

Figure 1.6: Quark-quark and quark-gluon scattering diagrams

High p_T partons are created in energetic quark–quark (see Fig. 1.6 [left panel]) or quark–gluon scattering and they typically emerge back-to-back due to p_T conservation. Hard scattering processes have been established at high transverse momentum (p_T) in elementary collisions at high energy. The high p_T partons fragment into a shower, a 'jet' of particles that is localized in space. Inside the jet the original energetic parton appears as a high p_T hadron. Experimentally we can request ('trigger') an event to be recorded when a high p_T particle appears in a collision, i.e. a particle with p_T above a certain threshold. We can then search in the opposite direction for a high p_T partner. In elementary collisions this correlation is apparent and strong as expected. When heavy nuclei collide at high energies, if the jet is formed near the edge of medium created during the collision, one parton is directed outward, and the other parton must traverse the medium. The study of back to back correlations of these jets can be used to understand the properties of the medium. The 'disappearance' of the back-to-back partner, which goes into the bulk matter generated in the collisions is known as 'jet quenching'. As we mentioned above when such a parton traverses deconfined matter it may lose energy by gluon radiation or elastic scattering, which results in a suppression of the fragmenting high p_T hadrons relative to the yield in baseline p+p measurement. According to models, fast partons are expected to lose more energy per unit length in partonic rather than in hadronic matter through gluon radiation; hence the energy loss might be a signal of whether partonic matter (and perhaps QGP) is created.

The study of back to back jet correlations in Au+Au collisions of varying centrality showed that in the most central Au-Au collisions, away side jets are strongly suppressed (Fig. 1.7)[9], when compared to a linear superposition of p-p collisions. The observed suppression is due to the fact that the medium produced in these collisions is strongly interacting. The initial correlation studies were followed by more detailed, p_T and centrality dependent studies that verified that indeed in central Au+Au collisions at 200 GeV/c the high p_T hadrons are greatly suppressed relative to properly normalized p-p interactions. An example is shown in Fig. 1.8 [left panel][11][16]. The R_{AA} variable in the vertical axis is the ratio of the specific particle yield in Au+Au collisions divided by the properly normalized yield in p-p. The normalization factor is the number of binary (p-p) collisions expected to occur in the specific centrality range

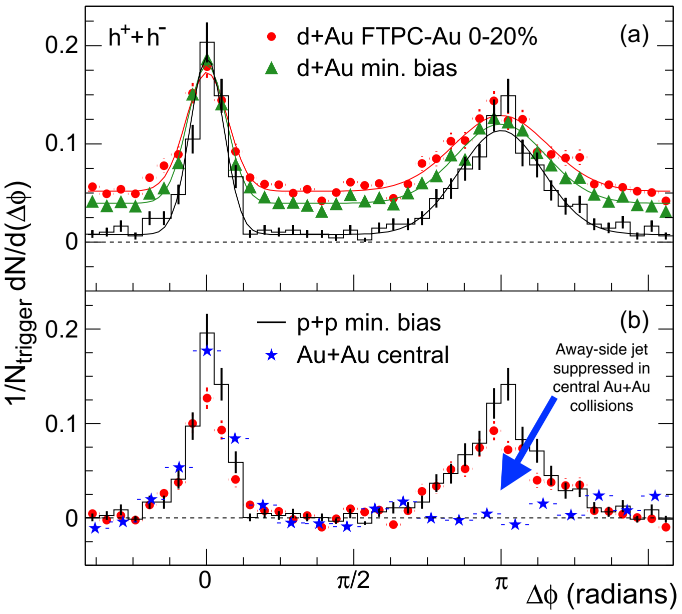

Figure 1.7: The figure above shows near-side and away-side correlations in d+Au, p+p, and central Au+Au collisions. As more QCD medium is created, fewer particles are able to escape the medium on the back side

in Au+Au collisions and it is used to take out trivial 'volume' differences between p-p and Au+Au. In the figure the red and purple points are π^0 and $h^{\pm}$ (mostly π^+ and π^- mesons) from PHENIX and STAR experiments. We see that above a certain value of p_T ($> 4\,\mathrm{GeV/c}$) the ratio is as low as 20%. In the same figure we see that direct photons (purple squares) are compatible with a ratio of ≈ 1 at all p_T values since photons do not interact strongly and therefore pass through the hot medium without any loss.

We also see in the same figure (yellow line) that QCD models or parton energy loss are successful in calculating the magnitude of the effect only when the assumed very high gluon densities per unit of rapidity in the medium, $dN^g/dy \approx 1100$. These initial results from light flavor studies at RHIC demonstrated that a hot partonic medium has been developed during the system evolution in heavy ion collisions and the next task would be to test experimentally whether the medium has reached thermalization.

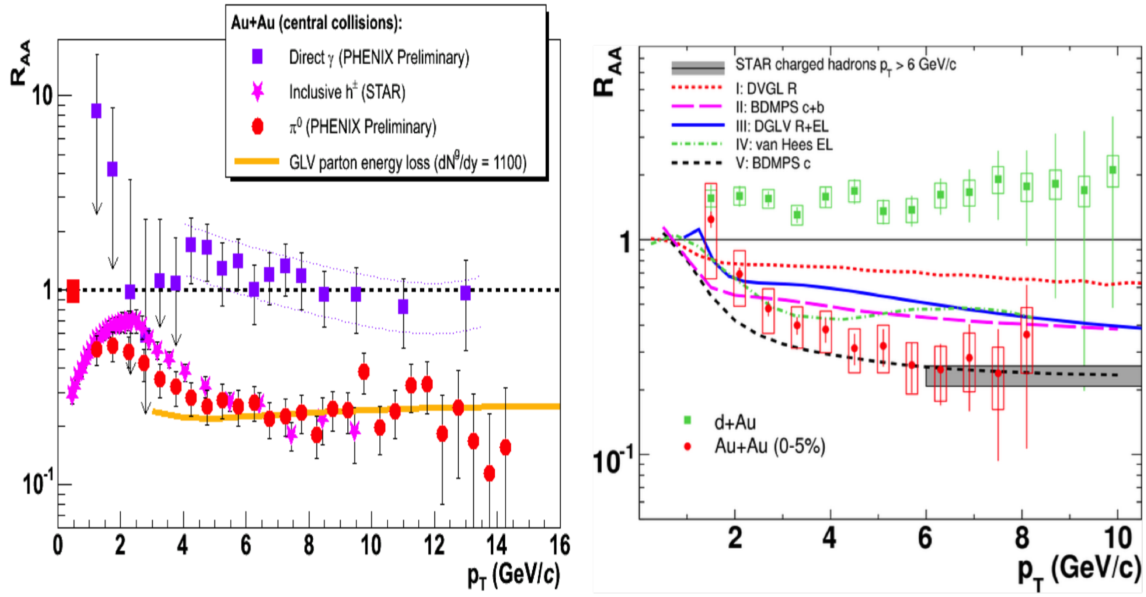

Figure 1.8: Energy loss for hadrons (left panel) and heavy flavor (right panel).

1.2.2 Heavy Flavor

The results from light flavor were followed by similar studies using particles containing heavy flavor quarks (c and b). At that time the experiments were lacking high precision vertex detectors to directly reconstruct the weak decays of heavy flavor particles. Instead they used the semi-leptonic decay channels with an electron in the final state. This method is called ‘non-photonic’ electrons since its major background is electrons from photon conversion in the apparatus. Another disadvantage of this method is that we do not have the complete kinematic information of the original hadron, since we do not fully reconstruct the decay, so we need to use the 'smeared' electron p_T as the kinematic variable.

The initial studies (see red points in Fig. 1.8 [right panel]) showed a suppression of heavy flavor at high p_T values comparable to that for the light hadrons (shown as a grey bar in the figure). This came as a surprise since the QCD model calculations that were successful in predicting the light flavor suppression were predicting a much smaller magnitude of suppression for the heavy quarks. After careful analysis it was realized that elastic collisions with the dense medium make a significant contribution to the total energy loss and they are not negligible. At the same time the experiments were upgrading their apparatuses with high precision vertex trackers so that they could fully reconstruct heavy flavor decays, e.g. $\mathrm{D}^0 \rightarrow K^- + \pi^+$.

Besides the need for a successful description of light and heavy flavor in the same framework (model), there is still the open question of thermalization and for that we can use heavy flavor as a probe. Heavy flavor quarks are generated in the early stages of nuclear collisions through gluon fusion. Heavy quarks (c, b), due to their early creation, can be valuable probes to this end. They are considered as the cleanest probes of QGP. Due to their heavier masses, heavy quarks require more rescatterings to reach a comparable collectivity ('flow') as light quarks (u, d, s). If we observe the kinetic properties of these heavy quarks to be similar to their lighter counterparts, it would be a strong indication of thermalization. If heavy quark collectivity is observed, there must be even more rescatterings happening among light quarks than expected, because the rescattering cross section among light quarks is larger than that between heavy and light quarks. So heavy quark collectivity will indicate the thermalization of the light flavors, although heavy quarks themselves do not have to be thermalized.

The PHENIX and STAR experiment put forward proposals for upgrading their silicon vertex detectors with new, precise pixel technologies in order to be able to perform detailed heavy flavor studies. The STAR collaboration built the Heavy Flavor Tracker (HFT), a four layer silicon vertex tracker using cutting edge silicon pixel technology in the two innermost layers. The application of the microvertexing techniques developed in this dissertation for use with the SVT, has been shown to improve measurements in the HFT era with some results presented in the conclusion of this dissertation.

Chapter 2

The STAR Experiment at RHIC

The Relativistic Heavy Ion Collider (RHIC) is located at Brookhaven National Laboratory on Long Island, New York and is used to search for the phase transition of nuclear matter from the hadronic phase to the quark gluon plasma (QGP). With a circumference of 3.8 km, the RHIC accelerator uses two independent super conducting rings to accelerate atomic nuclei to nearly the speed of light, with the possibility of colliding them at six interaction points around the ring. Initially, there were four active experiments making using RHIC, the now decommissioned smaller experiments, BRAHMS and PHOBOS, as well as two larger currently active experiments STAR and PHENIX. This chapter will discuss the design of RHIC and its experiments. Specific emphasis will be given to the STAR Experiment, particularly highlighting the Time Projection Chamber (TPC), Silicon Strip Detector (SSD) and the Silicon Vertex Tracker (SVT), as these are the primary detector systems used in this analysis.

2.1 RHIC

The RHIC accelerator was designed to study matter at extremely high densities and temperatures, and began physics operation in June 2000 colliding Au+Au beams at a center of mass energy of 130 GeV making it the first facility in the world to collide relativistic heavy ions. RHIC is designed to handle high luminosity beams and a wide range of beam energies and has the unique capability of colliding polarized proton beams. To date RHIC has collided beams of p+p, d+Au, Cu+Cu, Au+Au, and U+U with center of mass energies ranging from 7.7 GeV to 500 GeV. Heavy nuclei can be accelerated up to 200 GeV in RHIC, while p+p beams can be accelerated up to 500 GeV. The RHIC accelerator complex consists of the Tandem Van De Graff facility (TVDG), a linear proton accelerator, the booster synchrotron, and the RHIC ring.

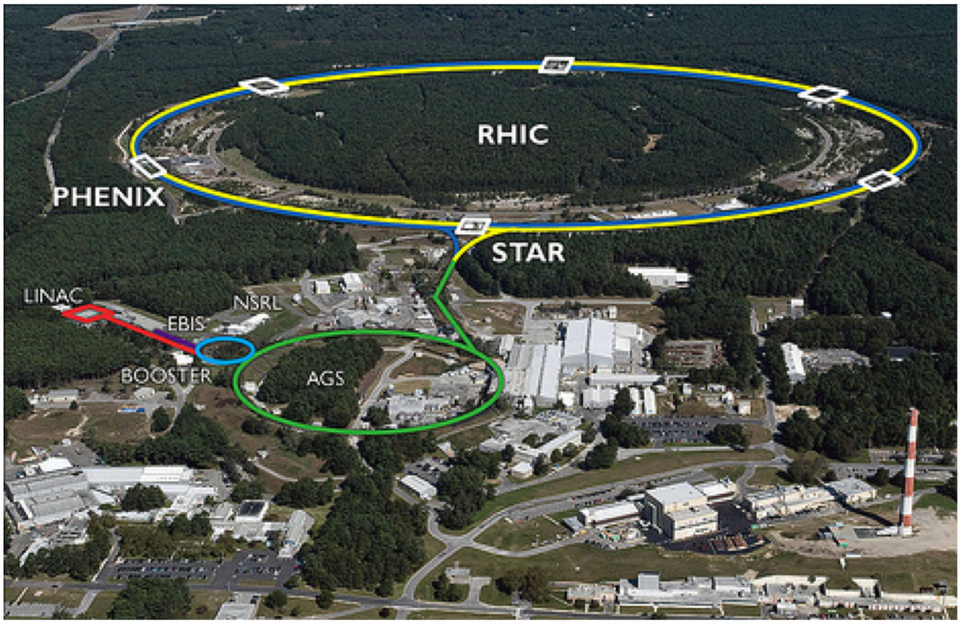

Figure 2.1: The RHIC Complex

The TVDG facility is used to strip the electrons away from the heavy nuclei. To produce a Au ion beam, Au atoms are first produced in the Pulsed Sputter Ion Source, in the TVDG facility, where they are initially ionized with a charge of -1e[25]. These ions are then accelerated through the TVDG facility to an energy of about 1 MeV per nucleon. Next, the ions are passed through a thin gold foil, ionizing them to a net charge of +32e. The ions are then accelerated in the booster synchrotron to an energy of 95 MeV per nucleon[47]. Upon exit from the booster synchrotron, they are further stripped to a net charge of +77e and transferred to the Alternating Gradient Synchrotron Booster (AGS).

In the case of a proton beam, protons are supplied by the 200 MeV linear accelerator (Linac). Upon exit from the Linac, the proton beam is injected into the booster synchrotron prior to moving on to the AGS.

The AGS itself is a synchrotron with an 807 m circumference. It, like the Booster, uses alternating quadrupole magnets to focus the beam. These quadrupoles cause a gradient in the magnetic field in the plane perpendicular to the beam direction. The net transverse magnetic field is zero at the center, so ions which are on the ideal circular path in the synchrotron are not diverted. Ions which have drifted away from the center are focused in an ellipse by the quadrupole. The subsequent quadrupole magnet is rotated by 90 degrees so that the beam is compressed along the other transverse axis. This strong (alternating) focusing technique earns the AGS its name. The AGS accelerates ions up to 9 GeV per nucleon.

The beam next passes through AGS To RHIC (ATR) transfer line, where a filter foil strips the Au of its final two electrons to produce Au^{79+}. At this point, the ion beam is split into bunches by switching magnets. The bunches are alternately sent down the two RHIC rings ('blue' and 'yellow') so the bunches travel in opposite directions around the RHICH ring. The final acceleration in the RHIC rings is 100 GeV/u for a total $\sqrt{s}_{NN} = 200\,\mathrm{GeV}$ per collision.

The collider has a design luminosity of $L = 2 \times 10^{26}\,\mathrm{cm}^{-2}\,\mathrm{s}^{-1}$ for Au-Au collisions at this maximum energy. The circumference of the RHIC ring is 3834 m, which is chosen because it is 19/4 times that of the AGS. That is the ratio of the number of ion bunches desired in each RHIC ring relative to the number in the AGS. This facilitates injection of ions from the AGS into the RHIC rings.

In RHIC, ion bunches are steered by magnets to cross at the 6 interaction points every 220 ns. This corresponds to a crossing rate of 4.55 MHz. Each bunch contains about 7.5×10^{8} ions. The luminosity is the flux of particle pairs, i.e., the number of particle crossings per unit area per unit time and is equivalent to $L = f\frac{N_1 N_2}{A}$, where f is the frequency of bunch crossing, N_1 and N_2 are the number of particles in each intersecting bunch, and A is the transverse area of the interaction region. So, the design luminosity above corresponds to a interaction area of about $A = (4.55 \times 10^{6}\,\mathrm{s}^{-1})(7.5 \times 10^{8})^{2}/(2 \times 10^{26}\,\mathrm{cm}^{-2}\,\mathrm{s}^{-1}) = 0.013\,\mathrm{cm}^{2}$, or a diameter of about 1.3 mm. The total interaction rate is $L\sigma_{NN}$, where σ_{NN}, the total Au-Au cross section, is about 7.2 barn. [26] So, the interaction rate is about $(2 \times 10^{26}\,\mathrm{cm}^{-2}\,\mathrm{s}^{-1})(7.2 \times 10^{24}\,\mathrm{cm}^{2}) =$ 1440 Hz.

2.2 The STAR Experiment

Our work is conducted at the Solenoidal Tracker at RHIC (STAR). The STAR detector consists of a large solenoidal magnet, surrounding an array of detectors. Fig. 2.2 shows the configuration of the STAR Experiment at the time of this research. STAR has since undergone a number of upgrades including an upgraded silicon complex which will be highlighted later in this dissertation.

2.2.1 TPC

The Time Projection Chamber (TPC) is the main tracking detector in STAR. With a diameter of 4 m and a length of 4.2 m, it was the largest such detector in

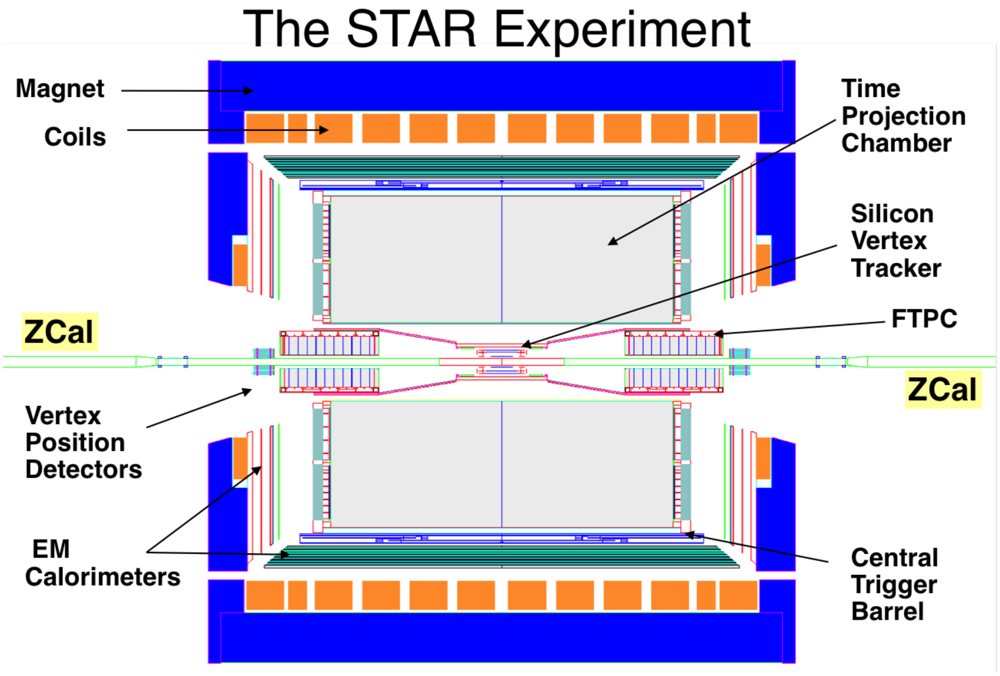

Figure 2.2: Configuration of STAR during Run VII

the world until the ALICE TPC was built in 2010. It provides full coverage around the beam line, and provides complete tracking out to ±1.8 units of pseudorapidity in the center-of-mass frame of the collision. A central membrane held at -31 kV at $z = 0$ splits the TPC into two halves and produces electric fields pointing in opposite directions resulting in negatively charged ions drifting toward opposite ends of the TPC. The TPC records an image of any particle with a momentum greater than 100 MeV that traverses the gas in the TPC, and can handle up to 3000 such tracks per event. The tracks imaged in the TPC consist of a combination of primary tracks caused by particles produced in a collision as well as secondary tracks produced by the daughter particles of primary particles that decay either within the TPC or before they enter the TPC.

As particles traverse the P10 gas (90% Argon, 10% Methane) within the TPC, they ionize gas molecules. The electron from the ionized gas molecule drifts through the very uniform longitudinal electric field created by holding the central membrane of the TPC at -31 kV while the endcaps are grounded toward the end of the TPC until it reaches the pad planes (see Figure 2.3). The 2 pad planes at opposite ends of the TPC each consist of 12 sectors. Each sector has 45 rows of pads. The sectors are divided into inner ($60 < R < 127\,\mathrm{cm}$) and outer ($127 < R < 189\,\mathrm{cm}$) subsectors. The pads are in fact MultiWire Proportional Chambers (MWPCs). Under normal operation, the drifting electron is accelerated toward the anode wires until it has enough energy to ionize another gas molecule. Both electrons are accelerated, ionizing more gas molecules as they traverse the TPC. Near the $20\,\mu\mathrm{m}$ anode wires, the electrons are subject to a very high electric field and are strongly accelerated. This avalanche deposits charge on the anode wires when the electrons are grounded out there. This charge induces a current in the pad below the wire; the induced current is the raw data measured by the TPC. The benefit of the Argon in P10 gas is that it is easily ionized. The Methane acts as a quencher. Gas molecules excited by the drifting electrons may revert to a ground state, emitting an energetic photon. Without a quencher, this photon would cause further ionizations in the TPC volume, leading to additional avalanches which were not caused by particles in the event. An organic quencher is a highly efficient absorber of these photons, and it ensures that the only avalanches come from primary electrons due to ionization by a particle produced in the event. The innermost set of wires in the MWPC is the gating grid, which keeps electrons from entering the avalanche region until the TPC is ready to take data and keeps positive ions from the avalanches from drifting into the TPC drift volume, where they could distort the precise electric field. An electron from a primary ionization may have to drift as much as 2 m before reaching the pad plane to be detected. The electric field in the drift volume must be as homogeneous as possible.

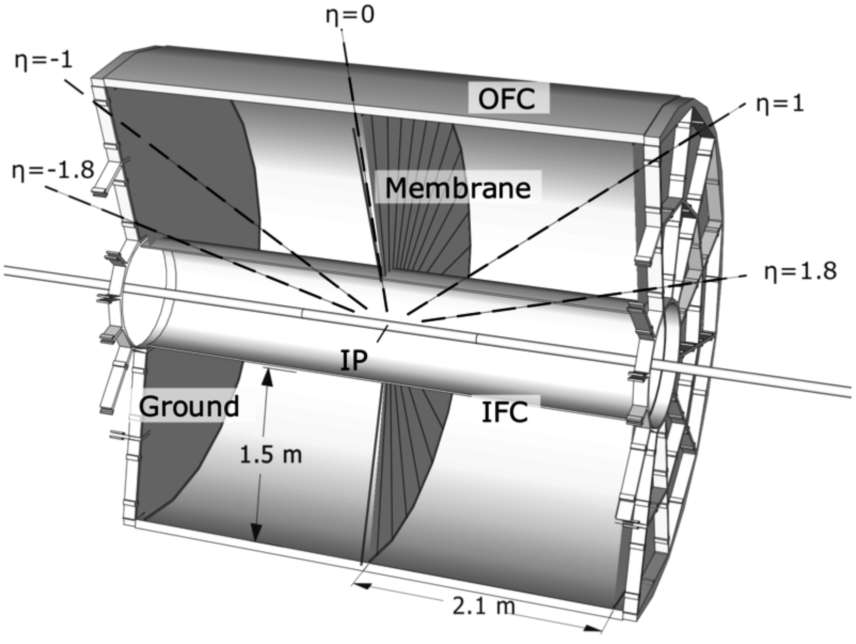

Figure 2.3: STAR TPC

These MWPCs operate in proportional mode, meaning that the gain is in a moderate region where the charge deposited on the pad goes linearly with the magnitude of the ionization produced in the drift volume. That means that the total charge deposited by an ionizing particle on the pad plane is proportional to the amount of energy loss (dE/dx) it incurred while passing through the TPC. This quantity depends mainly on the velocity of the particle (not the momentum), and so it can be used with some success to differentiate particle species in the region where the momentum does not greatly exceed the mass. The TPC provides three dimensional data. The pad spacing along a row is 3.35 mm (Inner sector) or 6.75 mm (outer sector). The spacing of the padrows is 50mm (inner sector) or 20 mm (outer sector). Total density is limited by electronic readout capability. The geometry above represents a balance between better energy loss (dE/dx) information in the outer sector, and better space point resolution in the inner sector. The high pad density along the inner sector padrows places a limitation on the number of rows which can be served by the readout electronics; thus the density of padrows is lower here. The z position is determined by the time the primary electrons take to drift from the original ionization point. Data is recorded in up to 512 'time buckets,' each corresponding to about 1 cm in z (based on the drift velocity determined by the electric field). The spatial information can have higher resolution than the spacing of pads or time buckets. One may fit a Gaussian to adjacent pads or time buckets to find the center of the distribution. Resolution along the padrow is about 0.4/,mm in the inner sector and 0.6 mm in the outer sector. That along the drift direction is 0.9 mm in the inner sector and 1.2 mm in the outer. These are for particle trajectories which cross the padrow at right angles. Polar or azimuthal inclination will increase the uncertainty in the drift and padrow directions, respectively, because the distribution of charge at the anode planes will be spread out over several pads or time buckets. The maximum resolution in the radial direction is fixed at the padrow width because no finer position information is available. There is an inherent uncertainty in position because of the diffusion of a cloud of electrons produced by an ionizing particle as it drifts through the TPC to the pad plane. The transverse diffusion is about 3.3 mm for electrons which drift the maximum 210 cm. The longitudinal diffusion is about 5.2 mm[27].

2.2.2 STAR Magnet

Measuring the momenta of tracks in the TPC requires a strong, uniform magnetic field in order to resolve the curvature of high momentum tracks. Consisting of 10 Main coils and two Space Trim coils, all of which are connected in series and draw a current of more than 5000 A at the maximum field strength (0.5 T), the STAR magnet produces a very uniform field along the z axis over the range $0.25 < |B_z| < 0.5\,\mathrm{T}$. To help maintain field uniformity, the Pole-Tips also contain Trim Coils, which draw a total of 1330 A at maximum field strength. In addition to providing STAR's magnetic field, the magnet's structure also serves as a rigid support structure to mount all other elements of the STAR detector[26].

2.2.3 SSD

The Silicon Strip Detector (SSD) is located between the TPC and the SVT. It provides two-dimensional hit position and energy loss measurements for charged particles, improving the extrapolation of TPC tracks through hits in the SVT. The SSD has a radius of 23 cm from the beam axis and covers a pseudorapidity range of $|\eta| < 1.2$. Its design is based on two clamshells each containing 10 carbon-fiber ladders. Each ladder is composed of 16 detection modules along the beam axis, two pairs of ADC boards and a C2D2 board located at the ends of the ladder. A low mass carbon fiber beam supports the modules, electronic boards and additional mechanical pieces which are used to attach the ladders and air cooling tubes. The 20 carbon fiber ladders are tilted 5 degrees about their long axis, allowing the ladders to overlap slightly in the transverse to help reduce the number of tracks that pass through the spaces between the ladders without hitting a module. The 16 detection modules on each ladder use a double-sided silicon strip technology with 768 strips per side and these modules are glued on the carbon ladder. Each ladder is 1060 mm long with a triangular cross section with a base of 40 mm. The ladders are made of carbon fiber which gives good rigidity and allows low material budget. The wafers are 75 mm by 42 mm sized and 300 μm thick[29]. The clamshell structure allows the SSD to be installed or dismounted easily. The SSD uses air cooling by routing air flow through the center of each ladder's structure. Tape automated bonding (TAB) technology was used to connect the detectors to their front-end electronics.

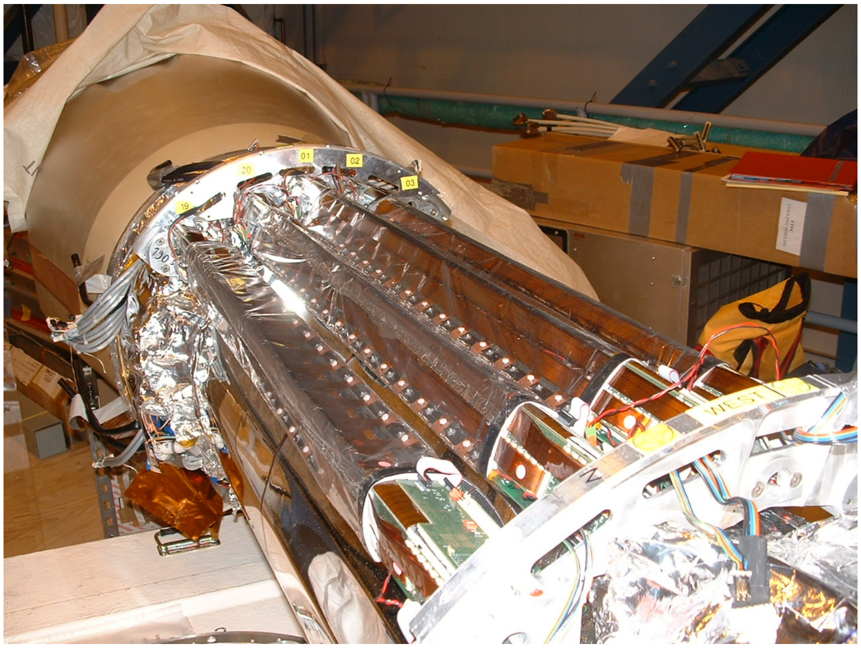

Figure 2.4: STAR SSD

2.2.4 SVT

In order to enhance the physics capabilities of the STAR TPC, a microvertex detector Silicon Vertex Tracker (SVT), shown in Fig. 2.5 is placed inside the TPC

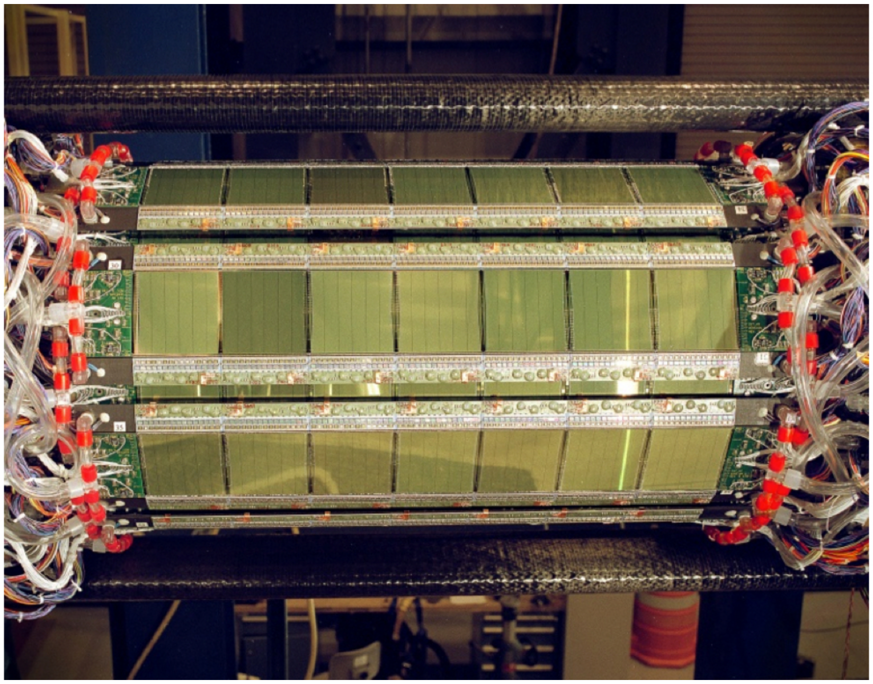

Figure 2.5: STAR SVT

around the beam line. It improves the primary vertexing, the two-track separation resolution, and the dE/dx measurement for particle identification. It enables the reconstruction of very short lived particles, primarily strange and multi-strange baryons and optimistically D mesons through secondary vertexing close to the interaction region, though the SVT was designed with strange physics in mind at the time. It also expands the acceptance for the low momentum primary tracks that do not reach the active volume of the TPC due to the applied magnetic field. Information from the SVT is advantageous both in high and low multiplicity environments; in the low multiplicity case, it can be an efficient primary vertex finder, and can rectify for the problem arising due to the wide distribution of collision vertices along the beam direction. On the other hand, the highly pixelated nature of the SVT ensures good two-track resolution in high multiplicity Au-Au events.

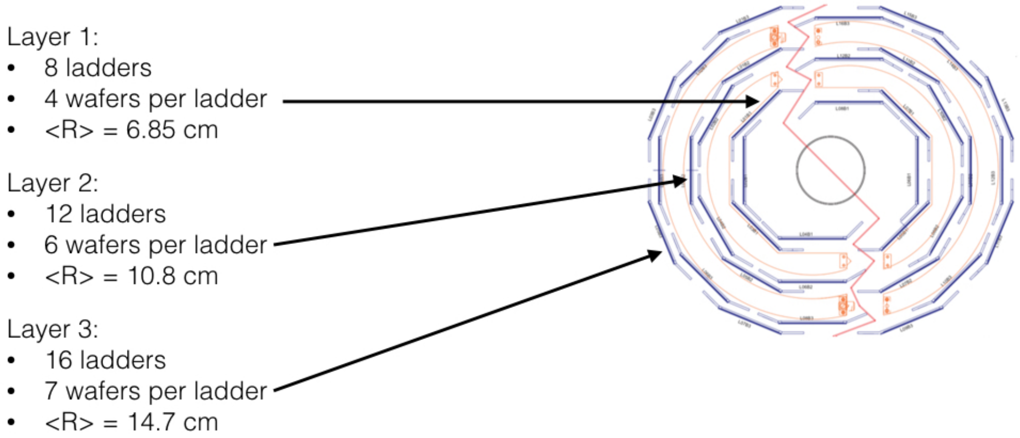

Figure 2.6: The configuration, number of ladders, and number of wavers per ladder in the STAR SVT. The SVT was built in 2 clamshells, the division of which is illustrated by the orange line.

The STAR SVT is based upon Silicon Drift Detector (SDD) technology. The SVT consists of three concentric barrels around the beam interaction region at radii of approximately 6.9, 10.8 and 14.5cm as shown in Fig. 2.6. These three barrels consist of 8, 12 and 16 ladders, respectively. Ladders are structures used to support the SDDs of the SVT. Each ladder is comprised of four, six, and seven wafers respectively in each of the three barrels. The active silicon length in the beam direction is 25.2 cm for the inner barrel, 37.8 cm for the middle barrel and 44.4 cm for the outer barrel.

The whole detector consists of 216 wafers arranged on 36 ladders to give complete azimuthal coverage in $|\phi| < 1$. The total average radiation length of the SVT is a little below 6% for all three layers or 1.89% per layer[30].

An SDD may be envisioned as a solid-state time projection chamber. It is a charged particle position measuring device with a position resolution of 20 μm in each coordinate. The SDDs are made of highly homogeneous neutron transmutation doped (NTD) 4-inch n-type silicon wafers. Each SDD has a thickness of 280 μm and are 63 mm×63 mm, consisting of a drift region and a focussing region. A charged particle crossing the detector creates electron-hole pairs. The holes are immediately absorbed by cathodes on the surface of the detector. Electrons converge to the middle of the bulk and drift at a constant speed under the influence of an applied uniform electric field towards the readout anodes. The current signal is then read through appropriate preamplifier electronics. The hit anodes determine the y coordinate of the hit and the drift time from the initial particle hit until the read-out of the signal determines the x coordinate of the hit. The SVT consists of two half-detectors separated by the dividing central cathode that receives the maximum voltage bias. Electrons in the half detectors drift in opposite directions from one another. This design limits the maximum drift voltage by limiting the maximum drift distance. The SDD's response is sensitive to certain environmental conditions such as the drift electrical field, the temperature, and the external magnetic field. The challenge is maintaining a highly linear drift velocity across the detector, which depends on the above quantities. Typical position resolution values obtained across the detector are 2 and 25μm in the anode and drift directions, respectively. In addition to the position measurement the detector also yields an energy loss measurement on the basis of charged particle energy loss in each layer. It is estimated that the dE/dx resolution of the SVT is about 7%.

Each ladder of the SVT is mounted in two edge locations onto the SVT beryllium end rings. It enhances the tracking capabilities of the STAR Experiment by accurately measuring the two-dimensional hit position and energy loss of charged particles. The full SVT was completed and was installed in STAR during the 2001 run. It is now retired from STAR and has been replaced by the silicon vertex detector upgrade, HFT (Heavy Flavor Tracker).

Calibration and Alignment (SVT)

Measuring particles such as the D^0 that decay very near to the primary vertex requires precision measurements, therefore careful attention must be paid to the alignment of the detectors along the path of the particles. Operations such as ramping the current in the STAR magnet can impose Lorenz forces on the detectors altering their orientation, which was shown to be the case with the SSD. The SSD was subject to shifts of several hundred microns with the location of the detector remaining stable during data collection runs, shown in 2.1 in order of increasing magnetic (B) field strength, along with the deviations from the initial alignment with the magnet and detectors powerd down (top half of 2.1). 2.1 displays the spatial shift in hundreds of μm and rotational shift in mrad of the entire SSD by calculating the average shift of each ladder in each sector of the SSD. The Cu-Cu run with no field was the initial run of the series (upper part half of the table). Note that after all detectors are powered up into their data collection mode that the SSD shifted in orientation slightly. Similarly, the other runs result in shifts of their own. In order to optimize the pointing accuracy of the tracks, a set of alignment procedures was produced.

	Average spatial and rotational deviation of all SSD sectors by run																			
	Before STAR magnet and detectors powered up																			
	CuCu200RF					CuCuNoField					CuCu200FF					CuCu62FF				
	B = -1					B = 0					B = 1					B = 1				
	A	FE	E	W	FW	A	FE	E	W	FW	A	FE	E	W	FW	A	FE	E	W	FW
x(100μm)	3	4	4	5	5	0	0	0	0	0	-1	0	-1	-1	-1	0	1	1	3	3
y(100μm)	6	7	5	7	7	0	0	0	0	0	1	2	-1	-1	-1	2	1	1	1	2
z(100μm)	-2	-2	-3	-5	-4	0	0	0	0	0	-2	-2	0	-1	0	-1	-2	1	-2	0
α(100mrad)	0	-1	0	0	0	0	0	0	0	0	0	0	0	0	0	0	0	0	0	0
β(100mrad)	0	0	0	0	0	0	0	0	0	0	0	0	0	0	0	0	0	0	0	0
γ(100mrad)	-6	-5	-5	-5	-5	0	0	0	0	0	-3	-3	-1	-2	-2	-3	-3	-3	-3	-3
	After STAR magnet and detectors powered up																			
	CuCu200RF					CuCuNoField					CuCu200FF					CuCu62FF				
	B = -1					B = 0					B = 1					B = 1				
	A	FE	E	W	FW	A	FE	E	W	FW	A	FE	E	W	FW	A	FE	E	W	FW
x(100μm)	3	4	4	3	3	0	0	0	-2	-2	-1	0	-1	-3	-3	1	1	1	1	1
y(100μm)	4	5	3	4	4	-3	-2	-1	-3	-3	-1	0	-3	-4	-4	-1	0	0	-2	-1
z(100μm)	-3	-2	-3	-3	-5	1	2	0	2	0	-1	0	-1	1	-1	0	1	0	0	0
α(100mrad)	0	-1	0	0	0	1	2	0	2	0	-1	0	-1	1	-1	0	1	0	0	0
β(100mrad)	0	0	0	0	0	0	0	0	0	0	0	0	0	0	0	0	0	0	0	0
γ(100mrad)	-2	-2	-2	-2	-2	3	3	3	3	3	0	0	1	1	1	0	0	0	0	0

Table 2.1

Initial data with the SVT gave a spatial resolution of $\sigma_{\rho\phi} \approx \sigma_Z \approx 200\mu$m, which poses a problem for direct charm measurements, particularly in the case of the D^0 measurement because the mean $c\tau$ of the D^0 is approximately 100 μm and the mean decay length of the D^0 in STAR is approximately 80 μm, as discussed later in the section describing the secondary vertex reconstruction in Chapter 3, and shown in Fig. 2.11. To reliably reconstruct these tracks in central Au+Au collisions with 2000 tracks per event, a Distance of Closest Approach (DCA) near the mean decay length of the D^0 or smaller is needed. The DCA resolutions in the XY ($\equiv \rho\phi$) plane (σ_{DCA}), a.k.a. bending or transverse plane and along the beamline or non-bending plane (σ_Z) are calculated using Equation

$$\sigma^2_{DCA} = \sigma^2_{vertex} + \sigma^2_{track} + \sigma^2_{MCS}, \tag{2.1}$$

where $\sigma^2_{vertex} \approx 600\mu\mathrm{m}\sqrt{N_{goodTracks}}$, $\sigma_{track} \approx 2\times\sigma_{XY}$, and $\sigma_{MCS} \approx 170\mu$m/p(GeV/c). $\sigma_{vertex} \approx 20\mu$m for central events and 100μm for minimum biased events. Because the track pointing resolution should be comparable to with MCS at 1GeV, it follows that the detector resolution after alignment should be, $\sigma_{XY} < 80\mu$ and $\sigma_Z < 80\mu$m, in both the bending and non-bending planes[31].

The calibration and alignment procedure is an iterative process of calibration, consisting of 4 steps, measuring the average drift velocities of the silicon wafers, using them to check alignment of the detector and repeating. Alignment occurs at the ladder level, which neglects effects, such as twisting of the ladder and gravitational or stress related sagging (or bowing) of the ladder. The alignment procedure assumes that the hit position deviations are linearly proportional to the misalignments through derivatives of the track projections to measurement with respect to misalignment parameters using a first order Taylor expansion and works quite well as long as the starting point is not far from the minimum. Well defined primary tracks are used for the alignment because they point back to the primary vertex and reduce systematic error introduced by using secondary tracks.

Average SVT Drift Velocity: The first step of the procedure is to calculate an average drift velocity per wafer. Because each wafer has a relatively sharp cutoff at t_0 and t_{max}, as shown in Fig. 2.7 the average drift velocity can be calculated as the total drift length divided by the amount of time between t_0 and t_{max}, $v_D = L/(t_{max} - t_0)$.

TPC Only Tracks: The TPC only tracks are used to check the global alignment of the SSD with respect to the TPC as a whole as well as the global alignment of the SSD sectors.

TPC + SSD Tracks: The TPC and SSD track information are used to check the global alignment of the SVT as a whole as well as the global alignment of the SVT Clam Shells and local alignment of the SVT Ladders. SVT drift velocities are updated. Fig. 2.8 shows the local alignment of an SVT Ladder where the slope, γ corresponds to a rotation around the local Z axis.

TPC + SSD + SVT Tracks: Track data from all three detectors are used to

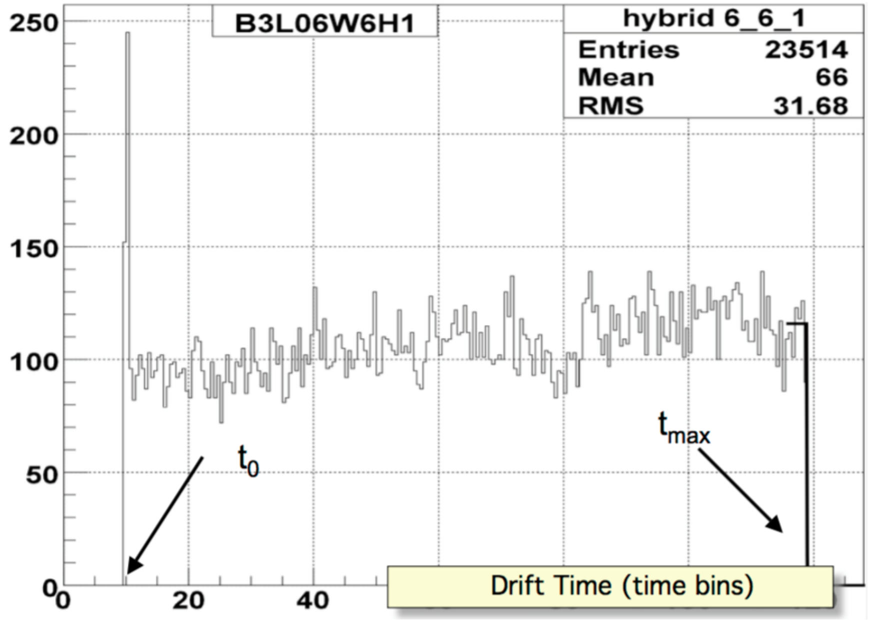

Figure 2.7: An example drift time distribution used for average drift velocity estimation via the charge step method.

check for consistency and reevaluate SVT and SSD hit errors.

Since D^0 mesons are short-lived particles, track information close to the interaction vertex is needed for its reconstruction. Run VII used the Silicon Vertex Detector, 3-layer SVT and a 1-layer SSD during data collection. We use the track hit data from the silicon detectors together with the TPC track data for the pointing resolution. Pointing resolution refers to the impact parameter resolution of primary tracks to the primary vertex, it is the heart of the μvertexing method. Since silicon hits provide track information close to the beam pipe, they provide better resolutions. Thus, track hits in the silicon layers are very important for our analysis.

During the first step in the reconstruction process, the daughter tracks are extrapolated towards the primary vertex. This allows us to find a point where the distance of the track to the primary vertex is a minimum, the Distance of Closest Approach

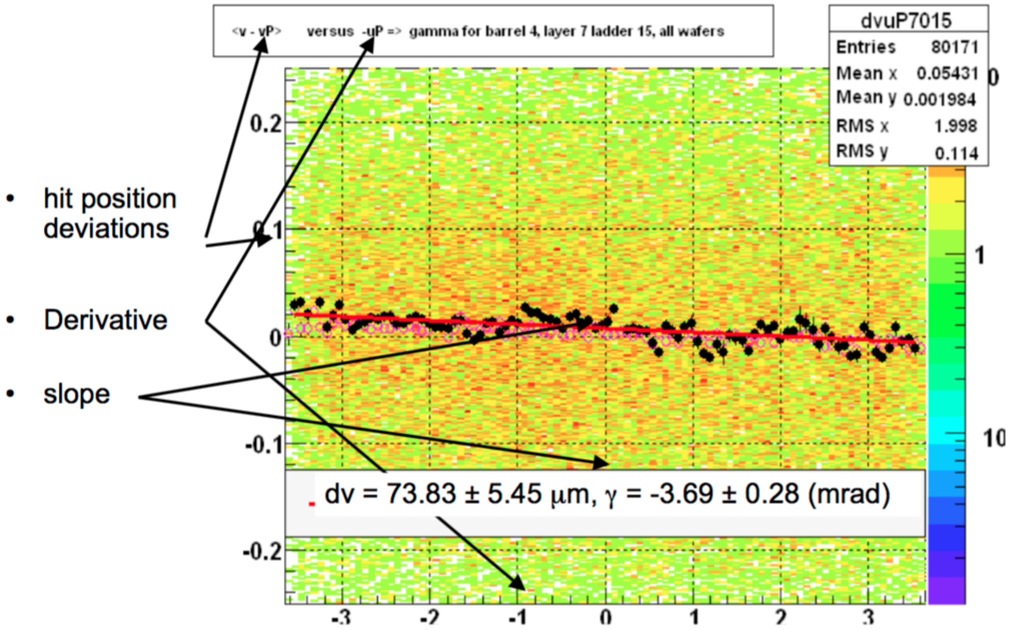

Figure 2.8: Example of local alignment: γ (slope) is the rotation around the w($\equiv$local Z) axis.

(DCA). The figure of merit used is the pointing resolution of this variable for reconstructed tracks ($\sigma_{DCA_{XY}}$, σDCA_Z). The DCA resolution gets better as the number of track hits in the silicon layers increases.

Silicon Hits Fitted to Track	σ_{XY}@1GeV/c (μm)	σ_Z@1GeV/c (μm)
0 - TPC only	3350	1184
1 - TPC+SSD	967	993
2 - TPC+SSD+SVT	383	351
3 - TPC+SSD+SVT	296	383
4 - TPC+SSD+SVT	280	344

Table 2.2: DCA Resolution for TPC and Silicon Detectors (SVT+SSD)

The top plot of Figure 2.9 shows the distribution of transverse DCA with increasing silicon hits. The bottom plot is the transverse DCA resolution versus $1/p_T$ as a function of silicon hits. At 1 GeV/c, the pointing resolution to the interaction point is

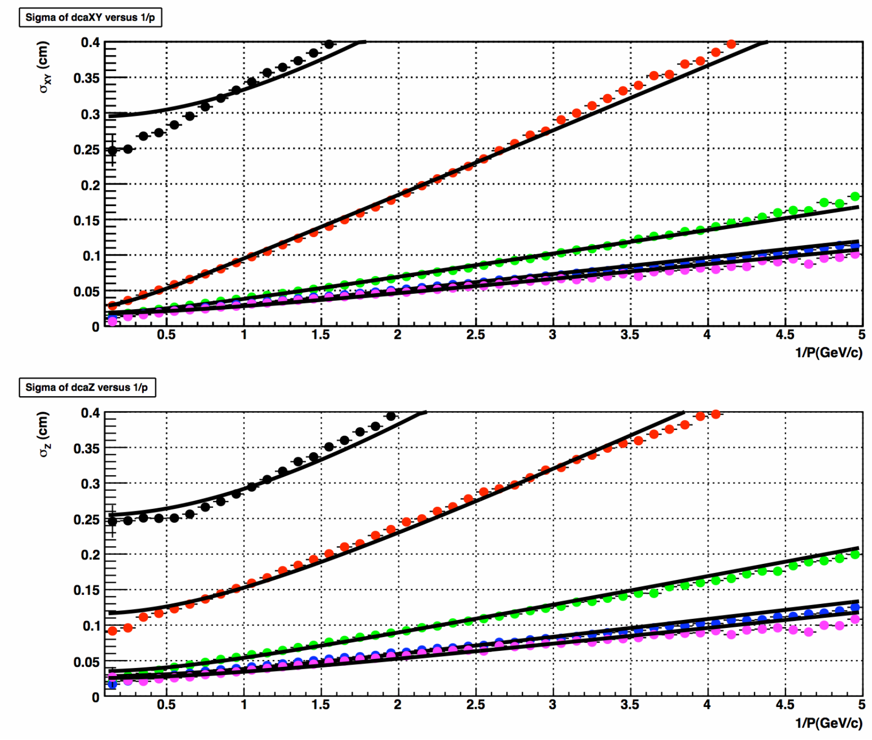

Figure 2.9: Distance of closest approach for global track with respect to the primary vertex in the xy (top) and z (bottom) planes for increasing numbers of silicon hits from 0-TPC only (black), 1-TPC+SSD (red), 2-TPC+SSD+SVT (green), 3-TPC+SSD+SVT (magenta)

$\sim 220\,\mu$m with track hits on all four silicon layers. Requiring hits on all layers of the SVT and SSD improves the DCA resolution by a factor of $sim12$ compared to tracking only by the TPC. Table 2.2 shows the measured values for the DCA resolution in the (XY) bending plane and the (Z)non-bending planes for all hadrons.

Now, in the HFT era, the DCA resolution is improved by a factor of $sim10$ compared to the best resolution of the TPC+SSD+SVT. The values in Table 2.3 show the averaged values of σ_{XY} and σ_Z for identified pions and kaons at 1 GeV/c (to compare to hadrons) in both sides of the detector, one of which has a mixture of Al and Cu cables, and the other with only Al cables[32]. The data presented are based on

DCA	(μm)	Cable Types
σ_{XY}	36	Al+Cu
σ_{XY}	34	Al only
σ_Z	34	Al+Cu
σ_Z	31	Al only

Table 2.3: Average σ_{XY} and σ_Z resolutions (μm) for hadrons with a momentum of 1 GeV/c with hits in the 3 layers of the IST and PXL detectors

pions and kaons that had the maximum number of hits (3) in IST+PXL. The values for identified pions and kaons were averaged to have numbers to better compare with the SVT era detectors. Note that since the hadrons have to pass through less material on the side of the HFT with only Al cables, the resolution on that side is slightly better.

2.2.5 Secondary Vertex Reconstruction

Figure 2.10 shows the schematic of the decay of $D^0(\overline{D^0})$ through their hadronic and semi-leptonic decay channels. We measure the hadronic decays (shown in the lower half of the decay diagram). D^0 s are very short-lived particles with $c\tau \sim 123\mu m$. For a realistic D^0 distribution at mid-rapidity, the mean transverse momentum, $p_T \sim 1$ GeV/c and the average decay length is 60-70 μm. However, the current detector resolution is $\sim 200\mu$m at 1 GeV/c at best. This results in huge background levels and therefore requires efficient background subtraction methods for signal extraction. Figure 2.11 shows the D^0 decay length distribution in the X-Y plane using a simulated data set consisting of pure signal events. As can be seen from Fig. 2.11, the distribution has a mean value of $\sim 65\mu$m. The role of the silicon detector complex including the SVT and SSD is to provide a few extra data points along particle tracks between the ID of the TPC and the event vertex, improving track resolutions.

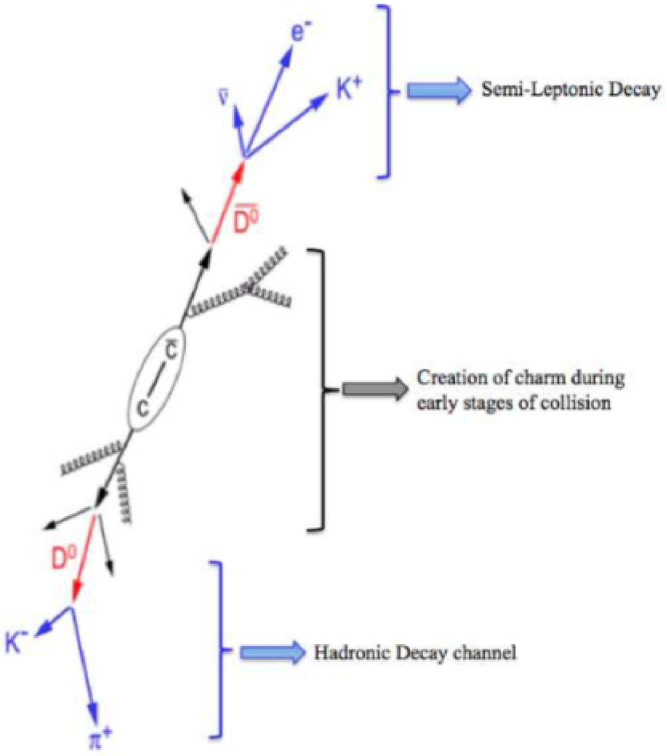

Figure 2.10: Possible ($\overline{D^0}$) decay diagrams

To reconstruct a $D^0(\overline{D^0})$ candidate, oppositely charged K and π tracks are paired. The invariant mass of a D^0 candidate can be determined from the measured momenta of the tracks and assuming the mass of the daughters using the formula,

$$M_{inv}^2 = M_+^2 + M_-^2 + 2(E_+E_- - \vec{p}_+ \cdot \vec{p}_-) \tag{2.2}$$

where the positive and negative subscripts refer to the positively and negatively charged daughter tracks (K and π) and c is taken to be 1. Details of the microvertexing techniques employed in this analysis can be found in Chapter 3.

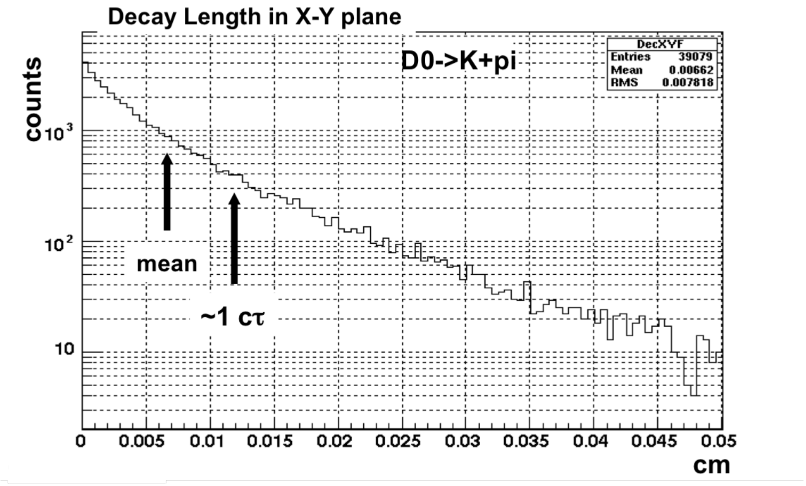

Figure 2.11: Transverse decay length of simulated D^0 mesons

2.2.6 The Heavy Flavor Tracker (HFT)

The HFT is the second generation of silicon vertex detector to reside inside the TPC, between the beam pipe and the inner field cage of the TPC. Its purpose, much like the SVT, is to extend the TPC tracks towards the event vertex by providing high precision points (hits) very close to the beam line. It consists of three different silicon technologies arranged in four layers as shown in Fig. 2.12.

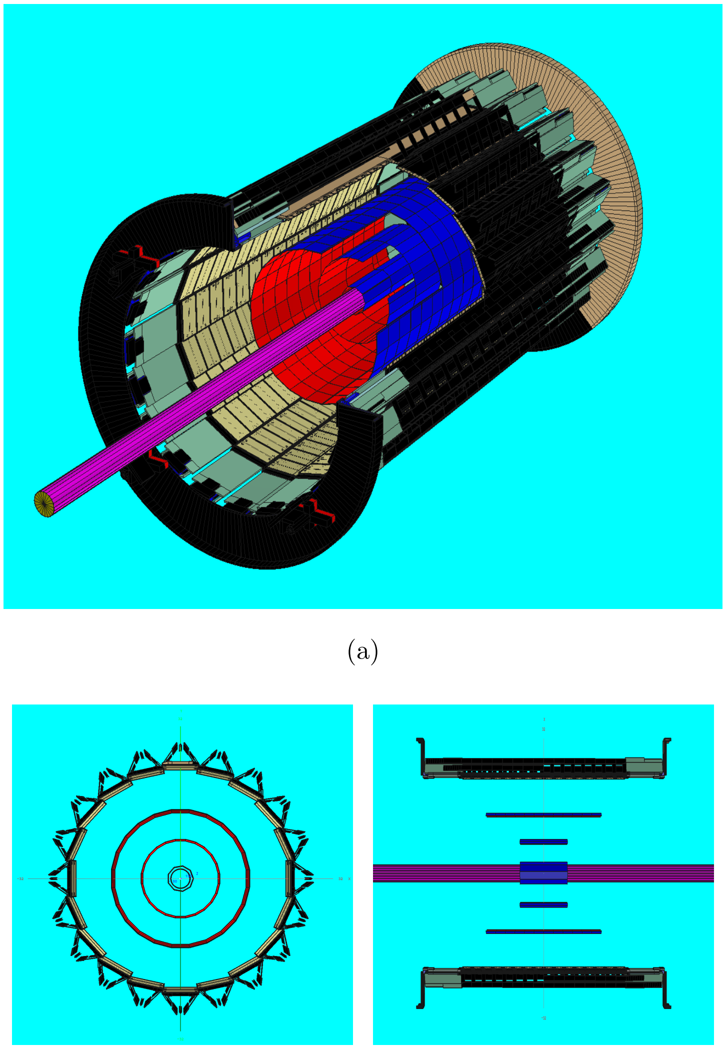

(a)

(b) (c)

Figure 2.12: A perspective (a), transverse (b) and side (c) view of a model of HFT in GEANT. The blue-red cylinders are the Pixel detector, the brown layer is the IST and the outer dark shape with the triangular shapes the SSD.

The outermost layer is the Silicon Strip Detector (SSD)[33], which has been modified for the HFT era. The SSD is still a double-sided silicon strip detector, made out of 20 ladders arranged in a cylinder, but now at a radius of about 22 cm from the beam line bringing the ladders 1 cm closer than the previous design. The SSD covers the pseudorapidity range of $|\eta| < 1.2$. Each ladder is composed of 16 sensors (wafers) along the beam axis, is 1060 mm long and air cooled. Each sensor has 768 strips per side crossing at 35 mrad. The resolution of SSD is about 30 microns in Rϕ and 800 microns in z direction.

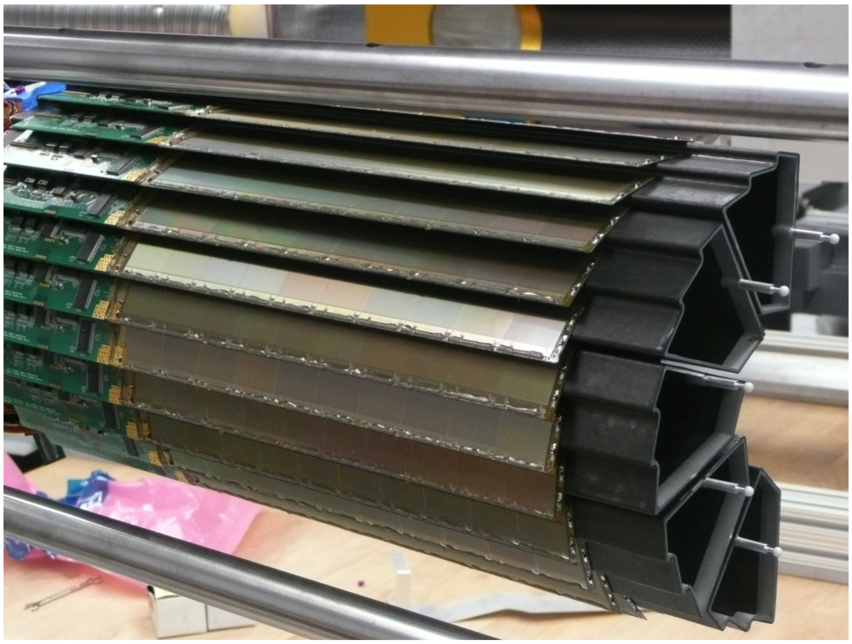

Figure 2.13: One half of the PXL detector mounted on the support/insertion structure. We can see the five carbon-fiber trapezoidal sectors and the outer ladders mounted on them and also the calibration balls on the right end used for survey purposes.

The next layer is the Intermediate Silicon Tracker (IST) which is a (single sided) silicon pad detector located at a radius of 14 cm. It is made of 24 ladders arranged in a cylinder. Each ladder has 16 sensors. The pad-size is $0.6 \times 6\,\mathrm{mm}^2$ resulting in an effective resolution of $170 \times 1700\,\mu\mathrm{m}^2$, where the high resolution side is on the transverse plane and the other along the z direction. The main purpose of the IST and SSD is to connect the tracks from TPC to the two inner layers, the PIXEL detector.

The Silicon Pixel Detector (PXL) is the two inner layers of HFT at 2.8 cm and 8 cm from the beam axis as shown in Figs 2.12, 2.13. It is based on the state-of-the art Monolithic Active Pixel Sensor (MAPS) technology with pixel size of about $20 \times 20\,\mu\text{m}^2$. Its hit resolution is better than ten microns in both $\text{R}\phi$ and z directions. It has a total of 40 ladders (10 inner and 30 outer) mounted on 10 trapezoidal carbon fiber structures (sectors). The sectors are mounted in two halves for insertion purposes. Each PXL ladder has 10 sensors of $2 \times 2\,\text{cm}^2$ size, so it has about 20 cm long active area. Each of the 400 sensors has about a million active pixels and it is thinned down to a 50 micron thickness in order to keep radiation thickness to a minimum. The average, total radiation thickness in the inner layer is less that 0.4% X_0. The position of each pixel inside the HFT has been surveyed and determined to an accuracy of better than 10 microns on average. The PXL detector has been designed so that can be replaced in about a day in case of radiation or other damage. The PXL detector defines the track pointing resolution and also determines the vertices position of secondary decay vertices very precisely.

2.2.7 Trigger and DAQ

The STAR Data AcQuisition (DAQ) electronics are capable of reading out entire events (ion collisions) at the rate of 100 Hz. As seen above, the bunch crossing rate is about 5 MHz, so some method of detecting events and deciding which ones to read out from DAQ must be found[53]. The actual Au-Au interaction rate is only about 1/3000 of the bunch crossing rate, so the first job of the trigger is to detect whether an interaction occurred during a bunch crossing. This is done mainly in the Level 0, 1, and 2 (L0, L1, L2) triggers[52]. These triggers get input from the 'Fast Detectors': a Central Trigger Barrel (CTB) and two Zero Degree Calorimeters (East and West ZDC). These detectors provide per-event information at the rate of 10 MHz, 5 orders of magnitude faster than the 'Slow Detectors', which include tracking detectors such as the Time Projection Chamber (TPC), the Silicon Vertex Tracker (SVT), and the Ring Imaging Cherenkov detector (RICH).

The CTB consists of 4 cylindrical bands, each of which contain 60 scintillator slats. It surrounds the TPC at a radius of 2 m. It covers the full azimuthal range and the pseudorapidity range $-1 < \eta < 1$. It serves to measure charged particle multiplicity. The ZDCs, common to all RHIC experiments, are hadronic calorimeters which use fiber optics to detect Cherenkov light from the core of the hadronic shower. They are located 18 m away on either side of the interaction region and cover a small solid angle at $\theta = 0$ and $\theta = \pi$. They are behind the dipole magnet, which steers the two RHIC beams back into the ring from the interaction region. Thus, only neutral particles (primarily neutrons) are detected in the calorimeters. Each ZDC has 3 modules, and both ZDC signals are summed to determine if an interaction occurred. The ZDCs can be used to estimate the longitudinal position of the collision vertex by comparing the timing of the signals from the East and West modules.

These fast detectors provide information to the Trigger hardware every time a bunch crossing occurs. The basic 'Hadronic Minimum Bias' (minbias) trigger is an L0 trigger that simply requires coincidence of signals in both the East and West ZDCs. This is designed to collect as many events as possible while introducing little bias with respect to centrality, etc. The 'Central' trigger is also a fast L0 trigger; it is designed to capture higher multiplicity events (i.e., more central collisions). It requires either a high CTB count alone or high counts in the CTB and ZDCs. The option exists because, for the most central collisions, few particles are produced at small polar angle, and the ZDC signal is small. The L0 trigger is programmed to trigger on a given number of Central and Minbias events in accordance with the data requirements of STAR. Once the conditions for an L0 trigger have been met, the various slow detectors begin digitizing their data. This takes several milliseconds, and during this time, the L1 and L2 triggers perform more comprehensive analysis of the output from the fast detectors. More complicated selections may be made, and the event may be aborted if it does not not meet the L1 and L2 trigger requirements. This causes the slow detectors to stop digitizing and prepare for another L0 trigger.

The Level 3 (L3) trigger uses data from the slow detectors once it is digitized and actually performs a fast reconstruction of the event[54]. This means that the L3 trigger software turns the pixel information from the tracking detectors into particle trajectory information, and ultimately particle identification (PID) data. It can then accept or reject the event on more complicated triggers such as the position of the interaction vertex, the particle multiplicity, or individual particle momenta. The L3 reconstruction allows the immediate display of events in the STAR control room.

Chapter 3

Data Analysis

In this chapter, the analysis methods used for the direct measurement of charmed mesons, specifically $D^0(\overline{D^0})$ are discussed. The discussion will begin with an introduction to the methods used to produce the data that are analyzed with our techniques, and continue on to discuss our analysis methods. The methods used in our analysis implement a microvertexing technique, which utilizes track information from the TPC, SSD and SVT for the direct topological reconstruction of $D^0(\overline{D^0})$, through the decay channel, $D^0(\overline{D^0}) \to K^-\pi^+(K^+\pi^-)$. Microvertexing is the process of reconstructing the secondary vertex through a fit of the D^0 daughter tracks. The program uses various quality cuts to select good events and track candidates which might come from the decay of a $D^0(\overline{D^0})$. These cuts were first imposed on simulated data files to optimize signal retention and then later they were applied to real data. This chapter includes details about the datasets, cut variables, and the cut sets used for our analysis.

3.1 Event Reconstruction

During an experimental run the Data Acquisition System (DAQ) is responsible for gathering, organizing and storing all the unprocessed (raw) information from all detector subsystems for each individual, triggered event. After the run is over a sample of the gathered data is analyzed for calibration and performance studies like the ones appearing in this thesis. When the calibrations are finished and the appropriate structures in the Data Base (DB) for each run are filled one can start the so-called DST production (DST=data summary tapes). The task here is to calibrate and process the raw information for each event and write out all the information that is needed for further physics analysis. Examples of information written out are the position of the event vertex in space, the multiplicity of the event, the momentum and direction of each track produced and their daughter tracks, etc.

Raw detector information is processed first into clusters or hits followed by tracking, if applicable. Then the event vertex is determined and tracks are fitted with the hypothesis that they originated from the vertex. If the primary vertex point is successfully included in the fit of the track, it is called a Primary Track. All other tracks are referred to as Global tracks. Other detector information is also associated with each track based on specific criteria.

3.1.1 Event Vertex Finding

After the tracking is finished, the next task is to determine the event or primary vertex (beams interaction point). There are two independent ways to determine the position of the triggered event vertex. One is based on TPC tracking information and the other is based on timing information between the two VPD detectors (on each side of STAR).

The task to find the event vertex using TPC tracks is straightforward. It is found by using the reconstructed global tracks and extrapolating them to a seed vertex, at the Distance of Closest Approach (DCA) space point which is the closest point of the global track helix from the seed vertex point. The seed vertex point is estimated by using the general z–coordinate pointing of the global tracks. Then, by using χ^2

minimization techniques on the sum of the track DCA, we can determine the position of the event vertex, the point that minimizes the average distance from the track sample.

The other way of determining the vertex position is by using timing information from the two VPDs that are on each side of STAR outside the TPC and just outside the beam pipe (see also Fig. 2.2). The particles that reach these detectors, traveling at near the speed of light, arrive at the VPDs at slightly different times, depending on the z-position of the primary vertex. The timing difference gives directly the z position of the vertex. More details on the VPDs can be found in Ref. [75].

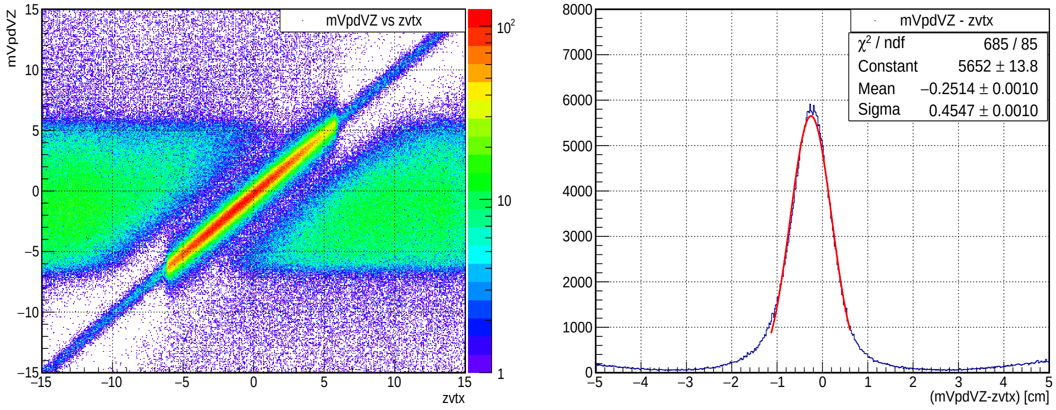

(a) (b)

Figure 3.1: The estimated z-position of the event vertex using the VPDs versus the same position estimated by using the TPC tracks (a) in the region of the HFT acceptance. The distribution of the difference between the two vertex estimates together with a gaussian fit [red line] is shown in (b). We observe a slight offset of 2.5 mm and a width of about 0.5 mm between the two estimates.

Figure 3.1 [left and right-upper panel] shows the correlation of the z location (beam direction) of the event vertex(V_Z) as reconstructed in the VPD vs that estimated by TPC tracking. The left panel is a large scale view of the distributions that covers the whole length of TPC. The right-upper panel is a zoom in version of the same correlation inside the acceptance of the HFT detector ($-10 < z < 10\,\mathrm{cm}$). The diagonal red band (triggered events) in the middle shows the nice correlation between the two reconstructed vertices. We also see that the red band extends to about $\pm 5\,\mathrm{cm}$. This is because the VPDs were in the trigger which was setup to accept only event that occur within 5 cm from the HFT center. Due to resolution effects the band actually extends to about another centimeter on each side. In order to find the combined system's resolution we need to look at the distribution of the difference between the two vertices. This is shown in the lower-right panel of Fig. 3.1. The gaussian fit of the distribution gives a σ_Z of about 5 mm with an overall shift (bias) of about 2.5 mm.

A V_Z quality cut of $\mid V_Z \mid < 5\,\mathrm{cm}$ was used in our analysis in order to avoid possible acceptance effects at the edges of the HFT detector. [what about a zvpd-ztpc cut?].

3.1.2 Tracking - Primary and Global Tracks

We will concentrate here on cluster/hit and track reconstruction in the TPC and SVT as the main tracking devices in the central region of the experiment. In the TPC the secondary electrons that are formed by collisions of the produced charged particles in the collision with electrons of gas atoms produce ionization clusters. These ionization clusters then drift towards the TPC end-caps where they get amplified and recorded. Offline software reconstructs these clusters on a 2+1 dimensional coordinate system defined by the TPC pad plane and the drift direction. The cluster is a blob of charge and a space-point is determined as the 'center' (weighted mean) of this blob which we call a 'hit'. The hits correspond to the points along the particle trajectory. Sometimes, in high multiplicity events, the clusters must be de-convoluted due to overlap into two or more individual hits.

The SVT hit reconstruction process is similar in the sense that ‘clusters’ are formed from raw data and then a centroid is determined, the hit coordinates. The SVT is made from three different technologies and the hit finding process is slightly different in each one. For example the SSD is a double-side silicon strip detector so first we make a list of ‘fired’ strip in each side and then we match the two sides based on geometry and charge information to form hit candidates. After that an algorithm decides which candidates are recorded hits. In the IST, a single layer silicon elongated strip detector, the hit is assigned to the geometrical center of the strip that was fired. The PIXEL detector typically gets several pixels fired every time a track crosses an active layer so after the cluster is identified the hit position is assigned to the geometrical mean position of the cluster, unweighted since the detector has only analog information.

The process of taking the reconstructed hits and combining them into tracks is called Global Tracking. The Global and primary tracks are the final step in the event reconstruction. This process starts typically in the outer part of the TPC where a short series of hits close to each other (a seed) is found. Finding these seeds in the low hit density regions of the outer pad-rows of a sector makes the seed finding more efficient. The global track finder fits the hits in the seed with a helix hypothesis and extends it (projects) inwards to the next padrow loooking for another hit. In this step the effects of Multiple Coulomb Scattering (MCS) and energy loss in the material crossed are taken into account. If one is found the whole string of hits is re-fitted and the process continues until all padrows are used. In reality of course this task is more complex especially in a high hit density environment and/or in the presence of gaps (dead padrows) in the detector.

After finishing tracking in the TPC the found tracks are extended to the outer layer of the HFT, the SSD, where silicon hits are now considered to be assigned to these tracks. The process continues inwards for all four layers of HFT. Typically after this outside-in tracking step is done it is followed by a clean-up, or 'filtering', step. The resulting sample of tracks is called *Global* tracks.

Based on the reconstructed global tracks in the event and extrapolating them to the beam line, one can find the primary vertex (the main interaction point where the collision occurred) as described below. After the event vertex is determined all Global tracks that point within 3 cm from the primary vertex are fitted with the hypothesis that they originate at the event vertex, i.e. they are fitted with the event vertex space point as a 'hit' on the track. If the fit is successful then the new, updated parameters of the track are saved in a track sample called Primary tracks for obvious reasons.

3.2 Particle Identification (dE/dx)

The Particle IDentification (PID) is a crucial aspect of most particle physics experiments. Special detectors are used that detect the unique signatures left by the stable particles as they pass through them. Charged hadrons can be identified from determining their mass and charge. The mass can be deduced from measurements of the momentum and the velocity or ionization. Momentum and the sign of the charge are obtained by measuring the curvature of the particles track in a magnetic field.

As elementary particles travel through the detector material they lose energy, aka dE/dx, through ionization production from collisions with atomic electrons. Another results of these collisions with the atoms is a small change in their direction, i.e.

MCS. We use the dE/dx information information to better identify the particle type from its mass and charge. In the following paragraphs we briefly describe the main features of these two particle identification methods.

We begin by discussing the dE/dx mechanism in some more detail. As particles traverse the detector media, gas in the TPC or silicon in the HFT etc, they collide with the atoms, i.e. interact electromagnetically with atomic electrons of the media, causing a loss of energy and the creation of what we call primary ionization (see also Fig. 3.2). In some of the hard collisions the atomic electron acquires such a large energy that it causes secondary ionization. Due to the presence of the external electric field the electrons will start drifting towards the TPC anodes at the edges of the detector where they get amplified and recorded and the positive ions towards the central membrane.

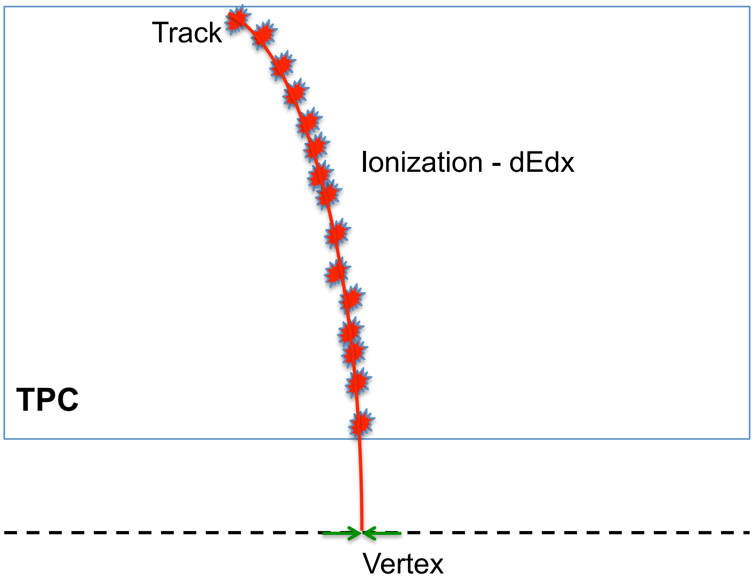

Figure 3.2: A sketch of ionization energy loss (dE/dx) in the gas volume of the TPC.

The rate of energy loss (also called stopping power) can be approximated by the Bethe-Bloch formula as shown below, (the Bethe-Bloch formula gives us quantitatively the amount of energy 'lost' or deposited by the particle on the average per unit length due to the numerous collisions it suffers as it passes through the material):

$$-\frac{dE}{dx} = Kz^2\frac{Z}{A}\frac{1}{\beta^2}\left[\frac{1}{2}ln\frac{2m_ec^2\beta^2\gamma^2T_{max}}{I^2} - \beta^2 - \frac{\delta(\beta\gamma)}{2}\right]$$

Here, $T_{max} = (2m_ec^2\beta^2\gamma^2)/(1 + \frac{2\gamma m_e}{M} + (\frac{m_e}{M})^2)$ is the maximum kinetic energy which can be imparted to a free electron in a single collision. Z is the charge number of medium, $K = 4\pi N_A r_e^2 m_0^2 c^2$ is a constant, z_e is the charge of incident particle, A is the atomic mass of medium, m_e is the electron mass, M is the mass of incident particle, $r_e(= \frac{e^2}{4\pi\epsilon_0 m_e c^2})$ is the classical electron radius, β is the particle's relativistic velocity (v/c), N_A is Avogadro's number, I is the mean excitation energy and δ is the density effect correction to ionization energy loss. Energy loss, however, is a stochastic process and so there are fluctuations in total energy loss.

In addition to energy loss, charged particles suffer Multiple scattering from nuclei through small angles which is called Multiple Coulomb Scattering (MCS). Moliere scattering was calculated during each iteration where the scatter away from the direction of propagation is defined as:

$$\theta_0 = \frac{13.6Mev}{\beta cp}z\sqrt{\frac{x}{X_0}}[1 + 0.038ln\frac{x}{X_0}]$$

Here p, βc, and z are the momentum, velocity, and charge number of incident particle, and$\frac{x}{X_0}$ is the thickness of the scattering medium.

Figure 3.3 shows the dEdx distribution as a function of track momentum. Clearly, the heavier particles bands protons and kaons have higher values of dE/dx than pions band has. The relativistic rise separates the electron dE/dx from the particles except at the crossover with protons at 1.12Gev/c, kaons at 0.6Gev/c and pions at 0.26Gev/c.

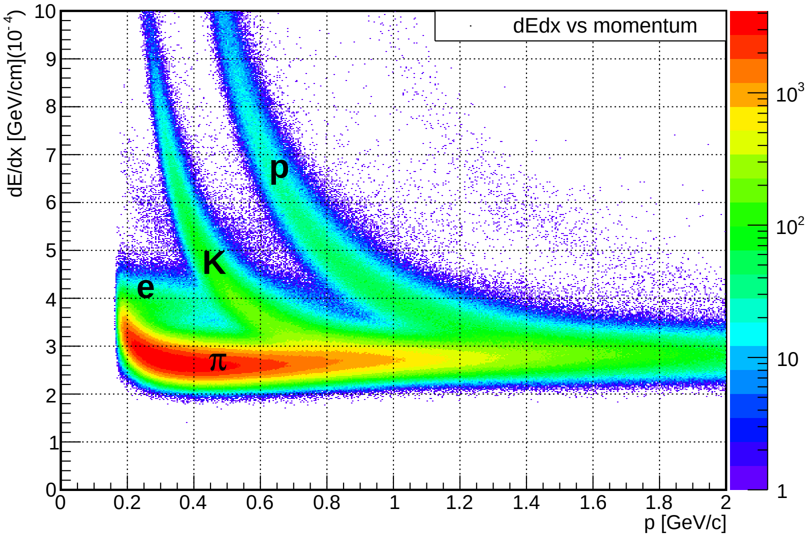

Figure 3.3: Energy loss [dEdx] as a function of track momentum.

3.3 Data Sample

We used three different data sets: pure D^0 events, D^0 mixed with $Au + Au$ HIJING events, and real data from Run VII Au+Au collisions at $\sqrt{s_{NN}} = 200\,\text{GeV}$. HIJING is a Monte Carlo event generator for simulating particle production in high energy hadronic and nuclear collisions based on QCD-inspired models for multiple jet production. Embedding data was used to do corrections for acceptance, efficiency etc. These corrections are discussed in Chapter 4 (see Section 4.4).

3.3.1 Real Data

The data used for this analysis is from year 2007 RHIC run (Run 7). Au+Au beams were collided at center-of-mass (CM) energy 200 GeV per nucleon. Run 7 included the inner silicon tracking detectors (SVT and SSD). This run had an additional change from previous years, which was the addition of the VPD detector to trigger on vertices less than 5 cm from the center of the detector along the z axis. This ensured the inclusion of vertices within the acceptance of SVT+SSD. The main production trigger setup names of this production are 2007 Production2, which contains mostly minimum bias but also rarer triggers, and 2007 ProductionMinBias, which contains minimum bias events (mb-vpd)5. Run 7 recorded 81 million events, out of which 62 million were ProductionMinBias events. Table 3.1 shows the data sample we selected:

Stream	Contents	Trigger Name	Detectors	Events
Physics	Prod2, ProdMinBias		TPC	81M
	Prod2, ProdMinBias	mb-vpd($\lvert V_z \rvert < 5$cm)		74M
	Prod2, ProdMinBias	mb-vpd		69M

Table 3.1: Data sample from the Run VII Au+Au run

3.3.2 Monte Carlo Data

In order to learn how the signal parameters behave, we used a sample of simulated 'pure D^0 events' where D^0 s were generated with transverse momentum of the following functional form in unit rapidity:

$$\frac{d^2N}{dp_T dy} = A\left[1 + \frac{p_T}{p_0}\right]^n, \tag{3.1}$$

where p_0 and n are two parameters, which are related to the mean transverse momenta by the relation: $\langle p_T \rangle = \frac{2p_0}{(n-3)}$. The value of $\langle pT \rangle$ is selected to be 1 GeV/c. This power law function was used to match the p_T distribution with the anticipated data spectrum [67]. Figure 3.4 shows the generated P_T distribution for various n values along with the real data distribution itself.

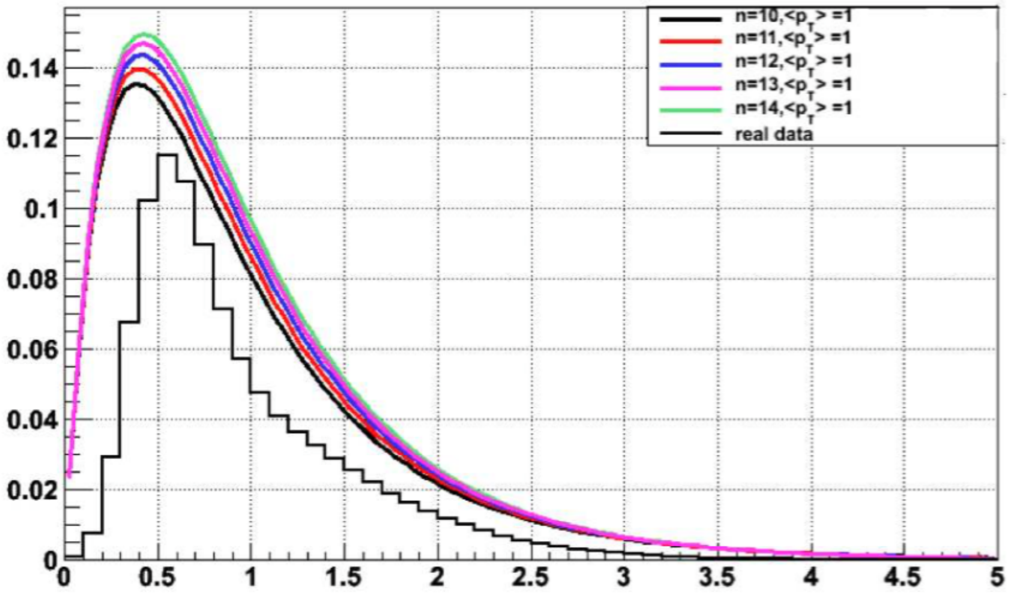

Figure 3.4: Power law p_T distribution of simulated D^0 mesons

We sample random values of this distribution for the transverse momentum of D^0 candidates. The parameters chosen are $n = 10$ and $pT = 1GeV/c$. The phase space characteristics of the D^0 s generated are: transverse momentum, $0 < p_T < 5GeV/c$, rapidity, $|y| < 1$ and flat distribution in azimuth, $0 < \phi < 2\pi$.

For background events we used central Au+Au HIJING events, with impact parameter, $b \leq 4.5fm$. HIJING does not normally produce charm mesons, therefore it is an ideal environment to study combinatorial background. The geometry used for running the 'Big Full Chain' (BFC)[2] was y2007g, which was the closest to the detector set up in Run 7. y2007g geometry uses the GEANT3 [68] (a software package used to simulate the passage of particles through matter) configuration with the TPC, SVT, SSD etc.[68], which are the main subsystems we utilized in order to get the pointing accuracy for the microvertexing method used here. This geometry also takes into account the dead material in the SVT. To study the signal in the presence of background, the D^0 particles generated with power law p_T distribution are mixed with HIJING events. Figure 3.5 shows the simulation phase-space settings for the generated D^0 s.

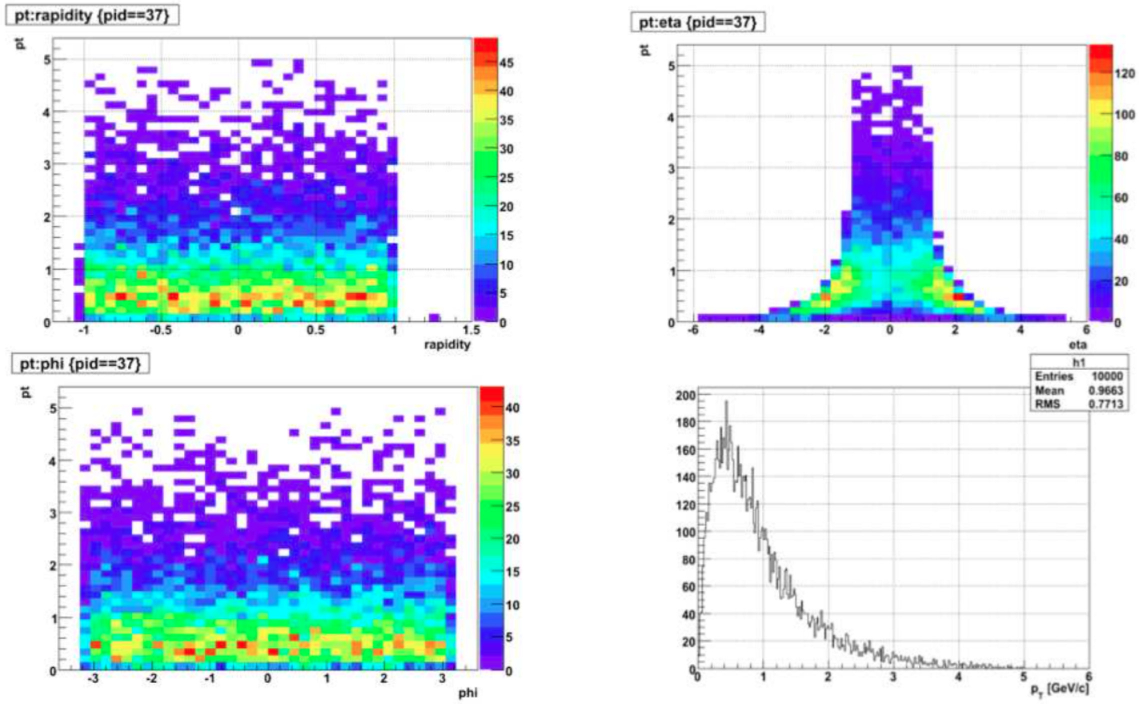

Figure 3.5: Phase space settings of the simulated D^0 mesons

3.4 Analysis Procedures

The analysis of data in STAR proceeds in two stages. In the first stage, the raw digitized detector data is processed with the reconstruction program, BFC (Big Full Chain). This process involves track fitting using different methods (see Appendix A) and the output is stored as `.Event.root` files. These tracks are organized and sorted to produce data summary tapes with information on detector hits, particle trajectories, momenta, hits, species identity, etc. as `.MuDst.root` files. The MuDst files are smaller root files that contain reconstructed particles and their properties. The second stage involves a detailed study of these reconstructed collision events in MuDst files to search for physics phenomena. The analysis procedure described in the following section is topological reconstruction of $D^0(\overline{D^0})$ from MuDst files, using microvertexing code.

3.5 Microvertexing

Microvertexing techniques were developed to handle the reconstruction of particle decays that occur near the primary vertex, before the parent particle reaches any detectors used for tracking. The D^0 is an strong candidate for the use of these techniques, because it has a short decay length, a mean of $0.65\,\mu$m (Fig. 2.11) in the STAR experiment. With $\approx$2000 tracks produced in a central Au-Au collision, the ability to distinguish D^0 daughter tracks from the kaons and pions produced at the primary vertex and other decays requires great precision in the reconstruction of the tracks. In an effort to deal with this issue, we compared DCA Geometry, Helix Swimming, and TCFit algorithms to better determine the trajectory of reconstructed kaons and pions. In chapter 4, a series of resolution studies are discussed as a means of comparing the results of the DCA Geometry, Helix Swimming, and TCFit techniques.

3.5.1 DCA Geometry

The tracks used in our analysis are Global Tracks, and as such, the tracks do not contain information about the primary vertex. Prior to the implementation of `StDcaGeometry` in Run VII, referring to the `StDcaGeometry` structure contained within `.mudst.root` files, tracks were only extrapolated back to the DCA of the first hit. The 'new' tracking method involves finding the global tracks and moving them through all material to the beam pipe center in the transverse plane, $(x, y) = (0, 0)$, to obtain full track information. The full track/error information is saved as `DcaGeometry`. A Kalman Filter machinery was run with `StTracks` to account for all of the dead materials from the inner field cage of the TPC, SSD, SVT, beam pipe, etc., which can account for Multiple Coulomb Scattering (MCS) as the tracks pass through the detector layers, and ensures that the helix manipulation is performed correctly. A geometric schematic of tracking with `StDcaGeometry` is shown in Fig. 3.6.

The transverse decay distance is the distance that the D^0 moves radially outward from the interaction point.

3.5.2 Helix Swimming

Helix swimming works much like V0 tracking, where oppositely charged identified particle tracks are paired and projected toward the primary vertex. If the tracks cross before the primary vertex, they are considered as D^0 daughter candidates. At this point some loose cuts can be imposed on variables such as the DCA of the parent track with the primary vertex to reduce fake candidates that are not pointing back

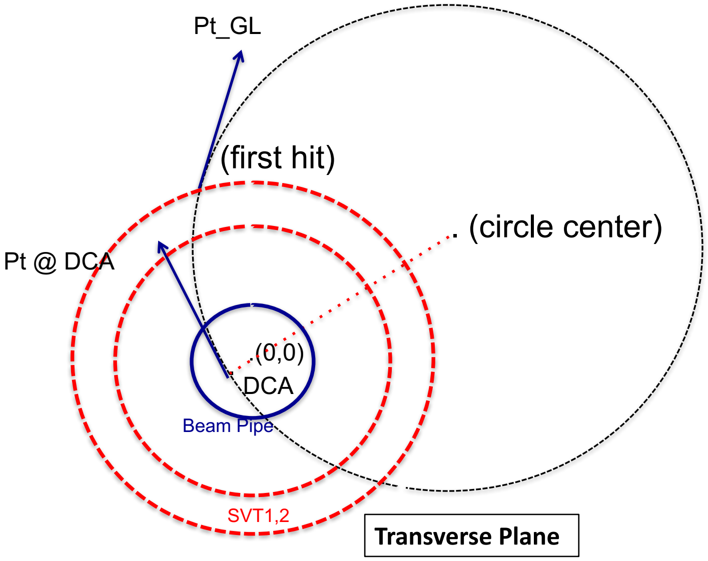

Figure 3.6: Schematic of `DcaGeometry` Tracking

toward the primary vertex.

3.5.3 TCFit

A third method uses the information gathered from the helix swimming method to perform a full D^0 vertex fit (TCFIT). This method is used in our final analysis. Fig. 3.7 shows the D^0 decay topology with the TCFIT constraints. The method uses a least squared fit of the decay vertex. Track parameters from DCA-Geometry provide information that is then used by the helix swimming methods to give an estimate of the decay vertex position. The kaon and pion daughter tracks are then fit with the constraint that they are coming from a common point, i.e. the momentum of the parent D^0 should point back toward the primary vertex. The solution to the fit is the one that minimizes the total χ^2. The fit calculates and updates the initial estimates of the decay length and its uncertainty obtained using the helix swimming method. The probability and χ^2 of the fit are also saved in the output.

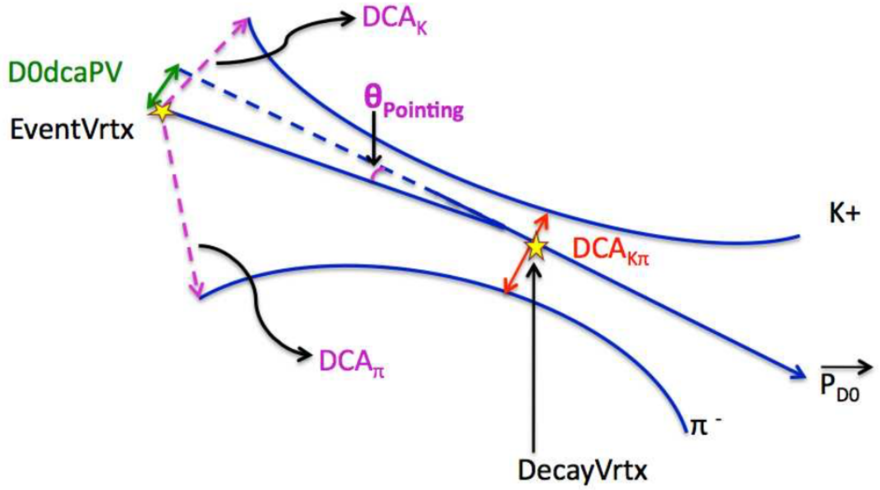

Figure 3.7: D^0 decay topology with TCFIT

3.6 Algorithms

The macro uses several loops to associate daughter tracks in the events stored in the data summary files (`.MuDst.root` files). While it iterates through the event structure, the code uses several quality cuts, both to reduce background and to speed up the run process. The first loop is over the events and the second loop is over all the vertices in that event. We select the best vertex assigned to that event during reconstruction (saved in `.MuDst.root` files) by a cut on `vertex index = 0` (a vertex index greater than 0 indicates a lower ranking vertex). Cuts on the vertex position and position resolution along the z-axis are also used. A third and a fourth loop within the third, are over the primary tracks to select K, π candidates. The loop over tracks makes no distinction between K and π tracks nor a distinction on the charge of the tracks. This is to accept both D^0 and $\overline{D^0}$ particles. The particle identification is obtained from the TPC dE/dx measurements, which will be discussed later. The primary tracks should correspond to the primary vertex index zero, or else it is rejected. In the next step, the global track corresponding to the primary track is selected and subjected to quality cuts and secondary vertexing. (Details on primary and global track are included in Appendix A.) In summary, the μvertex code proceeds in the following way:

1. Loop over event - select trigger
2. Loop over the primary vertices in the selected event and pick the vertex corresponding to index `i = 0`, apply vertex-level cuts to select good events.
3. First loop over primary tracks (index `k`). If the primary vertex index of the track does not equal `i`, it is rejected. For each primary track selected, the

global track associated to it is used - track-level quality cuts are applied.

4. Second loop over primary tracks, select a track different from the first. If the primary vertex index of the track does not equal `i`, it is rejected. The global track associated to the primary track is used - track-level quality cuts are applied.

5. Track pairs are subjected to secondary vertexing.

6. Apply cut on standard deviation of dE/dx bands to identify K and π tracks.

7. The D^0 candidate is built by combining K and π tracks that pass the cuts. For this, the momentum components are obtained from the global tracks and a `TVector3` class is used to save the momenta of the tracks. In the next step, we use the `TLorentzVector` class and save the momentum and energy of the track,

   ```
   p4[0][0].SetVectMag(p[0],amK);

   p4[1][0].SetVectMag(p[1],amPi);
   ```

   where `amK` is the mass of K and `amPi` is the mass of the π. `p[0]` and `p[1]` are the three-vector momenta (`TVector3`) of the K and π tracks. The D^0 candidate can be built by summing the above two Lorentz vectors.

   ```
   PP[0] = p4[0][0];

   PP[0] += p4[1][0];
   ```

We can now get access to the D^0 candidate momentum components; `PP[0].X()`, `PP[0].Y()`, `PP[0].Z()`. `PP[0]` is the TLorentzVector of the D^0 particle.

3.7 Cuts

3.7.1 Event-Level Cuts

We selected minimum bias events with conditions for a coincidence triggering of the ZDC detector and for triggering on vertices with z-position $(V_z) < 5\,\text{cm}$ by the mb-vpd trigger. This ensures that the vertex is constrained to be within the acceptance of SVT+SSD.

Events may have several vertices, each with a different position and resolution. Ranks are assigned to the determined vertex positions, based on the likelihood and number of matching extrapolated tracks. We select the highest ranked vertex with `index = 0`. This cut removes events with low multiplicity and may improve vertex resolution. A vertex position cut, $|Vz| < 10\,\text{cm}$ is used to select events that were were reconstructed well and within the region around $V_z = 0$. The cut on V_z helps to select tracks that do not cross a lot of detector support material and are in the heart of SVT acceptance region. Another cut used is on the vertex position resolution, $\sigma_{ZVrtx} < 200\,\mu\text{m}$ along the z-axis. Table 3.2 summarizes the cuts applied at the event level.

Data Set	Cut	Value
AuAu Run-VII	Trigger Id	200001, 200003, 200013
	vertex index (rank)	0 (highest rank)
	$\lvert Z_{Vrtx}\rvert$	< 10 cm
	$\lvert\sigma_{ZVrtx}\rvert$	$< 200\mu$m

Table 3.2: Cuts applied at the event level in Run 7 AuAu data

Figure 3.8 shows the distribution of the vertex position (top row) and the position resolution (bottom row) in the X-Y plane (transverse plane) as we apply the vertex level cuts. The vertex level cuts aid in the cleaning up of the sample and the selection of the best vertices. Figure 3.9 shows the primary vertex position and resolution along the z-axis (beamline) before and after the z-vertex cuts. By limiting to vertices close to (0,0), we choose events within the acceptance of the silicon detectors. Silicon detector information is crucial for the pointing accuracy of the secondary vertex reconstruction.

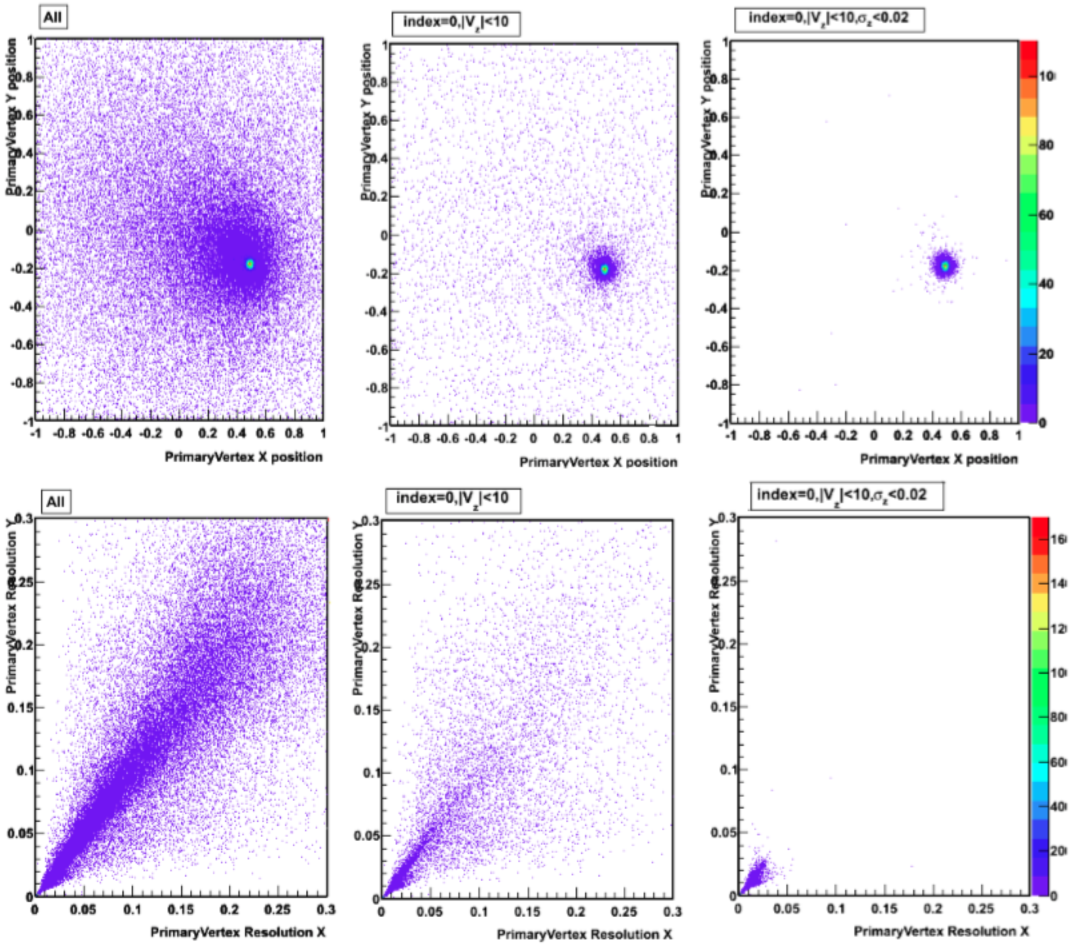

Figure 3.8: Primary vertex position and vertex resolution in the transverse plane

The approximate number of charged particles at mid-rapidity ($|\eta| < 0.5$) per nuclear collision, is called the 'reference multiplicity' in STAR. A cut on reference multiplicity is used later as an offline cut to select different collision centralities. The

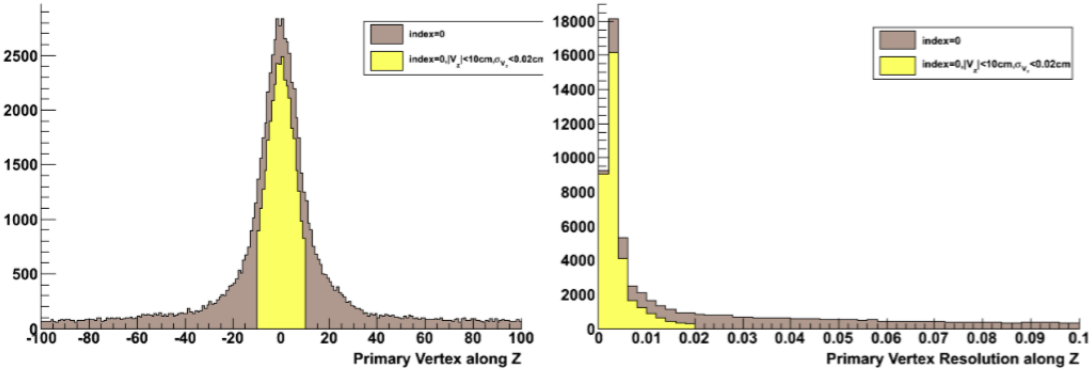

Figure 3.9: Primary vertex position and vertex resolution along the beamline

inclusion of inner tracking for Run 7 Au-Au data required a modification in the calculation of reference multiplicity. The proposed new variable (`gRefMult`) counts global tracks under $|\eta| < 0.5$, $|DCA_{global}| < 3\,\mathrm{cm}$ and Number of Hits Fitted ≥ 10. This is because the reconstruction efficiency seem to depend on the primary vertex position in $|Vz| < 30\,\mathrm{cm}$ region. However, this dependence was generally absent for TPC-only tracking. There was loss of primary tracks for events under SVT/SSD. It was determined that the reconstruction efficiency of `gRefMult` was stable as a function of z-vertex position. A Monte Carlo Glauber simulation (Appendix C) is used to define the centrality of events as given in Table 3.3. We use an offline cut on `gRefMult` to study the charm signal for various centralities.

3.7.2 Track-Level Cuts

A detailed study of cut variables is the most essential part of data analysis, especially for signals in the presence of a large background. This needs to be done for both the signal and the background. The resolution of the reconstructed variables also plays an important role when setting the cut values. The cuts are applied at the

Centrality	gRefMult
$0-5\%$	≥ 485
$0-10\%$	≥ 399
$0-20\%$	≥ 269
$0-30\%$	≥ 178
$0-40\%$	≥ 114
$0-50\%$	≥ 69
$0-60\%$	≥ 39
$0-70\%$	≥ 21
$0-80\%$	≥ 10

Table 3.3: gRefMult and corresponding centrality in Run 7 AuAu data

track level to select $K^{\mp}$ and $\pi^{\pm}$ before they are subjected to the secondary vertexing are discussed below.

Momentum Cut: At low momentum, due to multiple Coulomb scattering (MCS), the resolution of tracks is degraded. These low p tracks are poorly reconstructed. Additionally, there is a very large pion background at low momentum. Therefore, a lower cut on momentum is sometimes necessary. Since $\langle p_T \rangle$ of D^0 is $\sim 1\,\mathrm{GeV/c}$, this may affect the kinematics depending on the cut value. In order to keep the kinematics unaffected while reducing the low p_T background,we tried a cut on the sum of the momentum of the tracks. The cut is $PK + P\pi > 1.5\,\mathrm{GeV/c}$. This removes some uncorrelated tracks without affecting the decay kinematics. The left plot on Fig. 3.8 shows the momentum of tracks and the right plot shows the sum of momentum of track candidates in 2007 Au-Au ProductionMinBias data.

Rapidity and Pseudorapidity: The longitudinal distributions of secondary particles from high energy reactions are usually studied in rapidity (y) or pseudorapidity (η) variables. The rapidity is defined as

$$y = \frac{1}{2} \ln \left(\frac{E + p_z}{E - p_z} \right),$$

where p_z is the parallel component of momentum along the beamline direction. Rapidity is additive under Lorentz transformations: $y' = y + a$, and where y' is the rapidity in the lab frame, y is the rapidity in the CM frame. This means that the shape of the rapidity distribution is invariant under Lorentz transformations (see Appendix B). For ultrarelativistic particles, $\beta \approx 1$ and $E \approx p$, rapidity can be approximated by pseudorapidity,

$$\eta = -ln\left[tan\left(\frac{\theta}{2}\right)\right],$$

where $\theta = p_z/p$. We use a cut on the pseudorapidity of the charged daughter tracks, $\eta < 1.2$, which corresponds to the pseudorapidity coverage of the silicon vertex detectors. A cut on rapidity, $|y| < 0.5$, was applied later when calculating the yield and p_T spectra, so as to avoid another term in the calculation of $d^2N/d_yd_{p_T}$.

Number of TPC hits: The tracks selected are required to satisfy the condition,

$$\frac{nHitsFit}{nHitsPossible} > 0.51.$$

The numerator is the number of TPC hits fitted with a helix approximation and the denominator refers to the TPC hits possible. A track can have a maximum of 45 TPC hits. As the number fitted points increases, the momentum resolution of the track gets better, since more fit points implies a greater track length. The cut on the ratio of fitted points to hit points helps to avoid split tracks, a situation where the reconstruction software takes hits from one track and generates two separate tracks. Figure 3.9 shows this variable from real data.

***dE/dx* TrackLength:** This is the track length in the TPC that is used for the dE/dx calculation. We use a cut of dE/dx track length ¿ 40 cm in our analysis. A lower cut on this variable ensures a better fitting on the track, and also ensures that the tracks reach the TPC.

Silicon (SVT+SSD) Hits: Silicon hit information is an important cut variable used for the pointing resolution of tracks. A requirement on the number of silicon hits (SiHits), as well as the radius of the first hit are crucial for this analysis. These requirements will be discussed in detail in Sec 3.3.5.

Kaon decay angle in the D^0 rest frame: The variable θ^* refers to the angle made by the kaon in the CM frame of the lab D^0. In the CM frame of the D^0, the D^0 is at rest and the daughter particles decay back-to-back. Figure 3.10 shows a schematic of the decay of D0 in the lab frame (left) and in the CM frame (right).

The motivation behind this cut variable is discussed by considering the cases where $cos(\theta^*)$ has a value of $\sim \pm 1$. When $cos(\theta^*)$ is close to -1, the angle θ^* has values near $180°$. This value of θ^* corresponds to a kaon decaying in the opposite direction of the parent D^0. These kaons will be even slower after the 'boost' in the opposite direction. The track reconstruction efficiency has a steep slope at low momenta and therefore these soft kaons are unlikely to be reconstructed well. When $cos(\theta^*)$ is close to $+1$, the angle θ^* has values near 0. Therefore, the kaon is emitted parallel to the parent D^0. Because the kaon and pion decay back-to-back in the CM frame, this results in the production of soft pions.

A cut on $|cos(\theta^*)| < 0.8$ removes the very soft kaon and pion tracks and therefore, is used while running the *mu*vertexing code. Figure 3.11 shows the dependence of kaon decay angle and track momentum for kaons and pions for pure D0 signal events.

Chapter 4

Results and Discussion

4.1 Simulation

Simulation studies play a critical role in determining the effectiveness of an analysis technique. In this section, we discuss the various techniques and tools used to study the effectiveness of our analysis, including GEANT and HIJING. GEANT is a software package used to simulate the passage of particles through matter, and HIJING is a software package used to model multi-jet production in heavy-ion collisions. Included here are resolution studies that were conducted to search for differences between the microvertexing techniques employed.

4.1.1 D^0 Resolution Studies

To evaluate the performance of the three microvertexing techniques, we had to do several resolution studies and quantify the differences or gains. For the studies, we used a sample of one thousand pure D^0 s to compare the microvertexing, global helix reconstruction, dca geometry helix reconstruction, and TCFit. Here we make a direct correlation between the simulated and reconstructed events, and look at the resolution of the secondary vertex reconstruction.

In order to make a one to one comparison between simulated tracks and reconstructed tracks, one must be able to select the matching tracks in both simulation and reconstruction. First, a set of particles are simulated using GEANT. Next, the

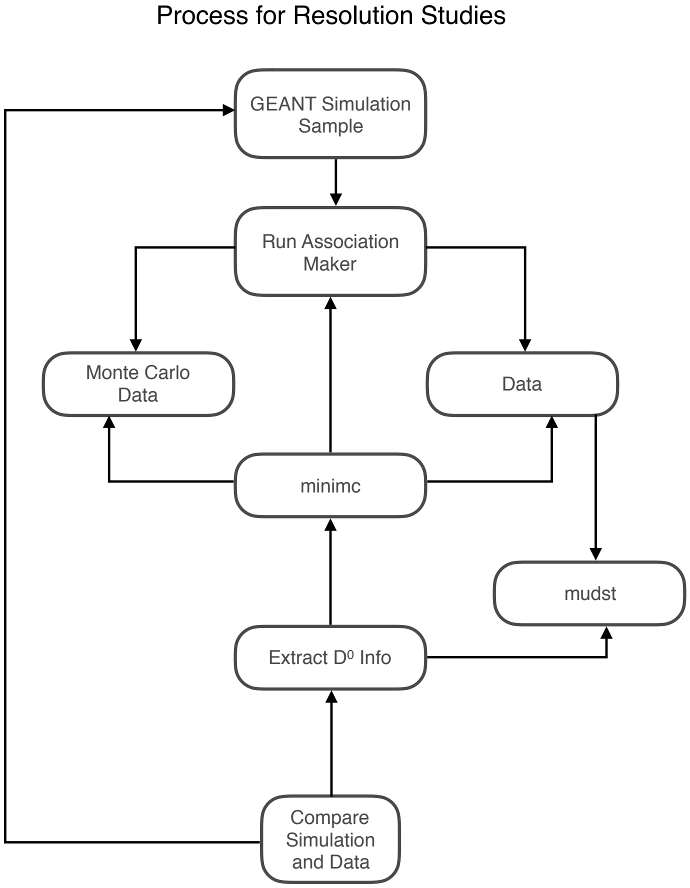

Figure 4.1: Flow Chart for Resolution Studies

simulation data goes through an Association Maker that produces two types of files, Monte Carlo files and data files. The Monte Carlo and data files are then used to find the tracks to compare with the simulation data.

After the particles are simulated in GEANT, the Association Maker associates daughter tracks with their parent tracks and produces two types of files. Monte Carlo, *.minimc.root, files contain a tree with information about various association between all parent tracks and all daughter tracks. Data files, *.mudst.root, contain only information about tracks visible to the STAR detector array.

Contained within the Monte Carlo tree is a branch dedicated to matched pairs. Matched Pairs are a group of tracks that evolve from a single parent. Although pair is in the variable name, a matched pair may contain more than two tracks, because it contains information pertaining to all of the daughters of a particle, all of the granddaughters of the particle and all subsequent generations of the particle. In GEANT, each D^0 decays into a K^- and π^+, therefore every D^0 must have matchedPairs≥ 2.

Also contained in the matched pairs tree is information relating the parent track the daughter tracks. By choosing the GEANT identification of the parent particle and daughter tracks, tracks can be selected that are daughters of that type of particle. The GEANT Id of the D^0, K^-, π^+ are 37, 12, and 8 respectively. Each track in a matched pair also contains information about the specific track from which it originated. By requiring that the key of the parent track be the same for both daughter tracks, it is ensured that both the K^- and π^+ originated from the same D^0.

Since the Monte Carlo files contain information about both charged and neutral tracks, it contains a greater number of tracks per event. To match simulated tracks to reconstructed tracks, one must use the reconstruction key. After a K^-/π^+ pair is shown to originate from the same parent D^0, the reconstruction key can be read out. The reconstruction key provides the information that allows one to choose which reconstructed track corresponds to a simulated track in a given event.

The resolution studies were done using macros that read GEANT information, read Monte Carlo Information, read reconstruction information and compared GEANT information to reconstruction information. The GEANT data is read and used to record information about the properties of the D^0, K^- and π^+ tracks. The Monte Carlo files are used to determine which tracks to look at in the reconstructed data files. A modified version of our microvertexing code is run on the reconstructed data to store data about the reconstructed D^0 vertex and its daughter tracks. Finally a macro is used to make a one to one comparison between the simulated and reconstructed data.

By studying the correlations between simulated and reconstructed data, one can see the effects of reconstruction and look for deficiencies in the microvertexing techniques. If every track is perfectly reconstructed, one would expect a set of perfectly linear plots for the relationship between simulated and reconstructed data. Given the limited resolution of the STAR detector, the resulting plots should appear to have a nearly linear correlation. Any time something different is seen, it must be studied further to find the root cause in the error.

The decay length correlation shows a better correlation as the distance from the primary vertex increases. This is due to the current detector's resolution limits. In the next section, we discuss how we use a sample of particles that decay far from the primary vertex to show that the secondary vertices are being properly reconstructed. The secondary vertex correlation plots show that the TCFit algorithm is better are properly reconstructing the secondary vertices.

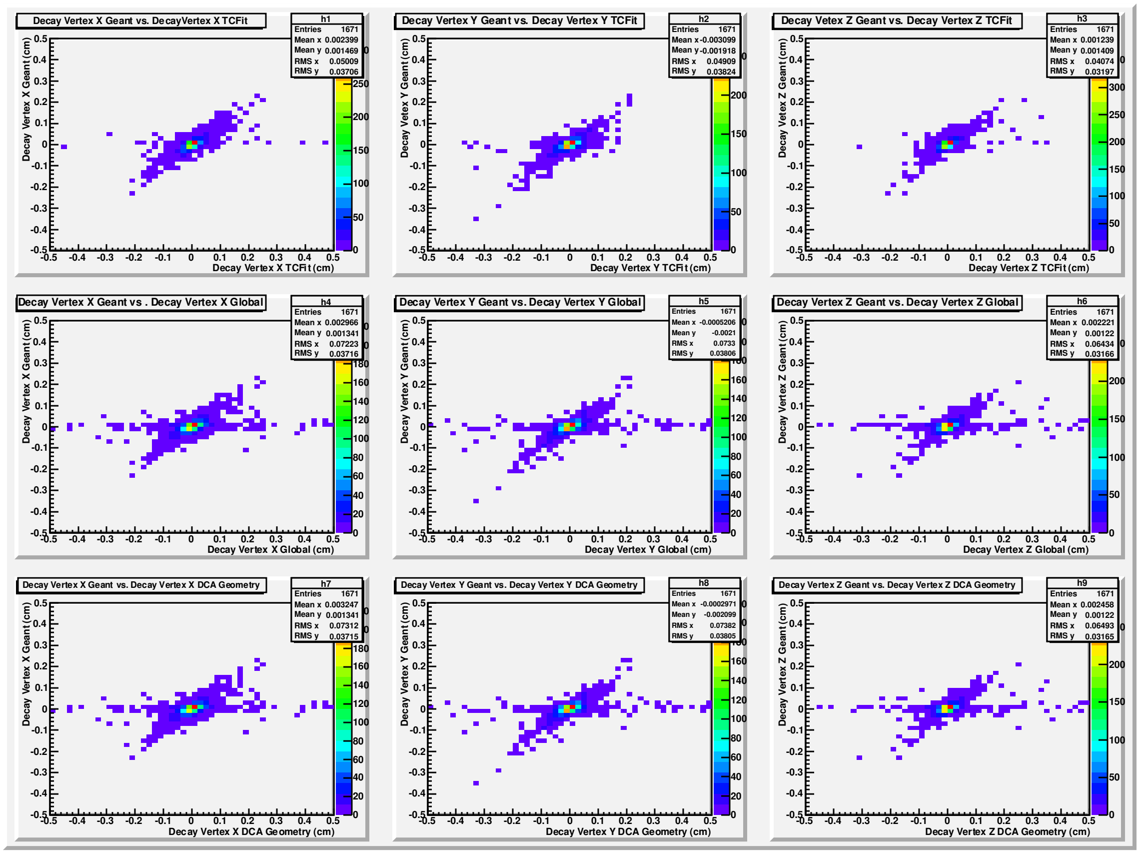

Figure 4.2: TCFit x, y, z are Top Row, Global Helix x, y , z are Middle Row, and DCA Geometry Helix x, y, z are Bottom Row.

Both of the helix swimming techniques suffer from a similar problem in reconstruction. In the case of low-pt D^0 s, where the daughter particles move nearly back to back in the lab frame, the tracks are nearly parallel, resulting in a horizontal band in the x, y, and z coordinate of the decay vertex of the D^0 resolution plots. Another contribution to this band comes from high-pt D^0 s, where the daughter particles move nearly parallel in the lab frame, as shown in Fig. 4.2. Note that the TCFIT technique reduces the horizontal band. Fig. 4.3 shows that by selecting pairs that are nearly antiparallel ($4 > |\Delta\phi| > 2\,\text{rads}$) and plotting them, the contribution of nearly parallel tracks to the secondary vertex reconstruction in the lab frame can be seen for DCA-Geometry and the Helix Swimming methods. Any time a pair of tracks are nearly parallel or antiparallel in the lab frame, the helix swimming techniques do not perform adequately. The swimming technique relies on finding the point where the distance of closest approach (DCA) is minimized. When the tracks are nearly parallel, the region to find the point where the DCA is minimized becomes broad, as the tracks do not move away from one another quickly. This results in the calculation failing to find the true secondary vertex coordinates.

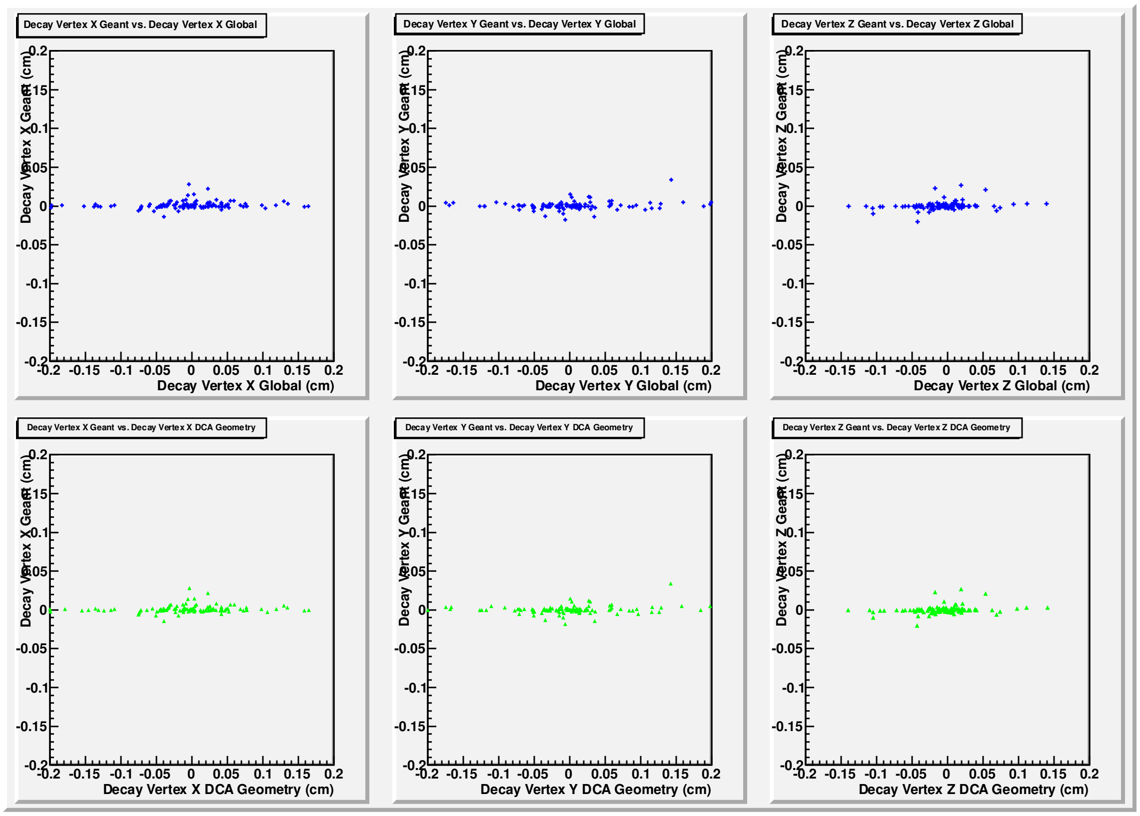

Figure 4.3: $|4 > \Delta\phi > 2\,\text{rads}|$Global Helix data are blue crosses, and DCA Geometry Helix data are green triangles.

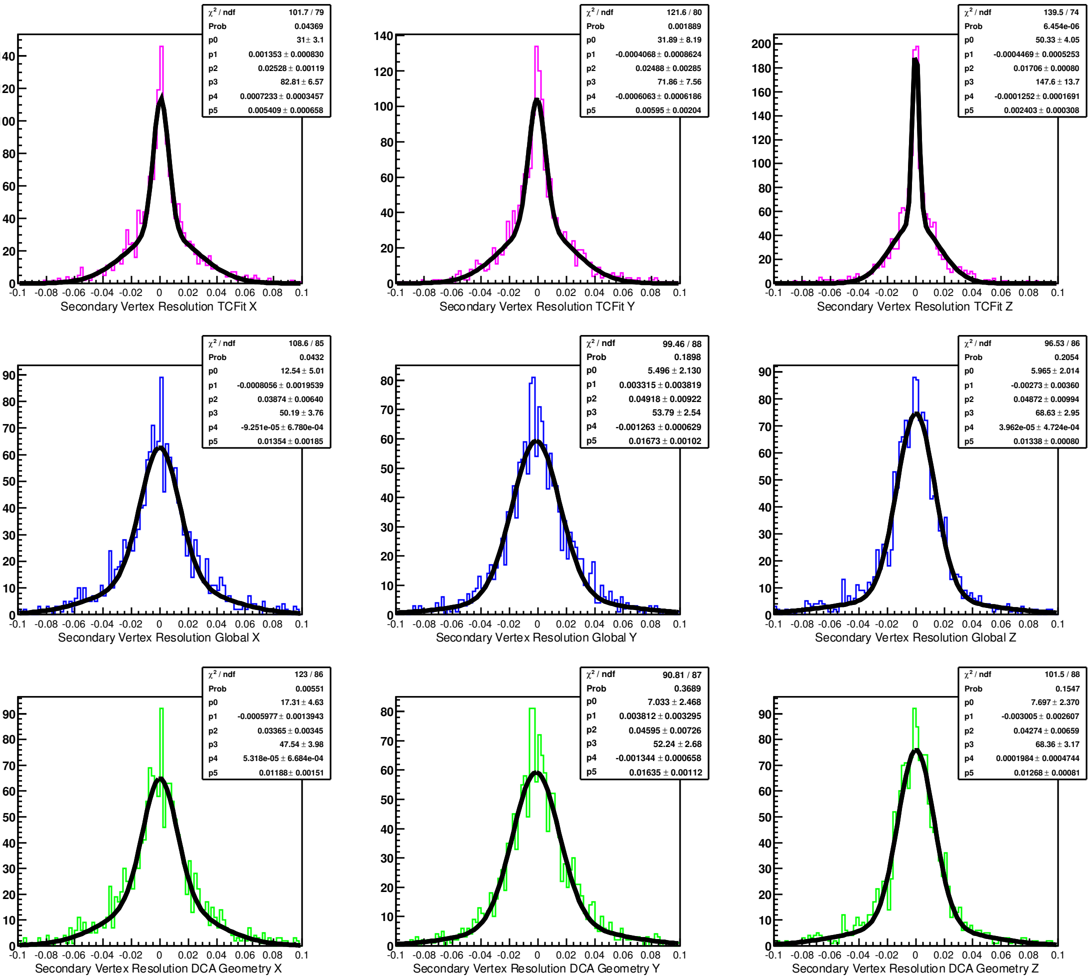

Figure 4.4: Secondary Vertex Resolution for Pure D^0 sample: TCFit data are magenta, Global Helix data are blue, and DCA Geometry Helix data are green.

The resolution of a reconstruction technique can be determined by looking at the differences between simulated and reconstructed data. In the case of the D^0, we looked at the resolution of the secondary vertex coordinates. In every case, the TCFit algorithm outperformed the helix swimming techniques, when looking at the pure D^0 sample, as shown in Fig 4.4. For this reason, the TCFIT method was chosen for use in our final analysis.

A study of the opening angle between the daughter tracks shows that many of the D^0 parents have the daughters decay back-to-back in the lab frame, indicating a decay into two daughters (Fig. 4.5(a)) while the bands corresponding to other decay angles correspond to decays into three or more daughters. Also note that background consisting of tracks that did not come from the same parent in the simulation show that, the opening angle between the tracks in the center of mass frame is rarely back-to-back.

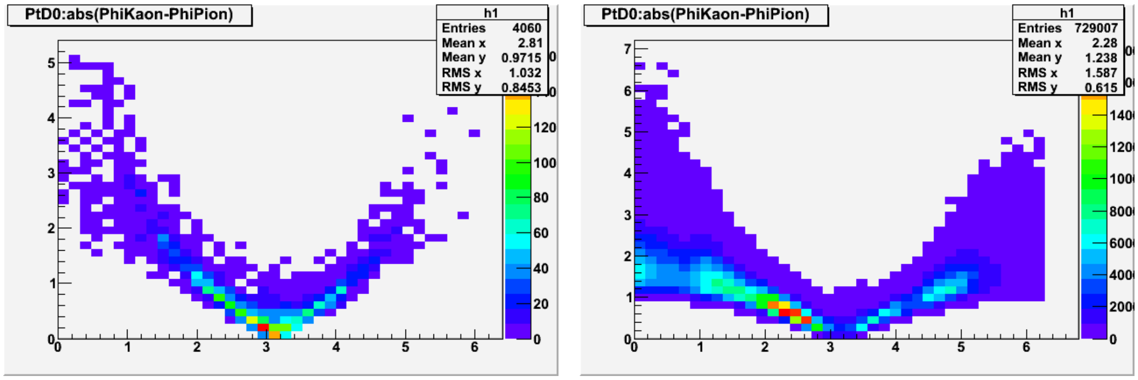

(a)

(b)

Figure 4.5: Panel (a) shows the opening angle of the D^0 daughters in the center of frame while panel (b) shows the opening angle between background in the center of mass frame.

3D DCA plots produced by summing the squares of DCA-XY and DCA-Z. Red is for pure signal, green is for all MuKpi output, and blue is for MuKpi output after pico cuts, Fig. 4.6. The same convention is used throughout. The plots are scaled so that they match nicely on this set of axes. The fact that the plots do not peak at zero is a result of the method. The individual plots, DCA-XY, and DCA-Z are gaussian around zero. The individual 3-D DCA plots are shown next to plots of the 3-D DCA vs. 1/p, Fig. 4.7.

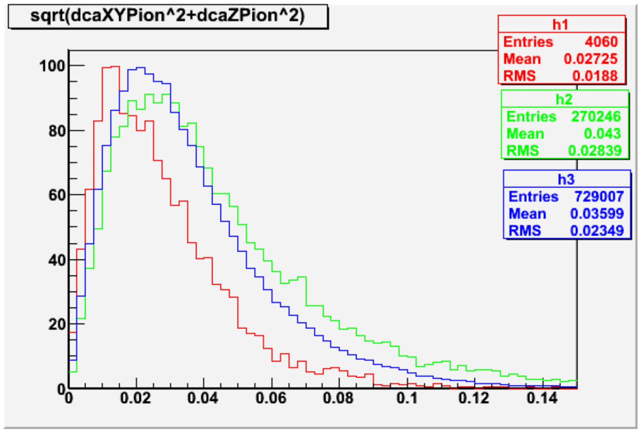

Figure 4.6: Red Line - Pure Signal, Green Line - All Pairs in MuKPi, Blue Line - All Pairs in MuKPi after cuts used in our picodst files

4.1.2 Large $c\tau$ D^0 Resolution Studies

To be certain that the reconstruction techniques are properly reconstructing the D^0 decays, we generated a sample of one thousand pure D^0 s that were modified in GEANT to have decay lengths of a few centimeters rather than tens of microns. This is achieved by modifiying the D^0 s lifetime from 4.15e-12s to 4.15e-10s. The increase by a factor of one hundred in the lifetime results in a similar increase by a factor of 100 in the decay length of the D^0.

The large $c\tau$ sample shows that the TCFit algorithm reconstructs the secondary vertex better than both helix swimming techniques. Both helix swimming techniques

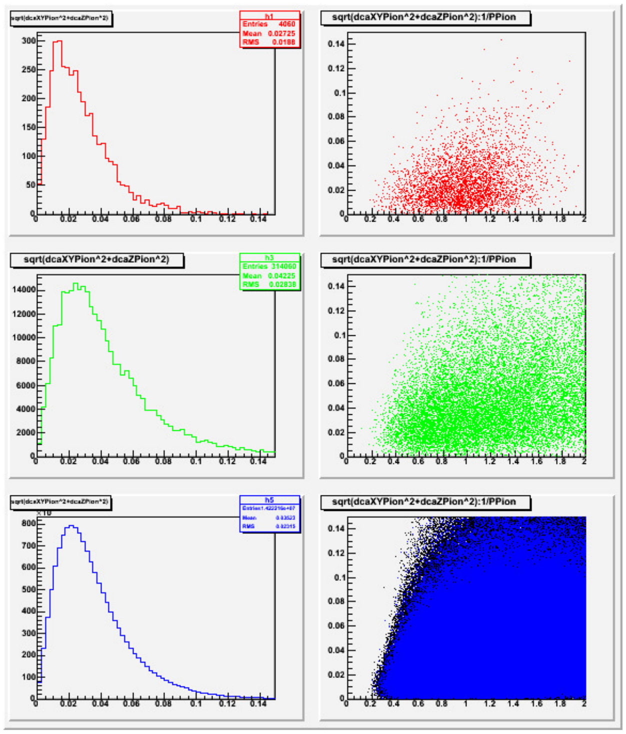

Figure 4.7: Opening angle of background in center of mass frame.

still show evidence of horizontal bands caused by nearly parallel tracks with a short decay length.

Because TCFit only returns a decay length, rather than individual coordinates, the unit vector for the reconstructed momentum of the D^0 is used to resolve the spatial coordinates of the secondary vertex.

4.2 Toolkit for Multivariate Analysis(TMVA)

During analysis, a group of cuts must be chosen to reduce background without artificially enhancing the signal in a dataset. Traditionally this has been done by taking a dataset and cutting each variable independently, and checking to see how each cut affected the signal to background ratio in both real data and simulated pure signal mixed into pure background events. Each parameter would be addressed individually, and often with simple linear cuts on the data.

When searching for weak/rare signals, it is essential to extract the maximum available signal from the data. Traditional techniques can quickly remove a significant portion of the signal and greatly increase the number of events required to make a measurement. In this dissertation, we utilize the Toolkit for MultiVariate Analysis, a ROOT integrated machine learning environment for the processing and parallel evaluation of multivariate classification and regression techniques. Advanced discrimination methods using all the information for optimal background reduction such as correlation of the input variables in signal and background are available in TMVA. A multivariate selection may allow us to have a higher signal efficiency for the same background rejection when compared to a cut-based selection. TMVA uses various classifiers, some of which we will discuss in greater detail later, to discriminate signal from background and it provides a framework for training, testing and performance evaluation of a variety of classification methods [10]. The classification methods include but are not limited to: rectangular cut optimization, projective likelihood estimation (PDE approach), linear discriminant analysis (H-matrix, Fisher and linear (LD) discriminants) to more complex nonlinear approximations such as boosted/bagged decision trees (BDT), Multi-Layer Perception (MLP), and others. The TMVA analysis proceeds in two phases, first, the training phase, and second, the application phase.

4.2.1 TMVA Training

During the training phase, two samples must be provided to the TMVA software, one containing pure signal, and the other containing pure background. For the analyses presented here, the training samples consisted of pure D^0 simulated with a power law p_T distribution for the pure signal sample and the background sample consisted of HIJING Au+Au central events. Each data set was processed with our microvertexing macro with the resulting output tree structure provided as input to TMVA for the training samples. When working with machine learning techniques, overtraining becomes a cause for concern. Overtraining occurs when too many model parameters are tuned using too few data points, creating a bias that will affect classification in testing and during the application phase. In order to account for this, TMVA splits both the signal and background data sets in half, separating them into two groups that are used for training purposes and testing purposes, respectively.

We tried several different classifiers including, Fisher, BDT and MLP classifiers for training. The classifier output gives a unique value to each $K\pi$ pair. Cutting on this classifier value is equivalent to cutting on multiple variables at the same time. Therefore, using such a cut should increase the purity and decrease the background. During the training phase, weight files are created, which contain the normalized distributions of signal and background training samples and the correlation of the variables. After the training phase a testing sample is provided to evaluate the performance of the classifier.

After TMVA performs an analysis of the test sample a number of plots and files are produced including, a set of plots displaying signal and background distributions for the variables included in the analysis (Fig. 4.8), a set of MVA output distributions for each classifier, a Receiver Operating Characteristic (ROC) diagram (Fig. 4.9) displaying the effectiveness of each classifier, and a set of weighting files that are used internally by TMVA. The MVA distributions provide a value unique to the classifier that can be cut on to improve the signal to noise ratio. The ROC diagram displays the signal efficiency versus background rejection for each classifier used. In general, the greater the area under the ROC curve, the better the classifier is for analysis.

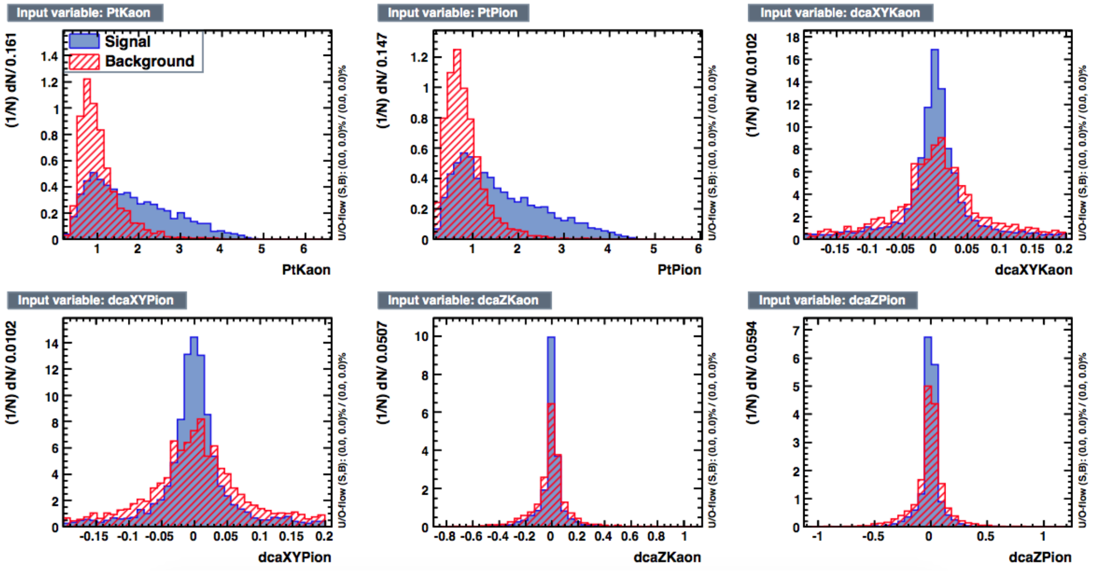
Input variable: PtKaon

Input variable: PtPion

Input variable: dcaXYKaon

Input variable: dcaXYPion

Input variable: dcaZKaon

Input variable: dcaZPion

Figure 4.8: Example of signal and background variable distributions from TMVA.

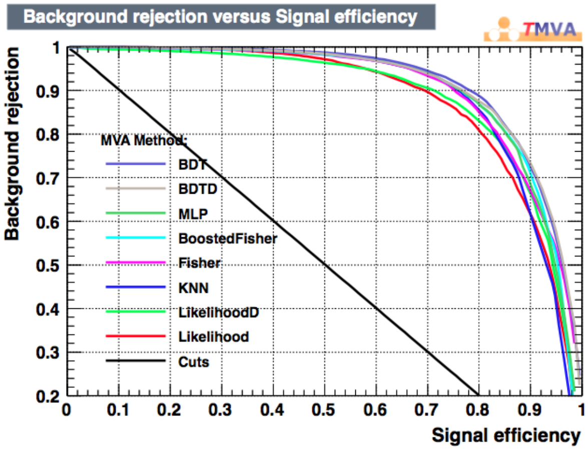

Figure 4.9: Background rejection vs. signal efficiency for the MVA tested using the variables from Fig. 4.8.

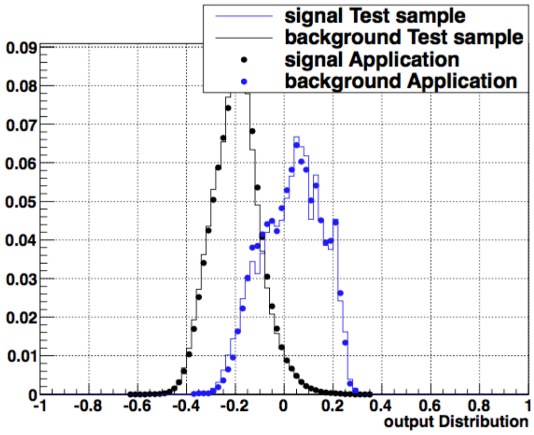

Figure 4.10: MVA output distribution for the BDTD classifier from the test sample (lines). Points are from the test events used during training.

4.3 TMVA Application

4.3.1 Simulation

Once TMVA is trained using pure signal and pure background samples, it is ready to be used in the application phase. The sample used in this discussion consists of 50k minimum bias Au+Au collisions embedded with Monte Carlo D^0 particles forced to decay via the $D^0 \rightarrow K^- + \pi^+$ hadronic decay channel. The D^0 particles were generated with flat transverse momentum ($0 < p_T < 5\acute{G}$eV/c), and represent 5% of the event multiplicity. This sample was analyzed with the same set of cuts used with real data, and resulted in a signal of $\approx$ 7k (kπ) pairs that were matched with the Monte Carlo sample, as well as $\approx$ 49k (Kπ) pairs with the same sign in the background sample. TMVA was trained using the transverse momentum of the daughter tracks, the transverse DCA of daughter tracks to the PV and their errors, the longitudinal DCA of daughter tracks to the PV, the transverse and longitudinal DCA between daughter tracks and the secondary vertex, the signed decay length of the (Kπ) pair to the primary vertex and its error, and the probability of fit to the found secondary vertex. Because the transverse momentum of the D^0 in this sample was flat, we did not use this variable in the training to prevent biasing the results of the training phase. Instead, the transverse momenta of the daughter particles were used, as they are less sensitive to the flatness. The resulting ROC curves for the training of this sample are presented in 4.9. Note that all of the classifiers tried provide, roughly, equivalent background rejection, except for the Cuts classifier.

Based on the separation between the signal and background distributions shown in Fig. 4.10, a cut of mvaBDT > 0.15 was selected to have a high signal to background ratio, resulting in a significant peak around the D^0 mass in the Kπ region, as shown

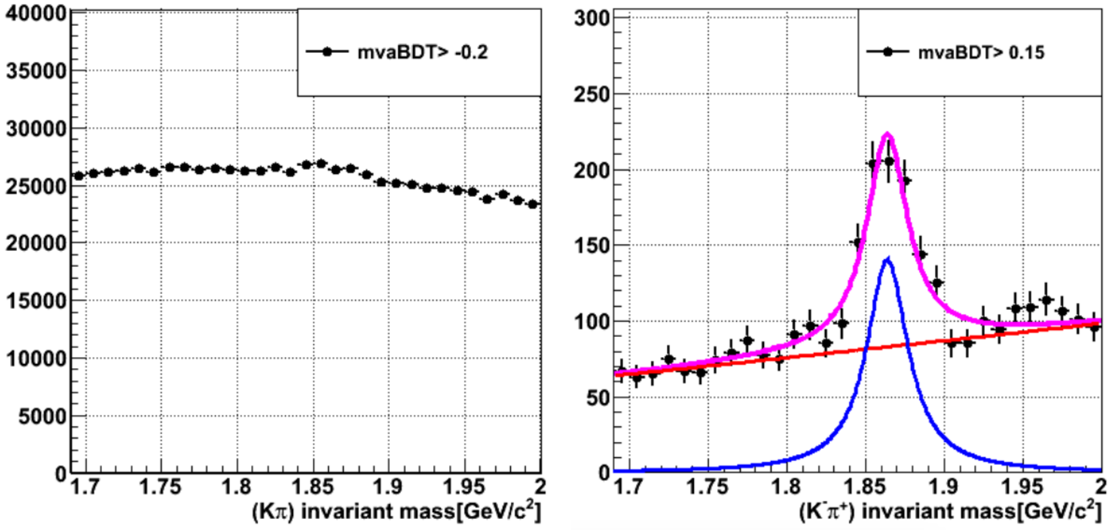

(a) (b)

Figure 4.11: Invariant mass distribution for a poor choice (left) of BDT cut, mvaBDT $>$ -0.2, and the invariant mass distribution for a much better choice (right) of BDT cut, mvaBDT $>$ 0.15.

in right panel of Fig. 4.11. Note that a poor selection of the mvaBDT > -0.2, results in an invariant mass distribution that has no significant peak in the D^0 mass region, as shown in the left panel of Fig. 4.11, demonstrating the effectiveness of the use of TMVA in data analysis.

4.3.2 Real Data

The effectiveness of our use of the TMVA application was demonstrated by the ability of the software to reduce the background in our search for direct topologically reconstructed D^0 particles in the STAR experiment. However, when applied to the real data, approximately 35 million events, alongside a like-sign background subtraction a statistically significant invariant mass peak could not be found, as shown in Fig. 4.12. The result of the efforts in this analysis is a null result for analyses

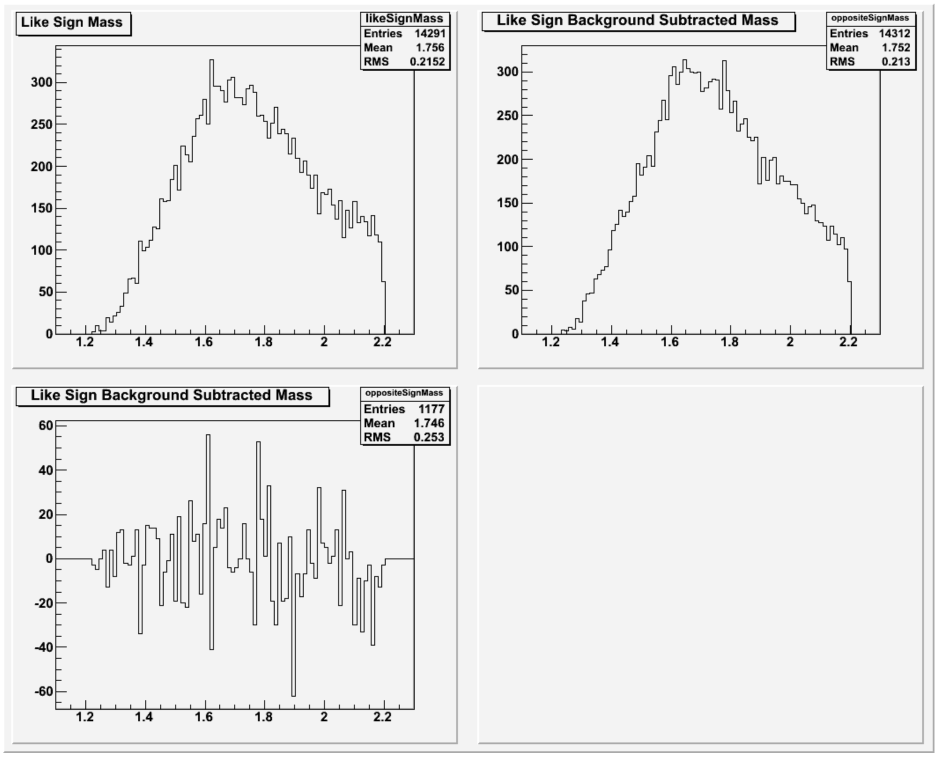

Figure 4.12: Invariant Mass distribution(Lower Left) after subtracting like sign background in real data.

conducted on SVT-era data sets. The techniques developed over the course of this research have proven successful when applied to datasets from HFT-era data sets. Some results of those analyses are presented in the next section.

4.4 Charm results using the HFT

As we discussed earlier, our attempt to use the SVT/SSD on a (useful) 2007 data sample of about 25 – 30 Million Au+Au events at 200 GeV to extract a D^0 sample for physics analysis was not successful. The first significant signal of fully topologically reconstructed D^0s was obtained during the RHIC run of 2014 (and 2016) with the next generation of vertex detector, the HFT. Table 4.1 summarizes the remarkable differences between the two setups, i.e. the factor of 50 in event statistics, the fraction of detector being alive during the run, and the factor of 10 in track pointing resolution due to differences in detector thickness and distance of first layer from the beam line (lever arm). We believe that even if we had the HFT, instead of SVT, installed and fully operational in Run-2007, the data sample (35 Million events) sample would not have been large enough to obtain significant physics results, but only a small bump in the D^0 mass spectrum. We need to reiterate at this point that our work and lessons learned with the SVT were the foundation that the HFT design, software and analysis was built upon.

In the following paragraphs we show selected HFT results [68] obtained from studying roughly 700 million MinBias events of the processed dataset obtained during Run 2014 together with a brief discussion related to the physics impact of the measurements on our understanding of the QGP production at RHIC energies.

The HFT was built with two specific measurements as its physics goals; one is the determination of the nuclear modification factor (R_{AA}) for charm (and maybe

Parameter	SVT/Run2007	HFT/Run2014
Data Sample (Million events)	25-30	1200
Track Pointing Resolution (1 GeV/c) (microns)	280	30
Distance of inner layer from beam axis (cm)	6.5	2.5
First layer's radiation thickness ($\% X_0$)	2	0.4
Fraction of detector dead areas (%)	20	< 5
D^0 Signal Significance in data sample	≈ 0	≈ 200

Table 4.1: Comparison of SVT and HFT parameters

bottom) quark and the other the measurement of charm elliptic flow (v_2) as a function of collision centrality and p_T. The aim was to perform both measurements using unambiguous, fully reconstructed, charm meson decays as well as achieve precision measurements at lower p_T values.

The R_{AA} at higher p_T ($> 4 - 5$ GeV/c) can be used, together with light quark measurements, to precisely determine the "energy loss per unit length" parameter($\hat{q}$) for each quark species as a function of energy (given the corresponding LHC measurements). At lower p_T values, together with the elliptic flow, it can be used to determine the charm "diffusion coefficient" in hot partonic matter. The elliptic flow (v_2) magnitude and p_T dependence is important in order to determine if charm exhibits any flow and if so compare it with that of lighter species. Flow is developed at the very early stages of the collision and if charm shows significant flow, i.e. comparable to that of lighter quarks, that would mean that the system must be in equilibrium, i.e. be fully thermalized. This is because for the heavy charm quark to acquire the velocity of the rest of the partonic fluid it needs to be in thermal equilibrium with the lighter quarks, or interact many times. This randomization of the kinetic energy is the very definition of thermalization, an important condition for the hot partonic matter to be a 'state' of nuclear matter.

Figure 4.13 shows the measured D^0 (invariant yield) spectrum [69]. The blue points are the HFT Au+Au 200 GeV data from the Run-2014 analysis. The open-red circles are STAR's published Au+Au 200 GeV data based on a TPC-only analysis of data taken during the 2010/2011 runs [70]. The blue, HFT points start at p_T values above 2 GeV since the lower p_T values are not yet corrected for all systematic effects, but in principal the HFT points can cover the full range down to $p_T = 0$ value. The same figure shows (filled-black circles) STAR's p-p 200 GeV data together with a (dashed-blue line) fit using the Levy function which is found to best describe the data. The Au+Au points are for the 0-10% centrality bin and they have been scaled down by a factor of 20 in order to fit in the figure. The blue-dashed line near the Au+Au points is the Levy function p-p fit scaled by the number of binary collisions in central Au+Au events. If the Au+Au data is nothing but a mere superposition of elementary p-p collisions, i.e. nuclear effects are absent, then the line should go through the data points. We see that at higher p_T values the scaled p-p data is significantly higher than the measured Au+Au data (note the logarithmic vertical scale). In order to study this better we form the ratio of Au+Au to scaled p-p which is nothing else but the nuclear modification factor R_{AA} and it is discussed next.

Figure 4.14 shows the measured D^0 nuclear modification factor (R_{AA}) as a function of p_T for Au+Au 200 GeV central (0-10%) collisions [69]. Black points are with the HFT and the red points are from the TPC analysis [70]. Also shown for comparison

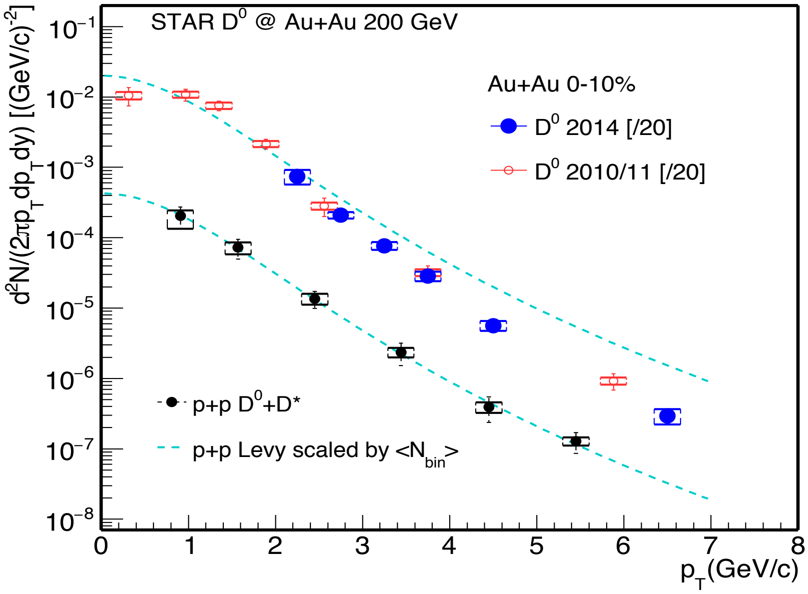

Figure 4.13: Invariant yields of D^0 mesons in Au+Au 200 GeV collisions (red and blue points) and p-p 200 GeV interactions (black points). The Au+Au points are for the 0-10% centrality bin and they have been scaled down by a factor of 20 in order to fit in the figure. The lower dashed-blue line is a Levy function fit to p-p data and the upper one is the lower one scaled up by the number of binary collisions in Au+Au. The caps show the estimated systematic error for each point.

(open blue points) is the R$_{AA}$ factor for light hadrons (mostly pions) as measured in STAR for 0-12% central Au+Au 200 GeV collisions [72]. The caps show the estimated systematic error for each point and the grey band in 2014 points is an extra uncertainty due to p-p reference data.

The R$_{AA}$ shows a strong suppression at high p$_T$ ($> 3-4\,$GeV) indicating strong charm medium interactions at this kinematic region. At the intermediate p$_T$ range (0.7-2 GeV/c), the TPC data shows an enhancement. It would be interesting to see whether the HFT points corroborate this behavior at low p$_T$ values. The enhancement can be described by theoretical models that incorporate coalescence of charm and light quarks (see below).

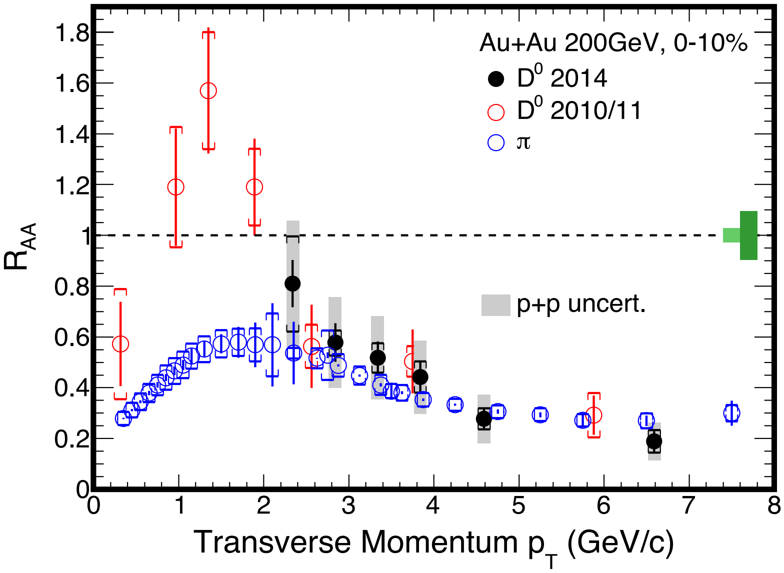

Figure 4.14: The D^0 nuclear modification factor with (black) or without (red) the HFT as a function of p_T for Au+Au 200 GeV central (0-10%) collisions. Also shown for comparison (open blue points) is the same factor for light hadrons (mostly pions). The caps show the estimated systematic error for each point and the grey band in 2014 points is an extra uncertainty due to p-p data.

Figure 4.15 shows the measured D^0 elliptic flow (v_2) in four centrality classes (0-10%, 10-40%, 40-80% plus the full 0-80% range) for Au+Au collisions at 200 GeV. An immediate observation that can be made from these results is the fact that the D^0 elliptic flow is finite in all four centrality bins. This result was corroborated by measurements of v_2 obtained for a different D-meson species, the $D^{\pm}$. The obtained results show identical elliptic flow for both species; this is what one expects from species with very similar masses ($D^{\pm} - D^0 = 4.77 \pm 0.08$ MeV/c^2 [73]) and quark content [68].

Figure 4.16 show the comparison between D^0 v_2 and other particle species measured at 200 GeV [74, 76] versus p_{T} in two different centrality classes, 0-10% (top-left)

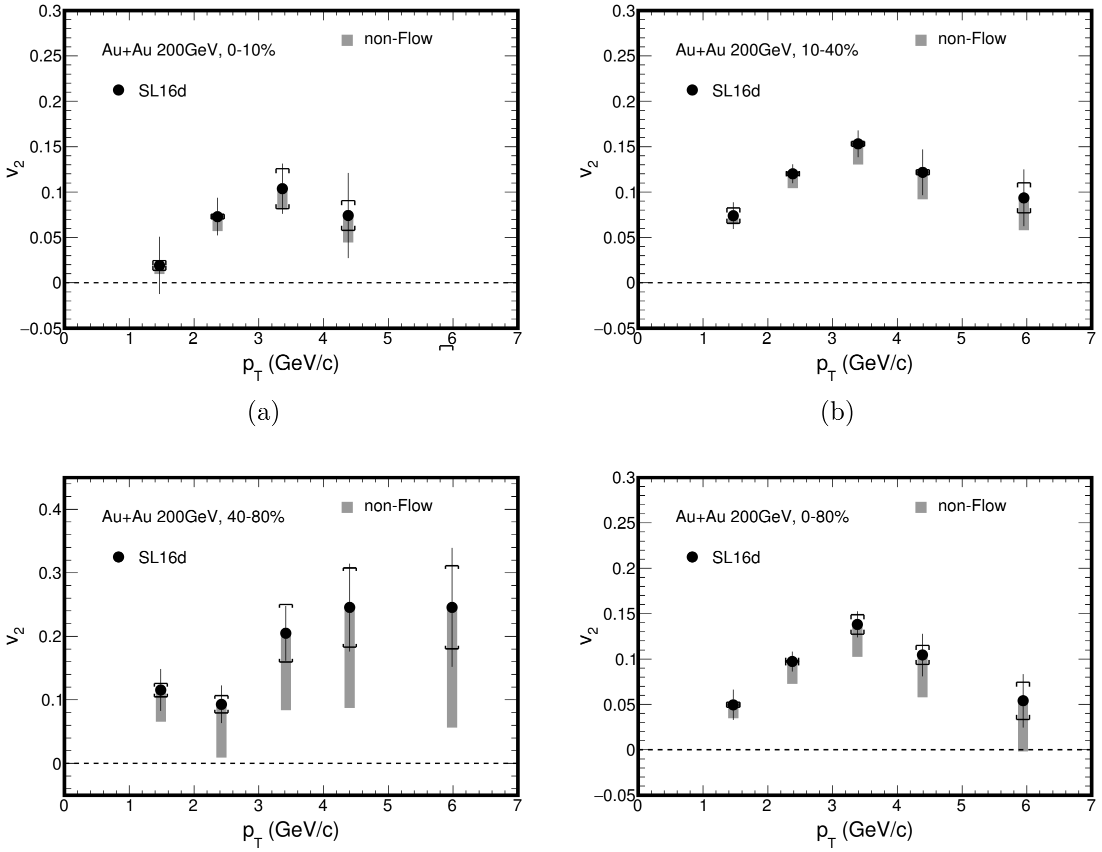

(a) (b)

(c) (d)

Figure 4.15: D^0 v_2 measured in 0-10%, 10-40%, 40-80% and 0-80% central events. The caps show the estimated systematic errors for each point and the shaded area the estimated contributions from non-flow related sources. Details can be found in Ref [68].

and 10-40% (bottom-left). Furthermore, in order to account for the different particle masses and Number of Constituent Quarks (NCQ), the comparison is done(right column) by plotting the NCQ-scaled flow v_2/NCQ vs the NCQ-scaled and rest mass subtracted transverse mass $(m_T - m_0)$/NCQ where $m_T = \sqrt{p_T^2 - m_0^2}$. This way one can put on equal footing particles with 2 or 3 valence quarks and also different quark species. For the most central events, figure 4.16 (right column), we can see that all of the particle species, including D^0, follow the same trend. This is a strong indication that charm quarks are flowing with a thermalized medium where the partons are the only relevant degrees of freedom.

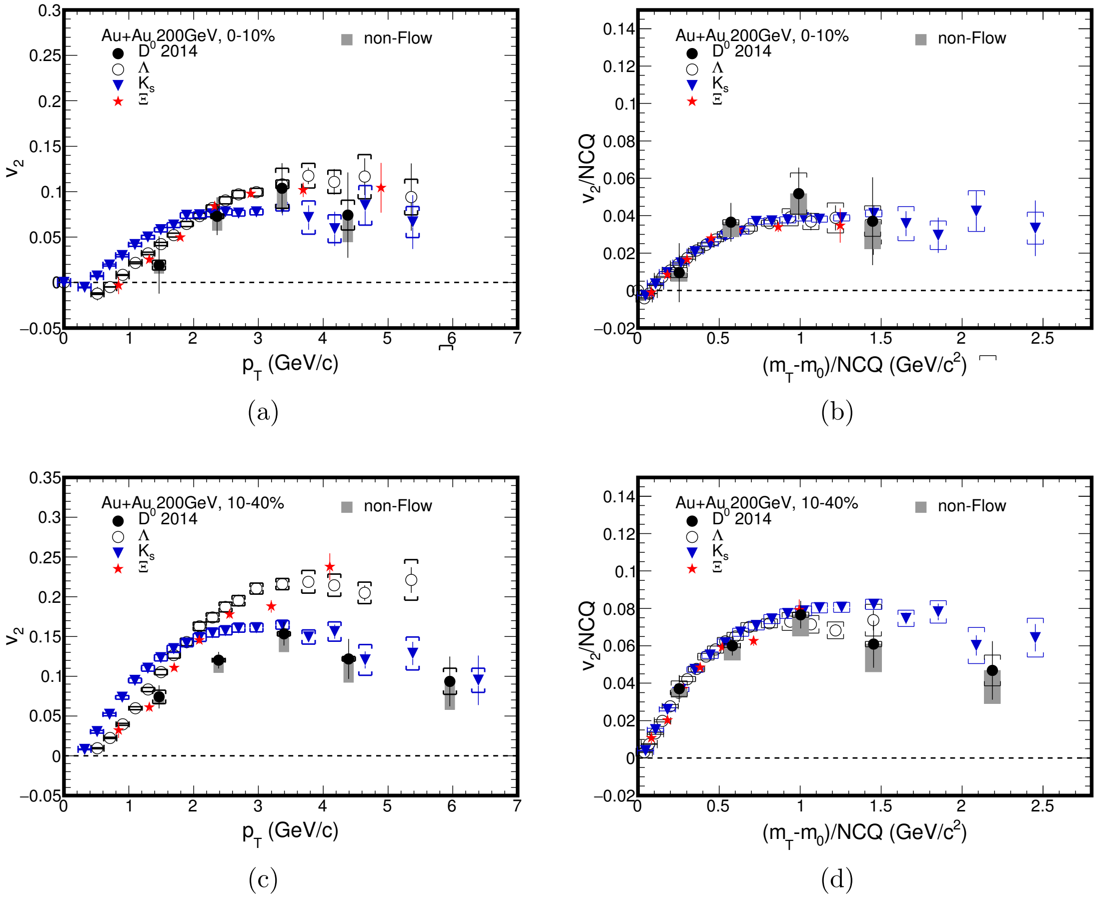

(a) (b)

(c) (d)

Figure 4.16: v_2 vs p_{T} (left) and v_2/NCQ vs $(m_T - m_0)$/NCQ (right) for D^0 compared to other particle species [74] in 0-10% (upper) and 10-40% (lower) central events with m_0 the mass of the particle and $m_T = \sqrt{p_T^2 + m_0^2}$.

One of the main motivations for measuring the charm quark flow is to constrain models that calculate the properties of the QGP medium, for instance the transport properties discussed earlier in this section. Figure 4.17 shows the comparison to the different models introduced in [68].

Two calculations from the TAMU model are included in this comparison, the blue line assuming charm quark diffusion in the medium agrees well with the data while the second calculation without charm diffusion, in magenta, underestimates the measured v_2 at mid p_{T} further supporting the conclusions that charm quarks are experiencing frequent interactions and flowing with the medium. The results from the SUBATECH model can also qualitatively describe the data in the studied p_T range. However, the calculation seems to under-predict the magnitude of the observed v_2 in the range $3 < p_{\mathrm{T}} < 4$ GeV/c. The hydrodynamic model presented here has been tuned to describe the v_2 measured for light quarks and describes the data well in the range where the calculations are provided, strengthening the conclusion that charm quarks are fully thermalized with the medium. Finally, the DUKE model shown here has been tuned to describe the measured R_{AA} at LHC energies with a fixed value for the dimensionless diffusion coefficient $(2\pi T D_s) = 7$ and underestimate the magnitude of the observed v_2.

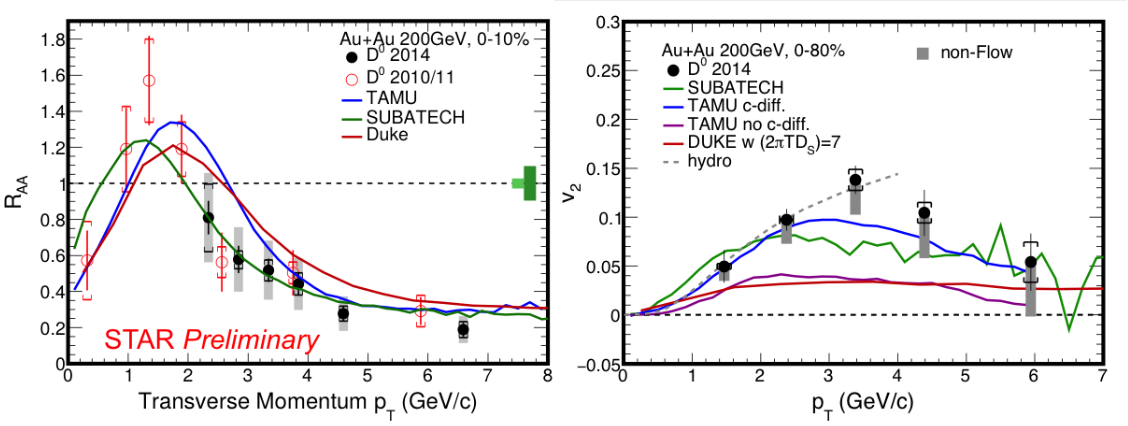

Figure 4.17: R$_{AA}$ (left) and v_2 vs p_{T} (right) for D^0 in 0-10% and 0-80% central events respectively compared to different model calculations.

The values of the diffusion coefficient extracted from a series of model calculations are shown in figure 4.18 together with the range of values that are compatible with the measured results as shown in 4.17. It is interesting to note that the values obtained from lattice calculations [77, 78] are consistent, albeit with large uncertainties, with those obtained from other models shown here and the range inferred from STAR data. However more work will be needed from theory in order to differentiate between the scenarios and further constrain the transport properties of the QGP.

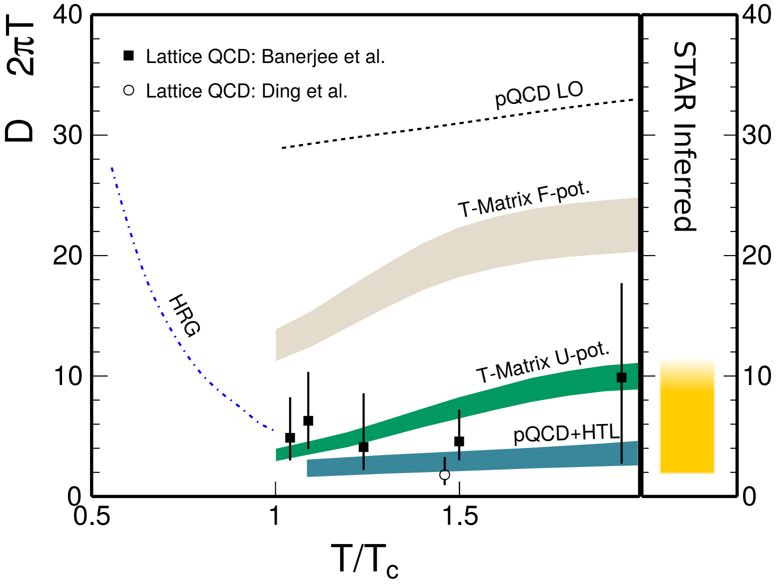

Figure 4.18: Diffusion coefficient extracted from a series of model calculations together with the inferred range of compatible values obtained from the comparisons done to the measured result.

Appendix A

Kinematics of the D^0 Meson Decay

A.1 Definitions

Transverse momentum(p_T): Transverse momentum component is defined as $p_T = \sqrt{p_x + p_y}$. The p_T is a Lorentz invariant variable since both p_x and p_y are uncharged under a Lorentz boost along z-axis.

Rapidity [y]/Pseudo-rapidity[η]: Rapidity is some sort of a relativistic "velocity". It is defined as

$$y = \frac{1}{2} ln \left(\frac{E + p_z}{E - p_z} \right)$$

Where $E = \sqrt{p^2 + m_0^2}$ is the particle's total energy and $p_z = p \cos\theta$ the momentum's z-component, where the z-direction is the beam axis (and thus θ is the polar angle). In the limit where the particle is traveling near the speed of light where $p \gg m_0$ or for massless particles (like the photon), rapidity is reduced to

$$y \approx \frac{1}{2} ln \left(\frac{p + p_z}{p - p_z} \right) = \frac{1}{2} ln \left(\frac{1 + \cos\theta}{1 - \cos\theta} \right) = -ln \tan \left(\frac{\theta}{2} \right) \equiv \eta$$

where η is the pseudo-rapidity and it directly relates to the particle's emission polar angle.

Rapidity is a Lorentz additive quantity so rapidity intervals are Lorentz invariant quantities and therefore the shape of a rapidity distribution of a physics quantity stays the same in all reference systems. The value of rapidity is zero for a particle emitted normal to the beam axis ($p_z = 0$) and achieves its maximum value for beam particles. For a proton of energy of 200 GeV the beam rapidity is about 5.5????

DCA: Distance of Closest Approach is the point where the track helix is closest to a space point, in our case the event or secondary vertex. Since all primary tracks should come from the event vertex, the distribution of this parameter characterizes the instrument's pointing or discrimination ability (resolution) between primary and secondary tracks.

MCS: Multiple Coulomb Scattering. The interaction of charged particles with atomic nuclei as they traverse detector material. The result is the deflection of the particle from its original path by a small angle. The smaller the amount of material traversed the smaller the cumulative deflection.

Luminosity: The luminosity is the flux of beam particles, i.e. the number of particle crossings per unit area per unit time and is equivalent to

$$L = f\frac{N_1 N_2}{A}$$

where f is the frequency of bunch crossing, N_1 and N_2 are the number of particles in each intersecting bunch, and A is the transverse area of the interaction region.

The Gaussian or Normal Distribution: The Gaussian distribution plays a central role in all of statistics and is continuous, symmetric distribution whose density is given by

$$P(x) = \frac{1}{\sigma\sqrt{2\pi}} exp\left(\frac{-(x-\mu)^2}{2\sigma^2}\right)$$

where μ is the mean and σ^2 is the variance of the distribution.

References

[1] S. Bethke. *Experimental Tests of Asymptotic Freedom*, Prog. Part. Nucl. Phys. **58**, 351, (2007).

[2] J. Adams, et al. *Experimental and Theoretical Challenges in the Search for the Quark Gluon Plasma: The STAR Collaboration's Critical Assessment of the Evidence from RHIC Collisions*, Nucl. Phys. A **757**, 102, (2005).

[3] J. Kogut, *The lattice gauge theory approach to quantum chromodynamics*, Rev. Mod. Phys. **55**, 775, (1983).

[4] F. Karsch, *Lattice QCD at High Temperature and Density*, Lect. Notes Phys. **583**, 209, (2002).

[5] K. Yagi, T. Hatsuda and Y. Miake, *Quark-Gluon plasma: from big bang to little bang*, Cambridge University Press (2005).

[6] C. Y. Wong. *Introduction to High Energy Heavy-Ion Collisions.* World Scientific, (1994).

[7] B. Muller *The Limits of Ordianry Matter* Science Magazine **332**(**6037**), 1513 (2011)

[8] Yu.L. Dokshitzer and D.E. Kharzeev Heavy-quark calorimetry of QCD matter Phys. Lett. B **519**, 199 (2001)

[9] C. Adler et al. *Disappearance of back-to-back high p_T hadron correlations in central Au+Au Collisions at* $\sqrt{S_{NN}} = 230\,GeV$ Phys. Rev. Lett. **90**, 202301 (2003).

[10] A. Hoecker et al. *TMVA - Toolkit for Multivariate Data Analysis* Proceedings of Science PoS ACAT **040**, (2007)

[11] A. Adare et al. *Energy Loss and Flow of Heavy Quarks in Au+Au Collisions at* $\sqrt{S_{NN}} = 200\,GeV$ Phys. Rev. Lett. **98**, 172301 (2007)

[12] O. Kaczmarek et al. Heavy Quark Potentials in Quenched QCD at High Temperature Phys. Rev. D **62**, 034021 (2000)

[13] C. Adler et al. (STAR Collaboration) *Centrality dependence of high p_T hadron suppression in Au+Au collisions at* $\sqrt{S_{NN}} = 130\,GeV$ Phys. Rev. Lett. **89**, 202301, (2002)

[14] M. Gyulassy and L. McLerran *New Forms of QCD Matter Discovered at RHIC* Nucl. Phys. A **750**, 30 (2005)

[15] F. Karsch, E. Laermann, and A. Peikert *The Pressure in 2, 2+1 and 3 Flavour QCD* Phys. Lett. B **478**, 447 (2000)

[16] X. Dong *Open Charm Production at RHIC* Acta Physica Poloncia B Proceedings Supplement (2008).

[17] M. Djordjevic, M. Gyulassy and S. Wicks *Open Charm and Beauty at Ultrarelativistic Heavy Ion Colliders* Phys. Rev. Lett. **94**, 112301 (2005)

[18] Z. Lin and M. Gyulassy Open charm as a probe of preequilibrium dynamics in nuclear collisions Phys. Rev. C **51**, 2177 (1995)

[19] Peter Steinberg *Hotter, Smaller, Denser, Faster... and Nearly-Perfect: What's the matter with RHIC?* 2007 J. Phys.: Conf. Ser. **69**, 012032 (2006)

[20] Ulrich W. Heinz *Thermalization at RHIC* AIP Conf. Proc. **739**, 163 (2005)

[21] J. Adams et al. (STAR Collaboration) *Evidence from d+Au measurements for final-state suppression of high p_T hadrons in Au+Au collisions at RHIC* Phys Rev. Lett. **91**, 072304 (2003)

[22] T. Matsui and H. Satz *J/ψ Suppression by Quark-Gluon Plasma Formation* Phs. Lett. B **178**, 416 (1986)

[23] J. Schaffner-Bielich *What is so special about strangeness in hot matter?* J. Phys. G **30R**, 245 (2004)

[24] D.A. Appel *Jets as a probe of quark-gluon plasmas* Phys. Rev. D **33**, 717-722 (1986)

[25] M. Hahn et al. *The RHIC Design Overview* Nucl. Instrum. Meth., A **499** (2003)

[26] F. Bergsma et al. *The STAR Detector Magnet Subsystem* Nucl. Instr. and Meth. A **499** (2003)

[27] M. Anderson et al. *The STAR Time Projection Chamber: A Unique Tool for Studying High Multiplicity Events at RHIC* Nucl. Instr. and Meth. A **499** (2003)

[28] T. Roser *RHIC Status and Plans* RHIC Retreat (2002)

[29] L. Arnold et al. *The STAR silicon strip detector (SSD)* Nucl. Instr. and Meth. A**499** (2003)

[30] R. Bellwied et al. *The STAR silicon vertex tracker: A large area silicon drift detector* Nucl. Instr. and Meth. A**499** (2003)

[31] Y. V. Fisyak et al. *Overview of the Inner Silicon Detector Alignment Procedure and Techniques in the RHIC/STAR Experiment* J. Phys.: Conf. Ser. **119**, 032017; S. Margetis et al.,*Alignment Experience in STAR*, CERN Yellow Report (2007)

[32] S. Margetis, Personal Communication

[33] C. Chasman et al. *HFT Detector for STAR - Relativistic Nuclear Collisions Program*

[34] H. Sorge *Elliptical Flow: A Signature for Early Pressure in Ultrarelativistic Nucleus-Nucleus Collisions* Phys. Rev. Lett. **78**, 2309 (1997)

[35] Shusu Shi *The elliptic flow of multi-strange hadrons in* $\sqrt{S_{NN}} = 200\,GeV$ *Au+Au collisions at STAR* Nucl. Phys. A $\mathbf{862} - \mathbf{863}$, 263c (2011)

[36] P.F Kolb, J. Sollfrank and U. Heinz Anisotropic flow from AGS to LHC energies Phys. Rev. C **459**, 667 (1999)

[37] W. Reisdorf and H.G. Ritter *Collective flow in Heavy-Ion Collisions* Annu. Rev. Nucl. Part. Sci. **47**, 663 (1997)

[38] K. Gottfried and V.F. Weisskopf. *Concepts of Particle Physics*, volume 2. Oxford University Press, (1986).

[39] K. Geiger and B. Müller. Dynamics of parton cascades in highly relativistic nuclear collisions. *Nucl. Phys. B*, 369:600–654, (1992).

[40] K. J. Eskola. Formation and evolution of quark-gluon plasma at rhic and lhc. *Nucl. Phys. A*, 590:383c–398c, (1995).

[41] J.W. Harris. Physics of the star experiment at rhic. 14th Winter Workshop on Nuclear Dynamics, (1998).

[42] J. Rafelski and B. Müller. Hadrons and the quark-gluon plasma. *Phys. Rev. Lett.*, 48:1066, (1982).

[43] F. Wang. Strangeness in dense nuclear matter: A review of ags results. *J.Phys. G*, 27:283–300, (2001).

[44] P. Braun-Munzinger et al. Maximum relative strangeness content in heavy ion collisions around 30 agev. *Nucl.Phys. A*, 697:902–912, (2002).

[45] M. Thoma, M. Gyulassy, M. Plumer, and X.N. Wang. High p_t probes of nuclear collisions. *Nucl. Phys. A*, 538:37, (1992).

[46] J.W. Cronin et al. Production of hadrons at large transverse momentum at 200, 300, and 400 gev. *Phys. Rev. D*, 11:3105, (1975).

[47] Thomas Roser. Rhic status and plans. RHIC Retreat, (2002).

[48] H.M. Calvani and L.A. Ahrens. Au 32+ beam intensity losses in the ags booster due to charge exchange processes. *Booster Technical Note*, (228), (1996).

[49] D. Kharzeev and M. Nardi. Hadron production in nuclear collisions at rhic and high density qcd. *Phys. Lett. B*, 507:121–128, (2001).

[50] W.H. Christie. Luminosity limits for the star detector system. *STAR Note*, (125), (1994).

[51] F. Bergsma et al. The star detector magnet subsystem. *Nucl. Instr. and Meth. A*, 499, (2003).

[52] F.S. Bieser et al. The star trigger. *Nucl. Instr. and Meth. A*, 499, (2003).

[53] J.M. Landgraf et al., *An Overview of the STAR DAQ System* Nucl. Instrum. Meth. A 499, 762 (2003)

[54] C. Adler et al. *The STAR Level-3 Trigger System* Nucl. Instrum. Meth. A**499**, 778 (2003)

[55] C. Adler et al. The star level-3 trigger system. *Nucl. Instr. and Meth. A*, 499, (2003).

[56] M. Andersen et al. The star time projection chamber: A unique tool for studying high multiplicity events at rhic. *Nucl. Instr. and Meth. A*, 499, (2003).

[57] R. Bellwied et al. The star silicon vertex tracker: A large area silicon drift detector. *Nucl. Instr. and Meth. A*, 499, (2003).

[58] X. N. Wang. (1997).

[59] H.C. Eggers and J. Rafelski. Strangeness and quark gluon plasma: aspects of theory and experiment. *Int. J. Mod. Phys. A*, 6:1067–1114, (1991).

[60] T. Csörgo and B. Lørstad. Bose-einstein correlations for three-dimensionally expanding, cylindrically symmetric, finite systems. *Phys. Rev. C*, 54:1390–1403, (1996).

[61] T. Chujo. Results on identified hadrons from the phenix experiment at rhic. Quark Matter 2002, (2002).

[62] S.J. Brodsky and G.R. Farrar. Scaling laws at large transverse momentum. *Phys. Rev. Lett.*, 31:1153, (1973).

[63] M. Wing. Summary of session on jets and inclusive hadron production. Photon 2001, (2001).

[64] C. Adler et al. Midrapidity antiproton-to-proton ratio from au+au $\sqrt{s_{NN}} = 130$ gev. *Phys. Rev. Lett.*, 86:4778–4782, (2001).

[65] A. Drees. First hints of jet quenching at rhic. *Nucl. Phys. A*, 698:331–340, (2002).

[66] E. Wang and X.N. Wang. Interplay of soft and hard processes and hadron p_t spectra in pa and aa collisions. *Phys. Rev. C*, 64:034901, (2001).

[67] P. R. Bevington and D. K. Robinson. *Data Reduction and Error Analysis for the Physical Sciences.* McGraw-Hill, third edition, (2002).

[68] M. Lomnitz. Measurement of charmed meson azimuthal anisotropy in Au+Au collisions at $\sqrt{s_{NN}} = 200$ GeV at RHIC Ph.D. Dissertation, Kent State University (2016).

[69] G. Xie et al. Nuclear Modification Factor of D^0 Meson in Au+Au Collisions at $\sqrt{s_{NN}} = 200$ GeV at RHIC Talk at Quark Matter 2015, Japan. arXiv:1601.00695 [nucl-ex].

[70] L. Adamczyk et al. Observation of D0 Meson Nuclear Modifications in Au + Au Collisions $\sqrt{s_{NN}} = 200$ GeV. *Phys. Rev. Lett.*, 113:142301, (2014).

[71] S.S. Adler et al. Nuclear Modification of Electron Spectra and Implications for Heavy Quark Energy Loss in Au+Au Collisions at $\sqrt{S_{NN}} = 200\,\mathrm{GeV}$ Phys. Rev. Lett. **96**, 032301 (2006)

[72] B.I. Abelev et al. Energy dependence of $\pi^{\pm}$, p and $\bar{p}$ transverse momentum spectra for Au+Au collisions at $\sqrt{s_{NN}} = 62.4$ and 200 GeV. *Phys. Rev. B*, 655:104, (2007).

[73] K. A. Olive *et al.* [Particle Data Group Collaboration], Chin. Phys. C **38**, 090001 (2014). doi:10.1088/1674-1137/38/9/090001

[74] B. Abelev *et al.* [Star Collaboration], *Phys. Rev.* **C77**, 054901, (2008)

[75] W. Llope, et al. *The STAR Vertex Position Detector* arXiv:1403.6855 [physics.ins-det]

[76] R. Esha, M. Nasim, and H. Huang, (2016) arXiv:1603.02700 [nucl-th]

[77] H.-T. Ding, F. Karsch, and S. Mukherjee, *Int. J. Mod. Phys.* **E24**, 1530007 (2015)

[78] D. Banerjee, S. Datta, R. Gavai, and P. Majumdar, *Phys. Rev.* **D85**, 014510 (2012)